

THESIS ON NATURAL AND EXACT SCIENCES B174

**Nonlinear Sound Generation
Mechanisms in Musical Acoustics**

DMITRI KARTOFELEV

TUT
PRESS

TALLINN UNIVERSITY OF TECHNOLOGY
Institute of Cybernetics
Laboratory of Nonlinear Dynamics

This thesis was accepted for the defence of the degree of Doctor of Philosophy in Applied Mechanics on June 25, 2014.

Supervisor: Dr. Anatoli Stulov
Laboratory of Nonlinear Dynamics,
Institute of Cybernetics at Tallinn University of Technology

Opponents: Prof. Bogumił B.J. Linde
Institute of Experimental Physics, University of Gdańsk,
Gdańsk, Poland

Prof. German A. Maximov
Andreyev Acoustical Institute,
Moscow, Russia

Defence of the thesis: August 22, 2014.

Declaration:

Hereby I declare that this doctoral thesis, my original investigation and achievement, submitted for the doctoral degree at Tallinn University of Technology, has not been submitted elsewhere for any academic degree.

Dmitri Kartofelev



Copyright: Dmitri Kartofelev, 2014
ISSN 1406-4723
ISBN 978-9949-23-660-2 (publication)
ISBN 978-9949-23-661-9 (PDF)

LOODUS- JA TÄPPISTEADUSED B174

**Helitekke mittelineaarsed
mehhanismid muusikalises akustikas**

DMITRI KARTOFELEV

Contents

List of publications	7
Author's contribution	8
Introduction	9
String vibration against a rigid termination	9
Deformation wave propagation in piano hammer felt	10
Approbation	11
1 String vibration against a rigid termination	13
1.1 Vibration of a string with ideal supports	13
1.2 Termination–string interaction model	13
1.3 Grand piano string vibration	15
1.3.1 Hammer–string interaction	15
1.3.2 <i>Capo d'astro</i> –string interaction	17
1.4 Chikuzen biwa string vibration	20
1.4.1 String excitation	20
1.4.2 Influence of the <i>sawari</i>	21
1.5 Sitar string vibration	22
1.5.1 String excitation	22
1.5.2 <i>Jawari</i> geometry	23
1.5.3 Influence of the <i>jawari</i>	24
2 Deformation wave propagation in piano hammer felt	27
2.1 Wool felt model	27
2.2 Linear analysis	29
2.2.1 Dispersion relation	29
2.2.2 Phase and group velocities	31
2.2.3 Negative group velocity	33
2.3 Wave attenuation	34
2.3.1 Boundary value problem	34
2.3.2 Pulse attenuation rate	34
2.4 Nonlinear analysis	35
2.4.1 Initial value problem	35
2.4.2 Influence of the nonlinearity parameter p	36
2.4.3 Influence of the initial amplitude	36

3	Conclusions	38
3.1	Termination–string dynamic interaction	38
3.2	Deformation wave propagation in piano hammer felt	38
3.3	Final remarks	39
	References	40
	Acknowledgements	43
	Abstract	44
	Resümee	45
	Appendix A: Publications	47
	Publication I	49
	Publication II	59
	Publication III	69
	Publication IV	83
	Publication V	91
	Appendix B: CV	93
	Curriculum Vitae	95
	Elulookirjeldus	101
	Dissertations Defended at TUT	103

List of publications

The thesis is an overview of and is based on five academic publications, which are referred to in the text as Publication I, Publication II, Publication III, Publication IV and Publication V. All publications except Publication V have undergone a rigorous scientific peer review process.

- Publication I** A. Stulov and D. Kartofelev, “**Vibration of strings with nonlinear supports,**” *Applied Acoustics*, vol. 76, pp. 223–229, February 2014.
DOI: 10.1016/j.apacoust.2013.08.010
- Publication II** D. Kartofelev, A. Stulov, H.-M. Lehtonen, and V. Välimäki, “**Modeling a vibrating string terminated against a bridge with arbitrary geometry,**” in *Proceedings of SMAC 2013, 4th Stockholm Music Acoustics Conference* (R. Bresin and A. Askenfelt, eds.), (Stockholm, Sweden), pp. 626–632, KTH Royal Institute of Technology, 2013.
- Publication III** D. Kartofelev and A. Stulov, “**Propagation of deformation waves in wool felt,**” *Acta Mechanica*, Online first, pp. [1–11], 2014.
DOI: 10.1007/s00707-014-1109-1
- Publication IV** T. Peets, D. Kartofelev, K. Tamm, and J. Engelbrecht, “**Waves in microstructured solids and negative group velocity,**” *EPL - A Letters Journal Exploring the Frontiers of Physics*, vol. 103, no. 1, pp. 16001-p1–16001-p6, 2013.
DOI: 10.1209/0295-5075/103/16001
- Publication V**¹ D. Kartofelev and A. Stulov, “**Wave propagation and dispersion in microstructured wool felt.**”
The manuscript has been submitted to the journal *Wave Motion*

¹The manuscript was submitted on March 5, 2014. As of July 3, 2014 (printing date of the thesis) the manuscript was undergoing a peer review.

Author's contribution

A brief summary of the thesis author's contribution to the publications:

Publication I The analytical and numerical calculations as well as Figs. 2–9 were produced by the thesis author. In addition, the thesis author participated in conceiving, drafting, and producing the manuscript.

Publication II The entire work was conceptualized, produced, and presented at the conference by the thesis author. Some parts of the text were written or modified by the co-authors.

Publication III The numerical code and the finite difference approximation of the wool felt model equation were derived and written by the thesis author. All figures were produced by the thesis author. In addition, the thesis author participated in conceiving, drafting, and producing the manuscript.

Publication IV The subsection “Felt-type model” and part of the section “Discussion” were written by the thesis author. Figure 5 was produced and the corresponding calculations were performed by the thesis author.

Publication V The numerical code and the finite difference approximation of the wool felt model equation were written and derived by the thesis author. The author participated in conceiving, drafting, and producing the manuscript. All figures and the bulk of the final text were produced by the thesis author.

Introduction

The mechanism of the sound production of most musical instruments is inherently nonlinear. The thesis focuses on two novel nonlinear models closely connected to the sound production of some Eastern lutes and grand pianos. The thesis consists of three parts.

The first part of the thesis discusses the termination–string interaction model. The model simulates the collision of a vibrating string with the rigid spatial termination located at one of the string’s termination points. Three different examples of the model application are presented and discussed. The first part of the thesis is based on the results presented in Publications I and II.

The second part of the thesis, which is a summary of results presented in Publications III, IV (Section “Felt-type model”), and V, explores the mechanical behaviour and properties of wool felt. The one-dimensional strain wave propagation through the felt material is considered. In the grand piano the collision of a felt-covered hammer with a string is a crucial phenomenon that determines the piano tone and timbre. The proposed felt model provides a better understanding of the complex hammer–string interaction [1].

In the last part of the thesis the main conclusions and discussion are presented. Below introductions to the first and the second part of the thesis follow.

String vibration against a rigid termination

The investigation of the boundary conditions of a vibrating string is a very important problem in musical acoustics. It is well known that the fundamental frequency of the string is strictly determined by the type of the string termination. Usually, the changing of the tone caused by the shape and curvature of the string support is negligible because the size of the termination is much less than the string’s speaking length. But there exists a group of lutes, which are mainly used in China, Japan, and India, where the collision of a vibrating string with a rigid spatial obstacle is crucial to the desired tonal quality. The spatial extent of these bridges along the direction of the string may be up to 2% of the string’s speaking length.

Lutes such as the shamisen, biwa, sitar, tambura, or veena have a very distinctive sound, which can be described as *buzzing*. This overtone-rich tonal quality is strictly determined by the string termination [2, 3]. Examples of the string terminations discussed here are shown in Figs. 1.7 and 1.9. A similar structural mechanism is not unknown in Western instruments either. The treble strings of a grand piano usually terminate at the *capo*

d'astro [4]. The V-shaped cross-section of the *capo d'astro* has a parabolic curvature, although the area to which the string rapidly touches while vibrating is small in relation to the string's speaking length. In Publication I it is shown that the *capo d'astro* has a noticeable effect on the piano tone formation.

Much effort has been devoted to modelling the dynamics of a vibrating string with a distributed unilateral constraint during the past decades. Over the years many authors have solved this problem using different approaches. The problem was considered by Schatzman [5], Burrige *et al.* [6], and Cabannes [7], who used the method of characteristics and assumed that the string does not lose energy when it hits an obstacle. Krishnaswamy and Smith [8], Han and Grosenbaugh [9], Bilbao *et al.* [10, 11], and Taguti [12, 13] used a finite difference method to study the string interaction with the curved bridge. Vyasarayani, *et al.* [14] described the movement of the sitar string with a set of partial differential equations. Rank and Kubin [15], Evangelista and Eckerholm [16], and Siddiq [17] used a waveguide modelling approach to study the plucked string vibration with nonlinear limitation effects. The geometry of the string terminations for the sitar, veena, and tambura was considered by Raman [18]. Hall concluded that a possible explanation of the phenomena of the *missing modes* [19] is the complex interaction of the string with the bridge.

A novel and relatively simple model of termination–string interaction is presented in the first part of the thesis. A number of simplifying assumptions are introduced. The string is assumed to be non-dispersive lossless *ideal* string, and the termination is always assumed to be absolutely rigid. Despite these assumptions it is hoped that the application of the proposed model would clarify the physics behind the termination–string complex non-linear interaction.

Deformation wave propagation in piano hammer felt

More in-depth understanding of the complex process of the piano hammer–string interaction [1] requires a better knowledge of the mechanical properties of the felt that coats the heads of piano hammers. The aim of the second part of the thesis is to explore the mechanical and acoustical features of one of the oldest microstructured material known to man. The felt is a textile fabric. It is produced of randomized fibres that are tightly matted together. It can be made of natural fibres such as wool or synthetic fibres such as acrylic. Felt is used widely from the automotive industry to the construction of musical instruments. Some applications of felt include vibration isolation, air filtering, and interior décor. In piano manufacturing felt has been used for almost two centuries. For instance, the piano string dampers are made using felt and, of course, the felt made of wool is a unique

and indispensable coating material of piano hammers.

A description of the novel model of wool felt that is derived in Publications III and V is presented. The advanced model involves a one-dimensional nonlinear constitutive equation of microstructured felt based on the experimental results of testing piano hammers [1, 20]. The evolution of the form of a one-dimensional pulse propagating through a nonlinear felt medium is investigated in the context with the initial and boundary value problems. The rate of the attenuation of a propagating pulse is estimated and discussed. Dispersion analysis of the corresponding linear problem is provided, and it is shown that for certain values of physical parameters the negative group velocity will appear.

Approbation

The results presented in the thesis have been presented at the following scientific conferences:

1. J. Engelbrecht, T. Peets, and D. Kartofelev,
“Negative group velocity may appear in microstructured solids,” at *FUDoM 13 Finno-Ugric International Conference on Mechanics*,
Ráckeve, Hungary, August 11–15, 2013.
2. D. Kartofelev, A. Stulov, H.-M. Lehtonen, and V. Välimäki,
“Modeling a vibrating string terminated against a bridge with arbitrary geometry,” at *SMAC Stockholm Music Acoustics Conference 2013/SMC Sound and Music Computing Conference 2013*,
Stockholm, Sweden, July 30–August 3, 2013.
3. D. Kartofelev and A. Stulov²,
“Acoustical properties of the wool felt,” at *Symposium on the Acoustics of Poro-Elastic Materials (SAPeM 2011)*,
Ferrara, Italy, December 14–16, 2011.
4. D. Kartofelev and A. Stulov,
“Influence of the edge of the cast iron frame curvature on the spectrum of the piano string vibration,” at *2nd Vienna Talk on Music Acoustics*,
Vienna, Austria, September 19–21, 2010.
5. D. Kartofelev and A. Stulov²,
“Propagation of deformation wave in the piano hammer felt material,” at *International Conference on Complexity of Nonlinear Waves*, Tallinn, Estonia, October 5–7, 2009.

²The paper was orally presented by the second author A. Stulov.

6. D. Kartofelev and A. Stulov,
“Piano hammer–string interaction: the influence of the elastic parameters of bass hammer on contact time duration,” at *ACOUSTICS High Tatras 2009, 34th International Acoustical Conference - EAA Symposium*,
Nový Smokovec, High Tatras, Slovakia, September 28–30, 2009.
7. D. Kartofelev and A. Stulov,
“Vibration of the string with nonlinear contact condition,” at *18th International Symposium on Nonlinear Acoustics*,
Stockholm, Sweden, July 7–10, 2008.
8. D. Kartofelev and A. Stulov,
“String vibrations induced by piano hammers,” at *XIII Estonian Days of Mechanics*,
Tallinn, Estonia, September 15–16, 2008.

1 String vibration against a rigid termination

This part of the thesis, which is a summary of the results presented in Publications I and II, focuses on the model that describes the complex string motion, whose displacement is unilaterally constrained by a rigid string termination. In addition, three different examples of the model application are discussed.

1.1 Vibration of a string with ideal supports

In order to explore only the effect of the influence of a rigid termination on the string motion, we eliminate the possible contribution that the lossy and dispersive wave propagation may introduce to this nonlinear problem. This is the reason why the *ideal* flexible string description is considered. The wave equation for the linear and lossless flexible *ideal* string is in the form

$$\frac{\partial^2 u}{\partial t^2} = c^2 \frac{\partial^2 u}{\partial x^2}, \quad (1.1)$$

where u is the string displacement, $c = \sqrt{T/\mu}$ is the speed of the travelling waves on the string, T is the tension, and μ is the linear mass density of the string [21]. It can be shown that (1.1) may be satisfied by superposition of non-dispersive travelling waves $u_r(t - x/c)$ and $u_l(t + x/c)$ moving in either direction along the string emerging from the plucking or excitation point $x = l$

$$u(x, t) = u_r\left(t - \frac{x}{c}\right) + u_l\left(t + \frac{x}{c}\right). \quad (1.2)$$

These two waves u_r and u_l are simply a translation of the waves induced by the excitation from the point $x = l$ to other segments of the string [21]. At the point $x = l$ it holds that $u_r(l, t) = u_l(l, t) = u(l, t)$.

The ideal supports of the string terminations are described by the boundary values $u(0, t) = u(L, t) = 0$, here L is the speaking length of the string. The travelling waves $u_r(t - x/c)$ and $u_l(t + x/c)$ reflect from each end of the string. The wave $u_r(t - x/c)$ propagating to the right at the point $x = L$ creates the wave $u_l(t + x/c) = -u_r(t - x/c)$ moving to the left, and the wave $u_l(t + x/c)$ propagating to the left at the point $x = 0$ creates the wave $u_r(t - x/c) = -u_l(t + x/c)$ moving to the right. This procedure can be interpreted as equivalent to the digital waveguide approach [22, 23, 24]. The method for modelling the nonlinear termination-string interaction is explained below.

1.2 Termination-string interaction model

Nonlinear string terminations of stringed musical instruments are usually located at the far end of the neck (nut) or at the bridge. Similarly, in

our model, the geometric unilateral termination condition (TC) is located at one of the two termination points of the string. Figure 1.1 shows the travelling waves u_r and u_l , string displacement $u(x, t)$, and the location of the rigid termination relative to the string. Here it is assumed that the x -axis is defined by the shape and extent of the string at rest.

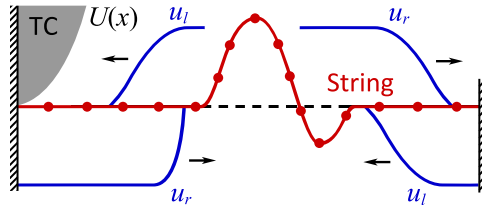


Figure 1.1: Scheme of the string displacement model. The travelling waves u_r and u_l , shown for two different time moments (unmarked solid lines), and the forms of the string (solid lines marked with circles). The position of the TC relative to the string is shown by the grey formation. The profile of the TC is described by the function $U(x)$.

In order to model the termination–string interaction it is assumed that the reflected wave $u_r(t - x/c)$ moving to the right appears only at the point $x = x^*$, where the amplitude of the string deflection $u(x^*, t) \geq U(x^*)$. The position of this point x^* is determined by the TC geometry function $U(x)$ in the following way. Since the termination is rigid, it must hold that $u(x^*, t) = U(x^*)$, and this condition results in the appearance (addition) of the reflected wave

$$u_r\left(t - \frac{x^*}{c}\right) = U(x^*) - u_l\left(t + \frac{x^*}{c}\right), \quad (1.3)$$

where the waves u_r and u_l correspond to any waves that have reflected on earlier time moments and are currently located at $x = x^*$. The proposed method ensures that the amplitude of the string deflection, which is determined by (1.2), will never exceed the value $U(x)$. The proposed procedure produces a reasonable result as long as the function $U(x)$ describing the string termination geometry is a monotonically growing or descending function.

Figure 1.2 demonstrates the form of the string in the vicinity of the geometric termination during the reflection of the first wave $u(t + x/c)$ only. By using the procedure described above, the string deflection as a function of the dimensionless distance along the string is computed for three succeeding normalized dimensionless ($c = 1$) moments of time. At the moment $t = t_1$ the form of the string, shown by the solid line marked with triangles, is determined only by the travelling wave u_l . At the next moment $t = t_2$ the small segment of the string is in contact with the surface of the

termination, and the reflected wave $u_r(x, t_2)$ has appeared (dashed line). The corresponding form of the string deflection is shown by the solid line marked with rectangles. At the moment $t = t_3$ the string is in contact with the surface of the termination on the segment closer to the string edge ($x = 0$). The form of the string at this moment is shown by the solid line marked with circles, and the reflected wave $u_r(x, t_3)$ is also shown by the dashed line. Thus, at some moments the string wraps or clings to the termination surface, and during that time the form of the string on some segment simply repeats the form of the termination.

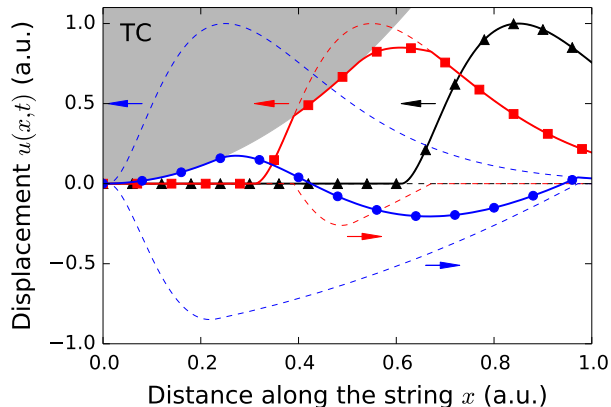


Figure 1.2: Reflection of the first wave from the termination. The travelling waves u_r and u_l (dashed lines) and the form of the string (marked solid lines) are shown for successive dimensionless moments of times $t_1 = 0.4$ (triangle), $t_2 = 0.7$ (rectangle), and $t_3 = 1.0$ (circle). Arrows indicate the direction of wave propagation.

1.3 Grand piano string vibration

1.3.1 Hammer–string interaction

The numerical simulation of the hammer–string interaction is based on the physical models of a piano hammer described in [1, 20, 25]. These models are based on the assumption that the woollen hammer felt is a microstructured material possessing history-dependent properties. The elastic and hereditary parameters of piano hammers were obtained experimentally by using a special piano hammer testing device that was developed and built at the Institute of Cybernetics at Tallinn University of Technology [20].

Like in [26, 27], we have the a system of equations describing the hammer–string interaction

$$\begin{cases} \frac{dz}{dt} = -\frac{2T}{cm} g(t) + V, \\ \frac{dg}{dt} = \frac{c}{2T} F(t), \end{cases} \quad (1.4)$$

where the function $g(t)$ is the form of the outgoing travelling wave created by the hammer strike at the contact point $x = l$, c is the speed of a non-dispersive wave travelling along the string, $F(t)$ is the acting force, T is the string tension, m , $z(t)$, and V are the hammer mass, the hammer displacement, and the hammer velocity, respectively. The hammer felt compression is defined by $w(t) = z(t) - u(l, t)$. Here the function $u(l, t)$ describes the string transverse deflection at the contact point $x = l$. String deflection $u(l, t)$ is calculated by using the knowledge on the outgoing wave $g(t)$ and the string's mathematical description discussed in Sections 1.1 and 1.2. The initial conditions at the moment when the hammer first contacts the string are taken as $g(0) = z(0) = 0$, and $dz(0)/dt = V$.

The experimental testing of piano hammers demonstrates that all hammers have a hysteretic type of force–compression characteristics. A main feature of hammers is that the slope of the force–compression characteristics is strongly dependent on the rate of loading. It was shown in [1, 20, 25] that nonlinear hysteretic models can successfully describe the dynamic behaviour of the hammer felt.

According to the three-parameter hereditary model of the hammer presented in [25], the nonlinear force $F(t)$ exerted by the hammer is related to the felt compression $w(t)$ by the following expression:

$$F(w(t)) = Q_0 \left[w^{\hat{p}} + \alpha \frac{d(w^{\hat{p}})}{dt} \right]. \quad (1.5)$$

Here the parameter Q_0 is the static hammer stiffness, \hat{p} is the compliance nonlinearity exponent, and α is the retarded time parameter.

The continuous variations in the hammer parameters across the entire compass of the piano were obtained experimentally by measuring an entire hammer set of recently produced and unvoiced *Abel* hammers. The result of those experiments is presented in [20, 25]. A best match to a whole set of hammers $1 \leq n \leq 88$ is approximated by using

$$Q_0 = 183 e^{0.045n}, \quad (1.6)$$

$$\hat{p} = 3.7 + 0.015n, \quad (1.7)$$

$$\alpha = 259.5 + 0.58n + 6.6 \cdot 10^{-2}n^2 - 1.25 \cdot 10^{-3}n^3 + 1.172 \cdot 10^{-5}n^4. \quad (1.8)$$

Here the unit for parameter α is ms, and the unit for Q_0 is N/mm $^{\hat{p}}$. The hammer masses of this set are approximated by

$$m = 11.074 - 0.074n + 10^{-4}n^2, \quad 1 \leq n \leq 88. \quad (1.9)$$

The mass of hammer no. 1 (A_0) is 11.0 g and the mass of the last hammer no. 88 (C_8) is 5.3 g.

1.3.2 *Capo d'astro*–string interaction

The treble strings of grand pianos usually terminate at the *capo d'astro* (capo bar) [4]. The *capo d'astro* is a part of the piano cast iron frame's substructure called the *agraffe*. The shape of the *capo d'astro* is carved out of the cast iron and reinforced (coated) with an titanium. The apex of the V-shaped cross-section profile of the *capo d'astro* defines the end of the speaking length of the string. This rigid termination has an approximately parabolic form, and it is described here by the function $U(x) = (2R)^{-1}x^2$, where R is the radius of the *capo d'astro* curvature at $x = 0$ (at the apex). Figure 1.3 presents the scheme of the *capo d'astro*–string interaction model.

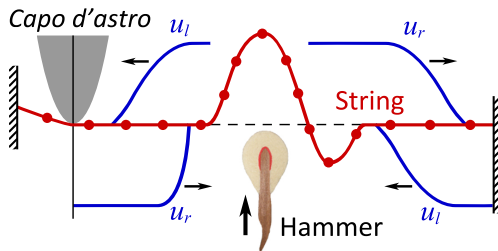


Figure 1.3: Scheme of the *capo d'astro*–string interaction model. The string is excited by the piano hammer strike. The direction of the hammer strike is shown by the bold arrow. The parabolic shape of the *capo d'astro* is shown by the grey formation. The shape of the string is shown by the solid line marked with circles. The small arrows indicate the propagation direction of the travelling waves u_r and u_l shown for two different time moments.

In this simulation a number of simplifying assumptions regarding the piano string are introduced. As mentioned above, the string is assumed to be an *ideal* flexible string. In addition, the motion of the soundboard and the bridge are discarded.

The hammer–string interaction is simulated by solving a system of Eqs. (1.4) for various initial hammer velocities V . The note no. 85 (tone A_7 , fundamental frequency $f = 3520$ Hz) is chosen for the calculations. The string parameters are the following: the string's speaking length $L = 61$ mm, the actual distance of the striking point from the nearest string end (*capo d'astro*) $l = 2.6$ mm, the linear mass density of the string $\mu = 4.2$ g/m, the string mass $M = 0.26$ g, the string tension $T = 774.6$ N.

The number of strings associated with the grand piano tone A_7 is three. Thus, the acting mass of a hammer defined by relation (1.9) for $n = 85$ is chosen equal to 1/3 of the total hammer mass, resulting in $m = 1.8$ g. For hammer no. 85 we use the following additional parameters: static stiffness $Q_0 = 8387.4$ N/mm $^{\hat{p}}$, nonlinearity exponent $\hat{p} = 4.975$, hereditary parameter $\alpha = 0.5312$ ms.

It is concluded in Publication I that the resulting string's movement

is strongly influenced by the termination for approximately the first 15–20 interactions (periods). After this time elapses ($t \simeq 6$ ms, in the current case), the vibration of the string terminated at the *capo d'astro* may be considered as periodical. This phenomenon can be demonstrated through the string vibration spectra. Figure 1.4 shows the string motion spectra for the string that is excited by the piano hammer, where $V = 5$ m/s.

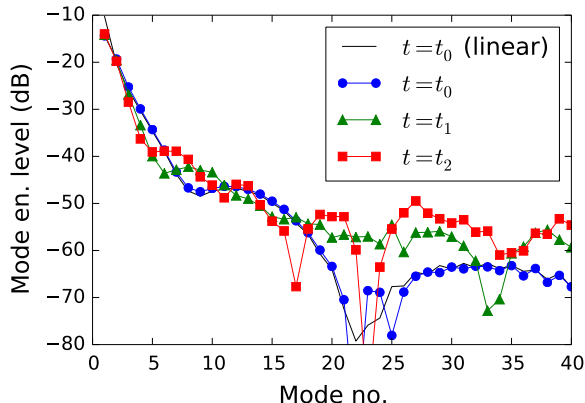


Figure 1.4: Comparison of spectra envelopes computed for successive time moments: $t_0 = 0.3$ ms, $t_1 = 3.86$ ms, $t_2 = 6.21$ ms. The solid line without marks shows the spectrum of the string with the ideal support. The marked solid lines show the spectra of the string that is terminated at the *capo d'astro*, where $R = 15$ mm. Hammer striking velocity $V = 5$ m/s.

At the moment $t = t_0$ (hammer–string contact duration) only a small difference between the spectra of the strings vibrations can be observed. After this time moment the spectrum of the string with the ideal support becomes stationary, in other words the spectrum is not time-dependent. On the contrary, the spectrum of the string terminated at the *capo d'astro* continues to change with the progression of time, even after the string starts to vibrate freely. The effect of the TC continues for approximately 6 ms, and after this time the spectrum becomes stationary as well. These two distinct vibration regimes, observed in the case where the strings are terminated at the *capo d'astro*, are called here the *aperiodic* and *periodic* vibration regimes, respectively. During the *aperiodic* vibration regime the level of the first five modes decreases systematically. The difference between the levels of the 4th mode for the ideally supported string and for the string terminated at the *capo d'astro* is equal to 6 dB. Undoubtedly, the transition of energy from low to high vibration modes is occurring. The power spectrum of the string vibration is widened by enriching the levels of high frequency vibration modes. The level of some high frequency vibration modes increases up to 15 dB.

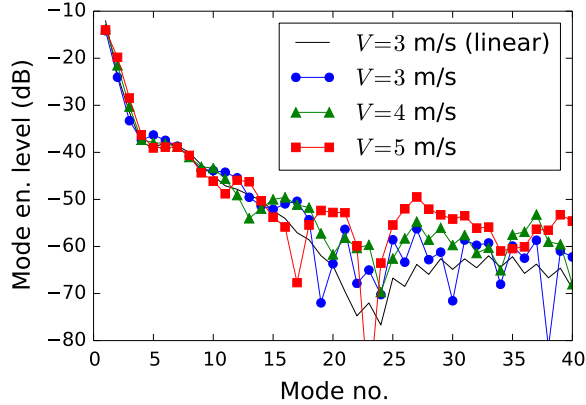


Figure 1.5: Comparison of spectra envelopes computed for the constant value of the *capo d'astro* curvature $R = 15$ mm and varying the hammer striking velocity V . The solid line without marks shows the spectrum of the string with the ideal support. The marked solid lines show the spectra of the string that is terminated at the *capo d'astro*.

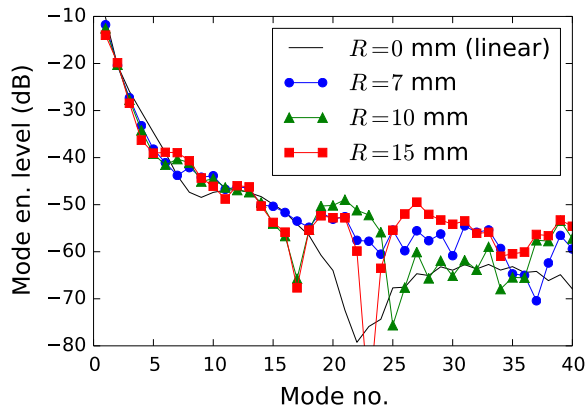


Figure 1.6: Comparison of spectra envelopes computed for the constant value of the hammer striking velocity $V = 5$ m/s and varying the radius of the *capo d'astro* curvature R . The solid line without marks shows the spectrum of the string with the ideal support. The marked solid lines show the spectra of the string terminated at the *capo d'astro*.

Figure 1.5 demonstrates the changing of the string vibration spectrum with the variation of the amplitude of the string excitation. The results are presented for the *capo d'astro* curvature $R = 15$ mm, and for the time moment $t = 6.21$ ms (beginning of the *periodic* vibration regime). It is evident that with the increasing of the amplitude of the string vibration the mean level of high frequency modes increases; this phenomenon confirms that the interaction between the termination and the string is nonlinear

indeed.

The effect of the *capo d'astro* profile curvature on the spectra of the piano string vibration is shown in Fig. 1.6. The result is presented for the hammer striking velocity $V = 5$ m/s, and for the time moment $t = 6.21$ ms (beginning of the *periodic* vibration regime). By analysing the result presented in Fig. 1.6 it is concluded that the increasing of the curvature radius increases the energy levels of the high frequency vibration modes, and therefore it is possible to quantify the energy transfer from the lower to the higher partials by using the proposed model.

1.4 Chikuzen biwa string vibration

The Chikuzen biwa is a traditional Japanese short-necked fretted lute, which is often used in narrative storytelling. The biwa is equipped with a *sawari* mechanism shown in Fig. 1.7. The *sawari* is usually made of bamboo and it is located at the nut, where it terminates the speaking length of the five silk strings of the biwa.

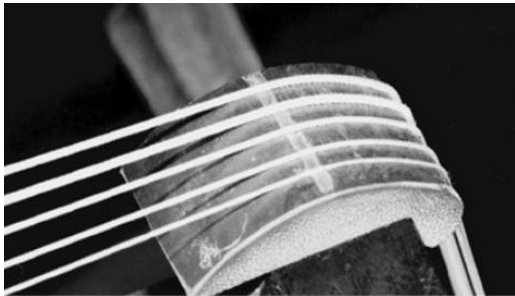


Figure 1.7: *Sawari* located at the nut of the *Chikuzen biwa* neck and five strings made of silk.

1.4.1 String excitation

The biwa string vibration is described here also by Eq. (1.1), i.e. we consider the biwa string as an *ideal*. The parameters for the biwa string are taken to be the same as used by Taguti in [13]. The values of the string parameters are the following: string's speaking length $L = 0.8$ m, linear mass density $\mu = 0.375$ g/m, string tension $T = 38.4$ N, and the speed of waves travelling along the string $c = 320$ m/s. The main tone frequency of such a string $f = 200$ Hz.

The string plucking condition is chosen as follows: at a moment $t = 0$ the force

$$F(t) = F_0 \alpha t e^{-\alpha t} \quad (1.10)$$

starts to act on the string at a point $x = 3/4L$ in a vertical direction and perpendicularly to the string at rest. At a moment $t = t_0$ the force stops acting on the string, i.e. $F(t) = 0$ if $t > t_0$. Here the parameter $\alpha = 2 \text{ ms}^{-1}$, the duration of the force action $t_0 = 2.5 \text{ ms}$, and $F_0 = 0.96 \text{ N}$.

According to the system of equations (1.4), the outgoing wave $g(t)$ created by this force is determined by the continuous function

$$g(t) = \begin{cases} A \{1 - [1 + \alpha t] e^{-\alpha t}\}, & \text{if } t < t_0, \\ \text{const} = g(t_0), & \text{if } t \geq t_0. \end{cases} \quad (1.11)$$

Here the coefficient $A = 2 \text{ mm}$ and $g(t_0) = 1.92 \text{ mm}$.

1.4.2 Influence of the *sawari*

The cross-section profile of the *sawari* is approximated by the function

$$U(x) = \begin{cases} -\frac{1}{2R}x^2, & \text{if } x \leq s, \\ -\infty, & \text{if } x > s, \end{cases} \quad (1.12)$$

where s is the extent of the *sawari* along the string at rest (x -axis), R is the radius of the *sawari* curvature at the string termination point $x = 0$. The values of the parameters s and R for *sawari* in Chikuzen biwa are taken $s = 1 \text{ cm}$, and $R = 2 \text{ m}$. The surface of the *sawari* is considered to be absolutely rigid.

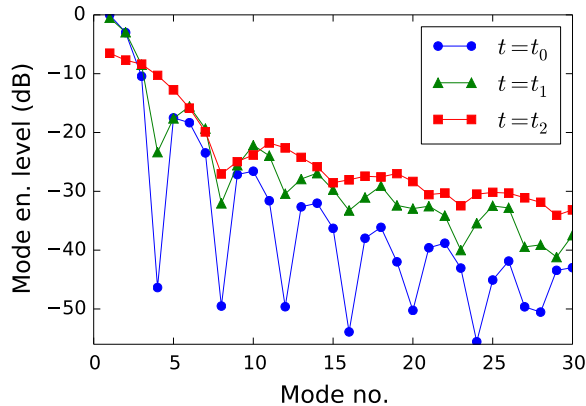


Figure 1.8: Evolution of the biwa string motion spectrum with the progression of time, where $t_0 = 2.5 \text{ ms}$, $t_1 = 16.4 \text{ ms}$, and $t_2 = 201.4 \text{ ms}$.

The effect of the *sawari* on the spectral structure of the biwa string vibration is shown in Fig. 1.8. Analysis of the spectral structure of the biwa string vibration reveals that it undergoes a period of rapid change (*aperiodic* vibration regime), which in this particular case lasts for approximately

200 ms. It can be shown that after that time period has elapsed the spectrum becomes stable (*periodic* vibration regime). Figure 1.8 shows clearly that during that time the mean level of the high frequency modes increases significantly, and the level of some low frequency modes decreases. This suggests that the vibration energy is being transferred from lower to higher partials.

1.5 Sitar string vibration

The sitar is a plucked stringed instrument, which is used mainly in Hindustani music and Indian classical music. The instrument descended from a similar but simpler Persian instrument called the setar. The main strings of the sitar terminate at the bridge called the *jawari*. The *jawari* shown in Fig. 1.9 has an almost flat cross-section shape, and it is classically made of animal bone or horn.

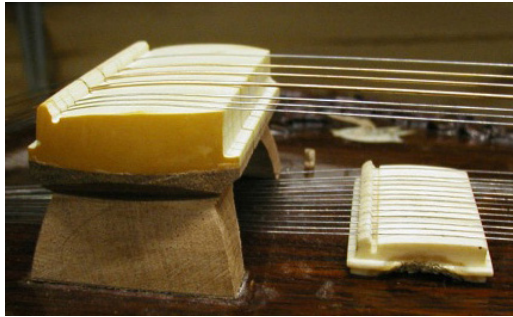


Figure 1.9: *Jawari*, the main bridge of the sitar, and *taraf ka ghoraj*, the sympathetic string bridge.

1.5.1 String excitation

The string plucking condition is introduced as follows. It is assumed that from the point $x = l = 3/4L$ outgoing waves emerge, and they have the following form:

$$g(t) = \begin{cases} A \left(\frac{t}{t_0}\right)^2 e^{2(1-t/t_0)}, & \text{if } 0 \leq t \leq t_0, \\ A, & \text{if } t > t_0. \end{cases} \quad (1.13)$$

Here $A = 1$ cm is the amplitude of the outgoing travelling wave and the duration of the excitation is $t = t_0 = 4$ ms. The selection of the plucking condition (1.13) ensures that the plucking force acting on the string at $x = l$ ceases if $t \geq t_0$ because the time derivative of (1.13) is proportional to the plucking force; *cf.* Eq. (1.4). The values of the string parameters are taken to be the same as in the previous example of the biwa string vibration.

1.5.2 *Jawari* geometry

As in Publication II, three mostly flat *jawari*-like cross-section profiles of the string termination are considered. Figure 1.10 shows these profiles. The mathematical descriptions of the profile shape functions $U(x)$ are provided below.

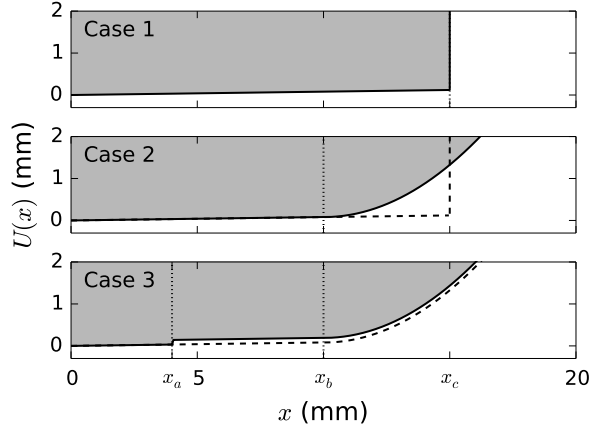


Figure 1.10: *Jawari*-like TC profile geometry for three cases under study. Dotted vertical lines mark the positions of the characteristic values x_a , x_b , and x_c . Case 1: Linear bridge with a sharp edge. Case 2: Linear bridge with a curved edge; the dashed line shows the profile of Case 1 for comparison. Case 3: Bridge with a small geometric imperfection; the dashed line shows Case 2 for comparison.

Case 1: Linear bridge with a sharp edge

The function $U(x)$ that describes the profile of a flat sitar's *jawari*-like bridge is calculated as follows:

$$U(x) = \begin{cases} kx, & \text{if } x \leq x_c, \\ \infty, & \text{if } x > x_c, \end{cases} \quad (1.14)$$

where $k = \tan \theta = 0.008$ is the slope of the linear function, and where $\theta \approx 0.008 \text{ rad} \approx 0.46^\circ$. The value $x_c = 15 \text{ mm}$ marks the coordinate of the truncation of the linear function with respect to the x -axis.

Case 2: Linear bridge with a curved edge

The profile of a *jawari* bridge with a curved edge is calculated as follows:

$$U(x) = \begin{cases} kx, & \text{if } x \leq x_b, \\ \frac{1}{2R}(x - x_b)^2, & \text{if } x > x_b, \end{cases} \quad (1.15)$$

where the parameter k has the same value and meaning as in the previous case. The parameter $R = 10$ mm is the curvature radius of the corresponding parabolic function $f(x) = (2R)^{-1}x^2$ at its local minimum. The coordinate $x_b = 10$ mm marks the transition between linear and parabolic parts of the geometry.

Case 3: Bridge with a geometric imperfection

The bridge in this case is similar to the previous case with the exception of an addition of a small imperfection in the form of discontinuity in the linear part of the TC in (1.15). The bridge profile geometry for this case can be expressed in the following form:

$$U(x) = \begin{cases} kx, & \text{if } x \leq x_a, \\ kx + y, & \text{if } x_a < x \leq x_b, \\ \frac{1}{2R}(x - x_b)^2 + K, & \text{if } x > x_b, \end{cases} \quad (1.16)$$

where the parameters k and R have the same values and meaning as in the previous cases. The parameter $y = 0.11$ mm raises the value of the linear function in the interval $x = (x_a, x_b]$, where $x_a = 4$ mm and $x_b = 10$ mm. The constant $K = kx_b + y$ is added in order to preserve the continuity of the form in the vicinity of the point $x = x_b$.

1.5.3 Influence of the *jawari*

The influence of the *jawari* on the string vibration is demonstrated through the use of spectrograms. The spectrograms are calculated by using the Hanning window of the size 45 ms and the overlap value of 55% of the window size.

Case 1: Linear bridge with a sharp edge

The spectrogram of the string vibration related to Case 1 is shown in Fig. 1.11 a. The dashed vertical line corresponds to the duration of the *aperiodic* vibration regime $t = t_{np}$ of the string. It can be seen that during the *aperiodic* vibration regime the energy of the low frequency vibration modes is being transferred to the high frequency modes. This phenomenon of the spectral widening can be noticed by comparing Figs. 1.11 a and 1.12.

Figure 1.12 shows the spectrogram of the corresponding linear case of the string with ideal supports where no amplitude limiting TC is present. The transfer of the energy from lower to higher vibration modes is an indication of the nonlinear behaviour resulting from the interaction of the vibrating string and the *jawari* bridge. In the *periodic* vibration regime ($t > t_{np}$) the spectrum remains constant.

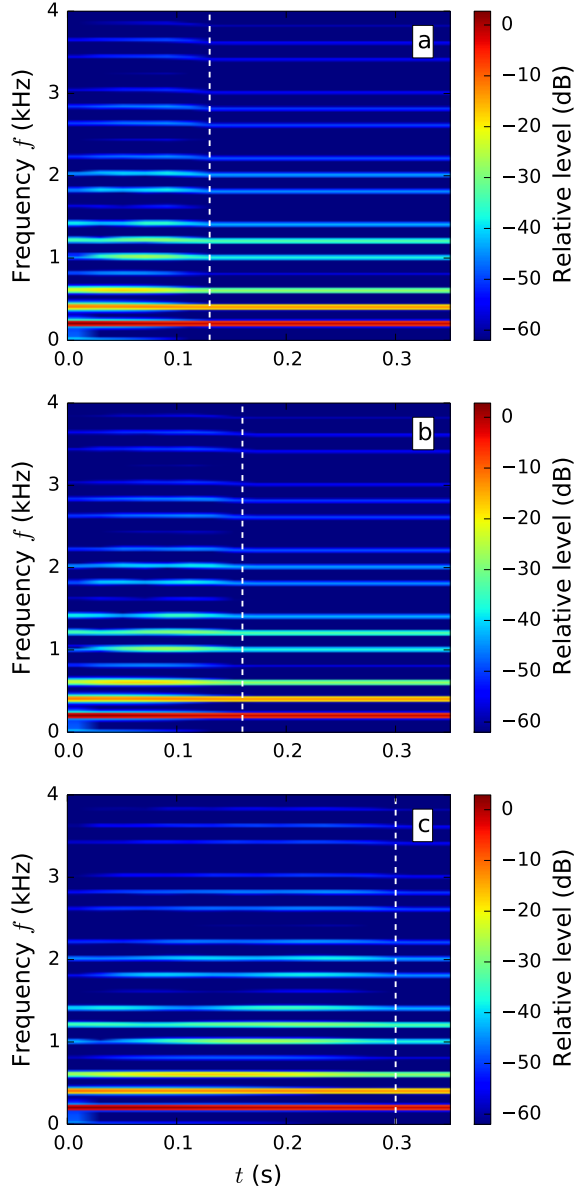


Figure 1.11: Spectrogram of the string vibration waveform $u(l, t)$ for (a) Case 1, (b) Case 2, and (c) Case 3. The transition between the *aperiodic* and *periodic* vibration regimes at $t = t_{np}$ is shown by the dashed line.

Case 2: Linear bridge with a curved edge

The spectrogram corresponding to Case 2 is shown in Fig. 1.11 b. As can be seen, the result is similar to Case 1 with the exception of a slightly longer *aperiodic* vibration regime.

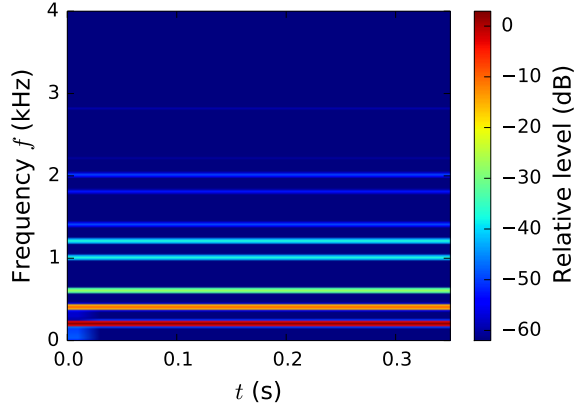


Figure 1.12: Spectrogram of the string vibration waveform $u(l, t)$ for the linear case.

Case 3: Bridge with a geometric imperfection

Figure 1.11 c shows the spectrogram for Case 3. Now the *aperiodic* vibration regime lengthens lasting for 300 ms, which is almost two times longer compared to Case 2. Again, the energy transfer from low frequency to high frequency modes is visible during the *aperiodic* vibration regime.

The relatively long *aperiodic* vibration regime can make playing such an instrument challenging. The timbre of the instrument can be strongly influenced by the selection of the plucking point and the plucking manner, which results in an uneven timbre behaviour. This phenomenon makes the learning to play the sitar more demanding compared to the similar Western stringed instruments such as acoustic guitar, for example.

2 Deformation wave propagation in piano hammer felt

This part of the thesis, which is a summary of the results presented in Publications III, IV (Section “Felt-type model”), and V, focuses on the mechanical and acoustical properties of the wool felt material that is used in manufacturing piano hammers.

2.1 Wool felt model

The first nonlinear dynamical model of piano hammer felt, that takes into consideration both the hysteresis of the force-compression characteristics and their dependence on the rate of the felt loading was presented in [1]. The derived model is based on the assumption that hammer felt is a microstructured material possessing history-dependent properties, i.e. it is a material with memory.

The constitutive equation of nonlinear microstructured wool felt may be assumed in the form

$$\sigma(\epsilon) = E\epsilon^p(t). \quad (2.1)$$

Here σ is the stress, $\epsilon = \partial u / \partial x$ is the strain, u is the displacement, E is Young’s modulus, and p is the nonlinearity parameter.

Following Rabotnov [28], the constitutive equation of the microstructured wool felt is derived by replacing the constant value of Young’s modulus E in expression (2.1) by a time-dependent operator $E_d [1 - \mathcal{R}(t)*]$, where $*$ denotes the convolution operation, and the relaxation function is given by

$$\mathcal{R}(t) = \frac{\gamma}{\tau_0} e^{-t/\tau_0}, \quad 0 \leq \gamma < 1. \quad (2.2)$$

Here the hereditary amplitude γ and the relaxation time τ_0 are the hereditary parameters of the wool felt. The time history of felt deformation is assumed to start at $t = 0$. This means that for the case of one-dimensional deformation and for any rate of loading the hysteretic felt material is defined by the constitutive equation

$$\sigma(\epsilon) = E_d [\epsilon^p(t) - \mathcal{R}(t) * \epsilon^p(t)], \quad (2.3)$$

where the constant E_d is the dynamic Young’s modulus. From Eq. (2.3) it follows that if $t \ll \tau_0$, then one obtains the constitutive equation for the fast felt compression

$$\sigma(\epsilon) = E_d \epsilon^p(t), \quad (2.4)$$

and if $t \gg \tau_0$, then one has the constitutive equation for the slow compression

$$\sigma(\epsilon) = E_d(1 - \gamma)\epsilon^p(t) = E_s \epsilon^p(t). \quad (2.5)$$

In each of these two cases, the loading and unloading of the felt follows the same path along the stress–strain curve. The quantity $E_s = E_d(1 - \gamma)$ is the static Young’s modulus of the felt material. Both Young’s moduli are physical parameters of the felt material, and their values are $0 < E_s < \infty$ and $0 < E_d < \infty$. For this reason, within the frame of the felt model, the value of the hereditary amplitude is always $\gamma < 1$.

The governing equation of motion, which describes the evolution of the one-dimensional wave in the felt material, is derived from the classical equation of motion

$$\rho \frac{\partial^2 u}{\partial t^2} = \frac{\partial \sigma}{\partial x}, \quad (2.6)$$

where ρ is the density of the medium. Substitution of (2.3) in Eq. (2.6) and elimination of the integral term leads to the equation in the following form, presented in terms of the displacement u :

$$\rho u_{tt} + \rho \tau_0 u_{ttt} - E_d \{ (1 - \gamma) [(u_x)^p]_x + \tau_0 [(u_x)^p]_{xt} \} = 0, \quad (2.7)$$

where the subscripted indices denote the differentiation with respect to the indicated variable.

One can derive the dimensionless form of Eq. (2.7) by using the dimensionless variables

$$u \Rightarrow \frac{u}{l_0}, \quad x \Rightarrow \frac{x}{l_0}, \quad t \Rightarrow \frac{t}{\alpha_0}, \quad (2.8)$$

where

$$\alpha_0 = \frac{\tau_0}{\delta}, \quad l_0 = c_d \alpha_0 \sqrt{\delta}, \quad \delta = 1 - \gamma, \quad c_d = \sqrt{\frac{E_d}{\rho}}, \quad c_s = c_d \sqrt{\delta}. \quad (2.9)$$

Thus, in terms of the dimensionless displacement variable $u(x, t)$ Eq. (2.7) takes the following form:

$$[(u_x)^p]_x - u_{tt} + [(u_x)^p]_{xt} - \delta u_{ttt} = 0, \quad (2.10)$$

and for the strain variable $\epsilon(x, t)$ Eq. (2.7) reads

$$(\epsilon^p)_{xx} - \epsilon_{tt} + (\epsilon^p)_{xxt} - \delta \epsilon_{ttt} = 0. \quad (2.11)$$

Several samples of felt pads were subjected to static stress–strain tests. The average value of the static Young’s modulus of the felt pads was estimated to be $E_s = 0.6$ MPa. The average value of the felt density was determined as $\rho \approx 10^3$ kg/m³. By using the realistic values of the hereditary parameters $\gamma = 0.96$ and $\tau_0 = 10$ μ s presented in [20], we obtain

$$\delta = 0.04, \quad E_d = 15 \text{ MPa}, \quad c_s = 25 \text{ m/s}, \quad c_d = 125 \text{ m/s}. \quad (2.12)$$

By using these values of material constants, the space scale l_0 and time scale α_0 that were used in (2.8) are

$$l_0 = 6.25 \text{ mm}, \quad \alpha_0 = 0.25 \text{ ms}. \quad (2.13)$$

2.2 Linear analysis

2.2.1 Dispersion relation

The peculiar characteristics of the solution of Eq. (2.11) are already revealed in the linear case, where $p = 1$

$$\epsilon_{xx} - \epsilon_{tt} + \epsilon_{xxt} - \delta\epsilon_{ttt} = 0. \quad (2.14)$$

The fundamental solution of this equation has the form of travelling waves

$$\epsilon(x, t) = \hat{\epsilon} e^{ikx - i\Omega t}, \quad (2.15)$$

where i is an imaginary unit, k is the wave number, Ω is the angular frequency, and $\hat{\epsilon}$ is the amplitude. The dispersion law $\Phi(k, \Omega) = 0$ of Eq. (2.14) is defined by the relation

$$k^2 - \Omega^2 - ik^2\Omega + i\delta\Omega^3 = 0. \quad (2.16)$$

In the case of an initial value problem, the general solution of Eq. (2.14) has the following form:

$$\epsilon(x, t) = \frac{1}{2\pi} \int_{-\infty}^{\infty} \chi(k) e^{ikx - i\Omega(k)t} dk, \quad (2.17)$$

where $\chi(k)$ is the Fourier transform of the initial disturbance of the strain prescribed at $t = 0$. The dependence $\Omega = \Omega(k)$ can be derived from the dispersion relation (2.16). In the general case $\Omega(k)$ is a complex quantity. In order to provide dispersion analysis in the context of an initial value problem and in the complex number domain, we rewrite the frequency $\Omega(k)$ in the form

$$\Omega(k) = \omega(k) + i\mu(k), \quad (2.18)$$

where $\omega = \text{Re}(\Omega)$ and $\mu = \text{Im}(\Omega)$. By using this notation, Eq. (2.15) can be rewritten as follows:

$$\epsilon(x, t) = \hat{\epsilon} e^{ikx - i\omega t + \mu t} = e^{\mu t} \hat{\epsilon} e^{ikx - i\omega t}. \quad (2.19)$$

From here it is evident that for the negative values of $\mu(k)$ it acts as an exponential decay function. In other words, the spectral components decay exponentially as $t \rightarrow \infty$ for $\mu(k) < 0$. On the other hand, if $\mu(k) > 0$, then the amplitude of the corresponding spectral component increases exponentially with the progression of time, and the solution of Eq. (2.14) becomes unstable.

By taking into account (2.18), the dispersion relation (2.16) takes the following form:

$$k^2 - ik^2\omega - \omega^2 + i\delta\omega^3 + k^2\mu - 2i\omega\mu - 3\delta\omega^2\mu + \mu^2 - 3i\delta\omega\mu^2 + \delta\mu^3 = 0. \quad (2.20)$$

The dispersion relation (2.20) can be separated into real and imaginary parts. A suitable solution of this simultaneous equation with respect to ω and μ has the following form:

$$\begin{cases} \omega(k) = \frac{\sqrt{6}}{12\delta S} \sqrt{\sqrt[3]{2}S^4 - 4S^2(1 - 3k^2\delta) + 2\sqrt[3]{4}(1 - 3k^2\delta)^2}, \\ \mu(k) = \frac{1}{12\delta S} \left[\sqrt[3]{4}S^2 - 4S + 2\sqrt[3]{2}(1 - 3k^2\delta) \right], \end{cases} \quad (2.21)$$

where

$$S = \sqrt[3]{2 - 9k^2\delta(1 - 3\delta) + 3k\delta\sqrt{3Q}} \quad (2.22)$$

and

$$Q = 4k^4\delta - k^2(1 + 18\delta - 27\delta^2) + 4. \quad (2.23)$$

This solution is physically reasonable, because it satisfies the conditions $\omega \in \mathbb{R}$, $\mu \in \mathbb{R}$, and $\mu \leq 0$. It can be shown that the solution (2.21) has three distinct modes of behaviour depending on the value of the parameter δ . These three regimes correspond to the following values of δ : (i) $0 < \delta \leq 1/9$; (ii) $1/9 < \delta < 1$; (iii) $\delta = 1$. A detailed analysis of these three cases is presented in Publication V. The following text in the thesis will address only case (ii).

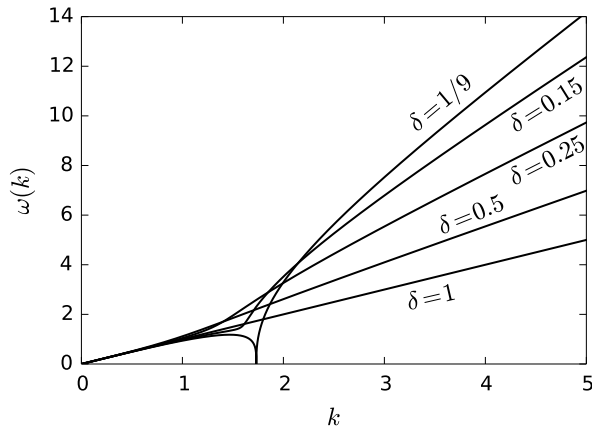


Figure 2.1: Dispersion curves $\omega(k)$ calculated for different values of the material parameter δ .

Figures 2.1 and 2.2 show examples of the dispersion curves for the case (ii), where $1/9 < \delta < 1$. The dispersion curves are continuous functions, and one can notice that as the parameter δ becomes larger the dispersion curve $\omega(k)$ becomes progressively more similar to the dispersion curve of the non-dispersive medium, where $\omega(k) = k$, $\mu(k) = 0$. Also, the average value of the exponential decay function $\mu(k)$ becomes progressively smaller with

the increasing of the value of δ , especially for the larger k values. Figure 2.2 shows that the decay function $\mu(k)$ is more or less constant if $k > 2$. The limits of dispersion relations $\omega(k)$ and $\mu(k)$ for large k are

$$\lim_{k \rightarrow \infty} \omega(k) = \infty, \quad (2.24)$$

$$\lim_{k \rightarrow \infty} \mu(k) = -\frac{1 - \delta}{2\delta}. \quad (2.25)$$

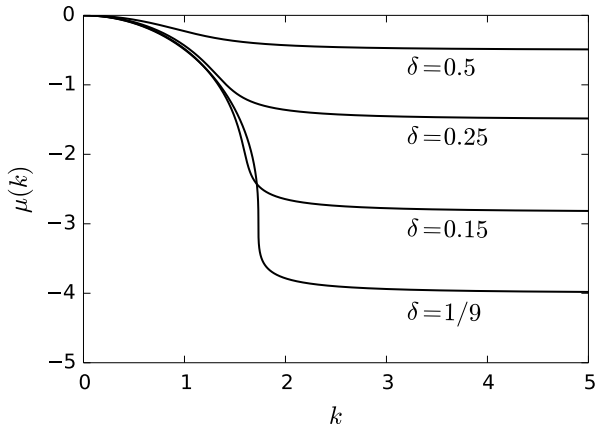


Figure 2.2: Dispersion curves $\mu(k)$ (exponential decay function) calculated for different values of the material parameter δ .

2.2.2 Phase and group velocities

The phase velocity, which is defined as $v_{ph}(k) = \omega/k$, can be obtained from (2.21). The group velocity can be calculated by taking the derivative $v_{gr}(k) = d\omega/dk$. The limits of these velocities for large values of k are

$$\lim_{k \rightarrow \infty} v_{ph}(k) = \lim_{k \rightarrow \infty} v_{gr}(k) = \frac{1}{\sqrt{\delta}} = v_{\alpha}. \quad (2.26)$$

Taking into account (2.8) and (2.9), one can find the relation between the dimensionless and dimensional values of these velocities. The dimensionless value of $v_{ph} = 1$ corresponds to the dimensional value $V_{ph} = c_s$, and $v_{gr} = v_{\alpha}$ corresponds to $V_{gr} = c_d$.

In Figs. 2.3, 2.4, and 2.5 the phase and group velocities are plotted against the wave number k . In Figs. 2.3 and 2.5 the regions of normal and anomalous dispersion can be distinguished. The dispersion plot is divided between these two regions at the point $k = k_*$. If $k < k_*$, it holds that $v_{ph} > v_{gr}$ (normal dispersion), and if $k > k_*$, it holds that $v_{ph} < v_{gr}$

(anomalous dispersion). The value of k_* is a function of the parameter δ . Numerical analysis shows that the range of the values for k_* is $0 \leq k_* < \sqrt{3}$. The maximum value of $k_* = \sqrt{3}$ is achieved for $\delta \rightarrow 1/9$.

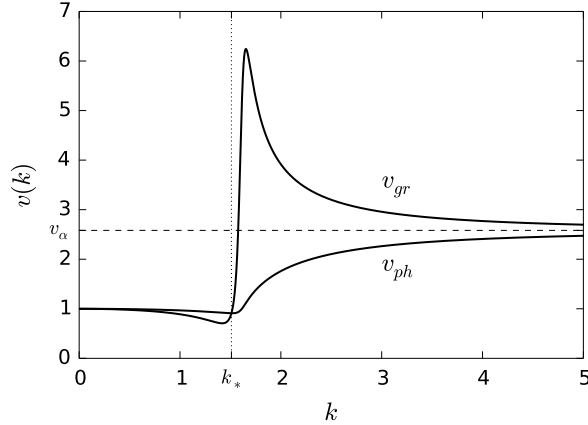


Figure 2.3: Phase and group velocities calculated for $\delta = 0.15$. The vertical dotted line at k_* separates the regions of normal and anomalous dispersion. The horizontal dashed line shows the limit of the velocities for large values of k .

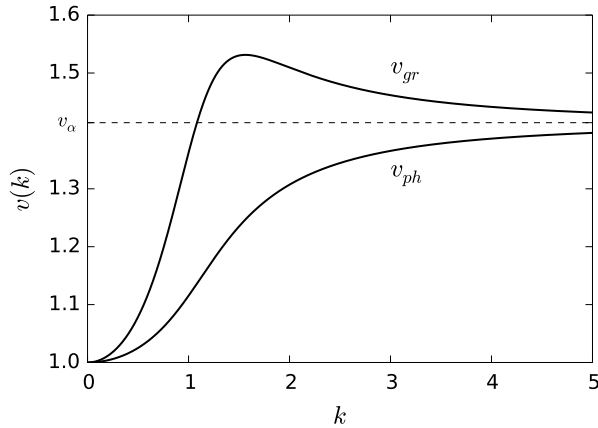


Figure 2.4: Phase and group velocities calculated for $\delta = 0.5$. The horizontal dashed line shows the limit of the velocities for large values of k .

For the value of $\delta \geq 0.2$ it was found that $k_* = 0$, and therefore the region of normal dispersion is completely absent and overtaken by the region of anomalous dispersion. Comparison of Figs. 2.3 and 2.4 shows a behaviour difference between the group and phase velocities for $\delta < 0.2$ and for $\delta > 0.2$.

2.2.3 Negative group velocity

Numerical analysis shows that the negative group velocity shown in Fig. 2.5 appears only in the region of normal dispersion if $0 < \delta < 0.1345$. The phenomenon of negative group velocity in the microstructured solids was also considered in Publications IV and V, which discuss the range of the physical parameters, that lead to the appearance of negative group velocity.

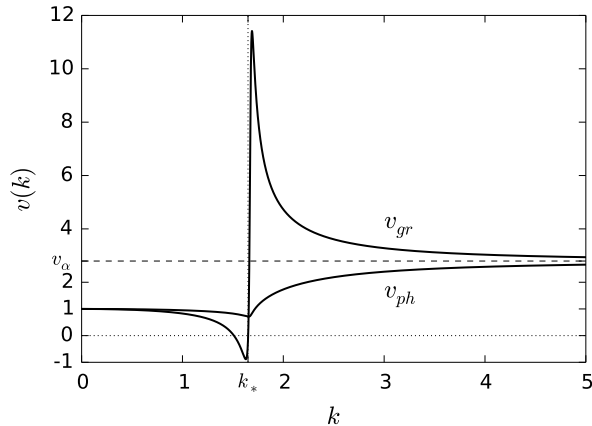


Figure 2.5: Phase and group velocities calculated for $\delta = 0.128$. The vertical dotted line at k_* separates the regions of normal and anomalous dispersion. The negative group velocity region is located to the left from k_* . The horizontal dashed line shows the limit of the velocities for large values of k .

It can be shown that as $\delta \rightarrow 0.1345$ the minimum of group velocity tends to zero. The existence of negative group velocity in the case of small values of δ is related to the stress-strain relaxation model in the form (2.3). In this case the hereditary amplitude $\gamma = 1 - \delta$ is close to its maximum, and therefore the hereditary features of the wool felt material are expressed most fully.

The effects of negative group velocity and anomalous dispersion are always *masked* by the relatively large influence of the exponential decay determined by $\mu(k)$. For example, the spectral wave components k that are associated with the strong anomalous dispersion regime ($\delta < 0.2$ and $k > k_*$) are also associated with the largest values of the exponential decay $\mu(k)$ (*vide* Fig. 2.2). This means that in this particular example, anomalous dispersion may be expressed only at the beginning of the wave evolution and only for a short period of time. Most probably, the anomalous dispersion will be overtaken by the normal dispersion regime, with which much smaller decay is associated.

2.3 Wave attenuation

The aim of this section is to study the rate of a strain pulse attenuation as it propagates along the x -axis through the felt material. This calls for the solution of the boundary value problem (BVP).

2.3.1 Boundary value problem

The solution to BVP is obtained numerically, by using the finite difference method (FDM). Instead of Eq. (2.11) a more suitable form of the equation for the finite difference approximation is considered. This form can be obtained by integrating Eq. (2.11) over time. This yields

$$\epsilon_{tt} = (\epsilon^p)_{xx} - \gamma \int_0^t (\epsilon^p)_{xx} e^{\xi-t} d\xi, \quad (2.27)$$

where $\gamma = 1 - \delta$. The BVP is solved over the non-negative space domain ($x \geq 0$). A boundary value of the strain prescribed at $x = 0$ is selected in the following form:

$$\epsilon(0, t) = A \left(\frac{t}{t_m} \right)^3 e^{3(1-t/t_m)}, \quad (2.28)$$

where t_m defines the time coordinate corresponding to the maximum of a pulse amplitude (peak of a pulse). This form of a pulse is continuous and smooth. At a pulse front the necessary conditions $\epsilon(0, 0) = \epsilon_t(0, 0) = \epsilon_{tt}(0, 0) = 0$ are met. Initially $t \leq 0$, the felt material is assumed to be at rest, thus $\epsilon(x, 0) = \epsilon_t(x, 0) = 0$.

Below the solution to the BVP (2.27), (2.28) is presented and analysed.

2.3.2 Pulse attenuation rate

Figure 2.6 shows the numerical solution of the BVP (2.27), (2.28) for the linear case, where $p = 1$. The evolution of the form of a pulse determined by the boundary value (2.28), where the boundary value parameter $t_m = 1/2$, is presented for three sequential time moments and for two different values of the material parameter δ . The dashed lines show the corresponding decays of the pulses' amplitudes. These decay curves are plotted through the maxima of the pulses and fitted to the exponential function in the form $e^{-\lambda_n x}$, where λ_n is the numerically found exponential decay constant. Here it is supposed that the dominant *fundamental* spectral component ω of a pulse (2.28) is estimated from a rough approximation $\omega t_m \simeq 1$.

In Publication III it is shown that the values of the decay constants λ_n calculated numerically and the decay constant $\lambda(\omega)$ taken from the dispersion relation are approximately equal. The derivation of the exponential

decay function (imaginary part of the dispersion relation) in the form $\lambda(\omega)$ is considered in Publication III. In principle this numerical approach can be used to verify the decay constant for any specific value of t_m rather accurately.

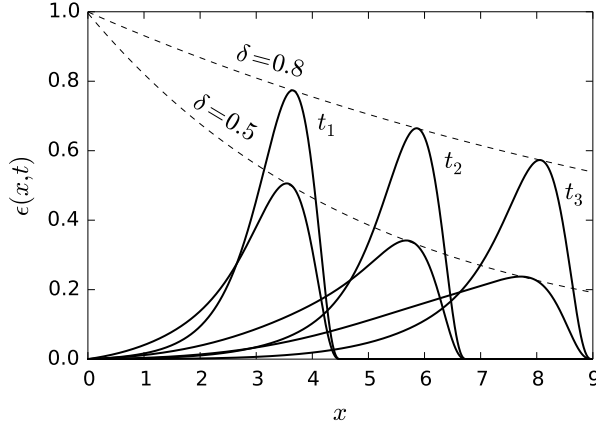


Figure 2.6: Snapshots of pulses' profiles shown for time moments $t_1 = 4.5$, $t_2 = 6.75$, and $t_3 = 9.0$, varying the value of the parameter δ . The boundary value parameter $t_m = 1/2$. The dashed lines show the amplitude decay. For $\delta = 0.8$, the corresponding amplitude decay function is $e^{-0.08x}$, for $\delta = 0.5$, the amplitude decay function is $e^{-0.20x}$.

2.4 Nonlinear analysis

In this section, the effects of the nonlinearity of the wool felt material on the evolution of an initial disturbance are considered. We examine the influence of the nonlinearity parameter p and the effect of an initial pulse amplitude on the evolution of a symmetrical pulse. The analysis is performed in connection with the numerical solution of the initial value problem (IVP).

2.4.1 Initial value problem

The IVP is solved over the non-negative time domain ($t \geq 0$) of the unbound half-space. The initial value of the strain prescribed at $t = 0$ is selected in the following form:

$$\epsilon(x, 0) = A \operatorname{sech}(\alpha x) = \frac{2A}{e^{\alpha x} + e^{-\alpha x}}, \quad (2.29)$$

$$\epsilon_t(x, 0) = \epsilon_x(x, 0) = 0, \quad (2.30)$$

where A is the amplitude and α is the space parameter.

Below, the numerical solution of the IVP in the form (2.27), (2.29), (2.30) is presented and analysed.

2.4.2 Influence of the nonlinearity parameter p

Figure 2.7 shows two solutions of the IVP (2.27), (2.29), (2.30), where only the nonlinearity parameter p is varied, while the other parameters are left constant. The solution of the problem is presented for four sequential time moments and for two values of the material parameter p .

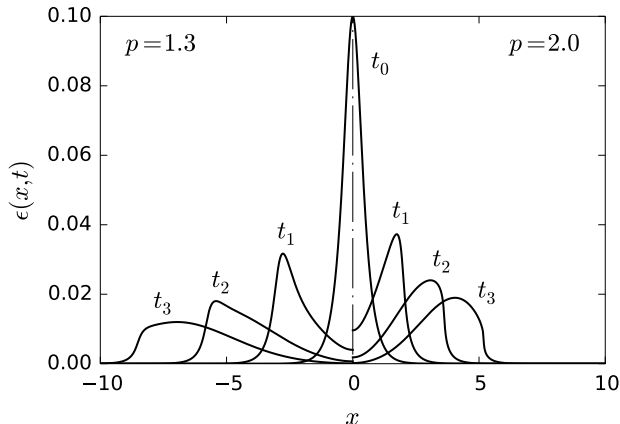


Figure 2.7: Snapshot of a pulse profile, where $\delta = 0.5$, $\alpha = 3$, and $A = 0.1$, shown for time moments $t_0 = 0$, $t_1 = 10/3$, $t_2 = 20/3$, and $t_3 = 30/3$, calculated for two different values of the parameter p .

The solution of the problem is symmetric with respect to $x = 0$, because the initial value (2.29) is an even bell-shaped function. The half of the solution where $p = 1.3$ is plotted to the left side from the axis of symmetry marked by the dot-dashed line in Fig. 2.7, and the half of the solution where $p = 2.0$ is plotted to the right side.

Figure 2.7 shows that the front part of a pulse becomes steeper as it propagates through the felt material. The process of the pulse steepening is greater for the felt with a larger value of the parameter p . The accumulation of this effect results in the eventual pulse breaking. This means that a shock wave will be formed, and the shock wave formation is brought to an earlier time for the larger values of p . In addition, a strong attenuation of the pulse amplitude with the progression of time is visible.

2.4.3 Influence of the initial amplitude

Figure 2.8 shows that the forward-facing slope of a pulse is strongly dependent on the pulse amplitude A . For larger amplitudes the maximum point or the peak of a pulse propagates faster than its front. This phenomenon prevails with the increasing of the amplitude of the bell-shaped initial value disturbance. The accumulation of this effect results in the eventual shock

wave formation. The progressive forward leaning of a propagating pulse can be explained by the fact that the group velocity is greater than the phase velocity. Also, these phenomena are related to the nonlinear features of the felt material.

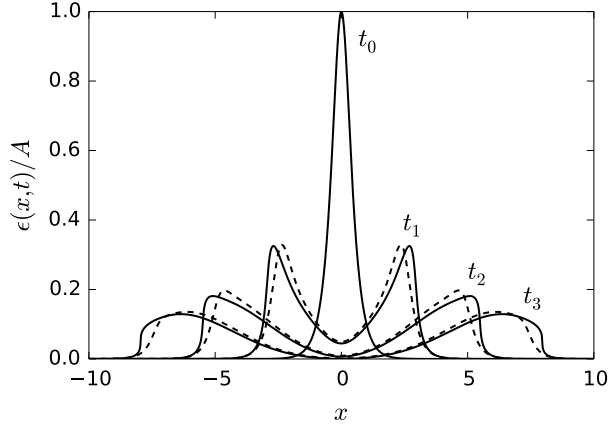


Figure 2.8: Normalized snapshots of pulses' profiles, where $\alpha = 3$, $\delta = 0.5$, and $p = 1.45$, shown for time moments $t_0 = 0$, $t_1 = 10/3$, $t_2 = 20/3$, and $t_3 = 30/3$. The profile starting with initial amplitude $A = 0.2$ is shown by the solid line. The profile starting with the initial amplitude $A = 0.02$ is shown by the dashed line.

Similar conclusions of the effects of the value of the parameter p and the initial amplitude A on the strain wave evolution can be drawn for the numerical solution of the BVP (2.27), (2.28), which is considered in Publication III.

3 Conclusions

Below the main conclusions of the first and the second part of the thesis and some final remarks are presented.

3.1 Termination–string dynamic interaction

The first part of the thesis, which is based on results that are derived in Publications I and II, introduced a novel model that is capable of reproducing the nonlinear effects of the *ideal* string vibration caused by the complex process of interaction between the string and the string termination. The proposed model is based on the travelling wave solution of the wave equation, which makes the method numerically reliable and highly stable. The accuracy of the computing method is determined only by the values of the discrete time and space mesh steps. The numerical experiments demonstrated that the lossless string vibrated in two distinct vibration regimes. In the beginning the string started to interact in a nonlinear fashion with the termination, and the resulting string motion was *aperiodic*. After some time of *aperiodic* vibration, the string vibration settled in a *periodic* regime, where the motion of the string was repetitious in time. The demonstration of the existence of these two vibration regimes is the main result of the first part of the thesis.

Additionally, the influence of the rigid termination on the string vibration and the resulting changes in the spectral structure were demonstrated and analysed. The effect of the amplitude of the string vibration on the mean level of high frequency modes was clearly evident, and this confirmed that the termination–string interaction was nonlinear indeed. Also, it was shown that the duration of the *aperiodic* vibration regime depended on the cross-section geometry of the termination. It was demonstrated that a minor geometric imperfection of the shape of the termination cross-section's profile elongated the duration of the *aperiodic* vibration regime significantly and produced noticeable changes in the string vibration spectrum. Comparison of the resulting spectra in the *periodic* vibration regime of the linear and nonlinear cases showed that the interaction of the string with the rigid termination widened the spectrum by transferring the energy of the low frequency modes to the high frequency vibration modes.

3.2 Deformation wave propagation in piano hammer felt

The second part of the thesis, which is based on the results derived in Publications III, IV (Section “Felt-type model”), and V, presented an analysis of a novel nonlinear felt model. The model equation takes into account the elastic and hereditary properties of the microstructured felt. It was used

to study the strain pulse evolution in the one-dimensional case. Linear and nonlinear analyses of the model were performed.

The numerical solution of the linear boundary value problem was used to estimate the rate of the amplitude decay of a strain pulse during its propagation through the felt. It was concluded that in the linear case the exponential decay constant could be obtained rather accurately by using dispersion analysis. The result of dispersion analysis also showed that both normal and anomalous dispersion types could exist in the wool felt material. It was demonstrated that for some values of the material parameters the negative group velocity region of the dispersion plot or the restrictive band-gap region of the dispersion plot (*vide* Publication V) or both would appear. Negative group velocity emerged always in connection with the region of normal dispersion.

The nonlinear effects of the general influence of the nonlinearity parameter p and the amplitude of the initial disturbance were demonstrated. It was shown that for the higher value of the parameter p the front of an evolving and propagating pulse became steeper, and this phenomenon was intensified with the growth of the value of the nonlinearity parameter p . It was also shown that the front slope of an evolving pulse was strongly determined by the pulse amplitude. A greater initial amplitude forced the peak of the wave pulse to propagate faster than the front of the pulse. Therefore, the accumulation of these nonlinear effects was eventually responsible for the formation of the discontinuity at the pulse front and the appearance of a shock wave. The most dominating feature of the felt was demonstrated to be the strong damping effect on any wave that was evolving and propagating through it.

The main results of the second part of the thesis are the following: the mathematical form of the novel constitutive relation and the equation of motion for the felt material were derived; the existence of negative group velocity in the linear case was proved.

3.3 Final remarks

The thesis focused on two nonlinear problems that are closely related to the processes of sound generation and formation of musical instruments such as grand pianos and Chikuzen biwas. These processes are the termination–string interaction and the impact of a piano hammer against the string, which can be understood through the detailed modelling of the deformation propagation in the felt material.

The proposed model of the termination–string interaction is based on a number of idealized and simplifying assumptions. The string was assumed to be *ideal* and the string’s termination was assumed to be absolutely rigid. Despite these assumptions the model clarified the underlying process of

the evolution of the termination–string dynamics. This simplified approach showed clearly how the shape of the cross-section profile of the termination influenced string vibration.

The analysis of the equation of motion of wool felt gave a fundamental insight into the mechanical and acoustical features and properties of the material. The felt coating is the characteristic part of the grand piano hammers. A good understanding of the wave propagation through the felt is necessary in order to start to grasp the complex process of the piano hammer–string interaction.

The results presented in this thesis are in no way final or conclusive. On the contrary, they represent the most basic and fundamental understanding of the otherwise complicated sound generation process of the aforementioned musical instruments. The results presented in the thesis may be applied for example in the digital physics-informed sound synthesis of such musical instruments.

References

- [1] A. Stulov, “Hysteretic model of the grand piano hammer felt,” *The Journal of the Acoustical Society of America*, vol. 97, no. 4, pp. 2577–2585, 1995.
- [2] T. Taguti and Y. K. Tohnai, “Acoustical analysis on the sawari tone of chikuzen biwa,” *Acoustical Science and Technology*, vol. 22, no. 3, pp. 199–208, 2001.
- [3] T. Taguti, “Sound production of sawari mechanism in biwa,” in *Proceedings of 18th International Congress on Acoustics*, (Kyoto, Japan), pp. 2119–2122, 2004.
- [4] H. A. Conklin Jr., “Design and tone in the mechanoacoustic piano. Part II. Piano structure,” *The Journal of the Acoustical Society of America*, vol. 100, no. 2, pp. 695–708, 2000.
- [5] M. Schatzman, “A hyperbolic problem of second order unilateral constraints: the vibrating string with a concave obstacle,” *Journal of Mathematical Analysis and Applications*, vol. 73, no. 1, pp. 138–191, 1980.
- [6] R. Burridge, J. Kappraff, and C. Morshedi, “The sitar string, a vibrating string with a one-sided inelastic constraint,” *SIAM Journal on Applied Mathematics*, vol. 42, no. 6, pp. 1231–1251, 1982.

- [7] H. Cabannes, “Presentation of software for movies of vibrating strings with obstacles,” *Applied Mathematics Letters*, vol. 10, no. 5, pp. 79–84, 1997.
- [8] A. Krishnaswamy and J. O. Smith, “Methods for simulating string collisions with rigid spatial obstacles,” in *Proceedings of IEEE Workshop on Applications of Signal Processing to Audio and Acoustics*, (New Paltz, NY, USA), pp. 233–236, 2003.
- [9] S. M. Han and M. A. Grosenbaugh, “Non-linear free vibration of a cable against a straight obstacle,” *Journal of Sound and Vibration*, vol. 237, pp. 337–361, 2004.
- [10] S. Bilbao, A. Torin, and V. Chatziioannou, “Numerical modeling of collisions in musical instruments,” *Acta Acustica United with Acustica*, pp. 1–18, 2014. Submitted.
- [11] S. Bilbao, “Numerical modeling of string/barrier collision,” in *Proceedings of International Symposium on Musical Acoustics (ISMA 2014)*, (Le Mans, France), pp. 1–6, 2014.
- [12] T. Taguti, “Numerical simulation of vibrating string subject to sawari mechanism,” in *Proceedings of 19th International Congress on Acoustics*, (Madrid, Spain), pp. 1–6, 2007.
- [13] T. Taguti, “Dynamics of simple string subject to unilateral constraint: A model analysis of sawari mechanism,” *Acoustical Science and Technology*, vol. 29, no. 3, pp. 203–214, 2008.
- [14] C. P. Vyasarayani, S. Birkett, and J. McPhee, “Modeling the dynamics of a vibrating string with a finite distributed unilateral constraint: Application to the sitar,” *The Journal of the Acoustical Society of America*, vol. 125, no. 6, pp. 3673–3682, 2009.
- [15] E. Rank and G. Kubin, “A waveguide model for slapbass synthesis,” in *Proceedings of IEEE International Conference on Acoustics, Speech, and Signal Processing*, (Munich, Germany), pp. 443–446, 1997.
- [16] G. Evangelista and F. Eckerholm, “Player–instrument interaction models for digital waveguide synthesis of guitar: touch and collisions,” *IEEE Transactions on Audio, Speech, and Language Processing*, vol. 18, no. 4, pp. 822–832, 2010.
- [17] S. Siddiq, “A physical model of the nonlinear sitar string,” *Archives of Acoustics*, vol. 37, no. 1, pp. 73–79, 2012.

- [18] C. V. Raman, “On some Indian stringed instruments,” *Proceedings of the Indian Association for the Cultivation of Science*, vol. 7, pp. 29–33, 1921.
- [19] D. E. Hall, “Piano string excitation IV: The question of missing modes,” *The Journal of the Acoustical Society of America*, vol. 82, no. 6, pp. 1913–1918, 1987.
- [20] A. Stulov, “Experimental and computational studies of piano hammers,” *Acta Acustica United with Acustica*, vol. 91, no. 6, pp. 1086–1097, 2005.
- [21] N. H. Fletcher and T. D. Rossing, *The Physics of Musical Instruments*. United States of America: Springer, 1998.
- [22] J. O. Smith, “Physical modeling using digital waveguides,” *Computer Music Journal*, vol. 16, no. 4, pp. 74–91, 1992.
- [23] V. Välimäki, J. Pakarinen, C. Erkut, and M. Karjalainen, “Discrete-time modelling of musical instruments,” *Reports on Progress in Physics*, vol. 69, no. 1, pp. 1–78, 2006.
- [24] J. O. Smith, *Physical Audio Signal Processing for Virtual Musical Instruments and Audio Effects*. W3K Publishing, 2010.
- [25] A. Stulov, “Dynamic behavior and mechanical features of wool felt,” *ACTA Mechanica*, vol. 169, no. 1–4, pp. 13–21, 2004.
- [26] D. E. Hall, “Piano string excitation VI: Nonlinear modeling,” *The Journal of the Acoustical Society of America*, vol. 92, no. 1, pp. 95–105, 1992.
- [27] A. Stulov, “Physical modeling of the piano string scale,” *Applied Acoustics*, vol. 69, no. 11, pp. 977–984, 2008.
- [28] Y. N. Rabotnov, *Elements of Hereditary Solid Mechanics*. Moscow: MIR Publishers, 1980. Chap. 17.

Acknowledgements

The author expresses sincere gratitude to his supervisor Anatoli Stulov. Without his active support this thesis would have never materialized. In addition, co-authors of papers included in the thesis are gratefully acknowledged – their contributions to these works have been invaluable.

The author is greatly indebted to the following persons for their valuable advice and kindly provided support during the different stages of the author’s doctoral studies: Prof. Jüri Engelbrecht (Institute of Cybernetics at TUT), Prof. Aleksander Klauson (Institute of Mechanics at TUT), Prof. Vesa Välimäki (Department of Signal Processing and Acoustics at Aalto University), Assoc. Prof. Mihhail Klopov (Institute of Physics at TUT), Dr. Jaan Kalda (Institute of Cybernetics at TUT), Dr. Julian Parker (current affiliation: Native Instruments, Berlin, Germany), Dr. Heidi-Maria Lehtonen (current affiliation: Dolby Laboratories, Stockholm, Sweden), Dr. Tanel Peets (Institute of Cybernetics at TUT), Dr. Kert Tamm (Institute of Cybernetics at TUT), Prof. Jaan Janno (Institute of Mathematics at TUT), Assoc. Prof. Balázs Bank (Faculty of Electrical Engineering and Informatics at Budapest University of Technology and Economics), and Aigar Vaigu (Metrology Research Group at Aalto University).

Special thanks go to the anonymous reviewers of the research papers included in the thesis for their volunteered time and energy. In the author’s opinion the reviewers’ comments and remarks were always helpful and constructive.

Financial support from the Archimedes Foundation (several Kristjan Jaak and DoRa programme 8 scholarships), the European Regional Development Fund (Project TK124 (CENS)), the Institute of Cybernetics at TUT, the Aalto University funding scheme for infrastructure, and the Estonian Ministry of Education and Research (SF 0140077s08) is greatly appreciated. Any factual errors and omissions in the thesis remain the author’s sole responsibility.

Abstract

The thesis focuses on two nonlinear problems that are closely related to the sound production mechanism of musical instruments such as grand pianos, biwas, and sitars.

The first part of the thesis considers the string motion in which the string displacement is unilaterally constrained by the rigid termination with an arbitrary cross-section profile geometry. A model based on the travelling wave solution is proposed for simulating the nonlinear interactions between the vibrating string and the termination. It is shown that the lossless *ideal* string vibrates in two distinct vibration regimes. In the beginning the string starts to interact continuously with the termination, resulting in the *aperiodic* motion of the string. Consequently, the spectrum of the string motion depends on the amplitude of the string vibration, and its spectral structure changes continuously with the progression of time. The duration of the *aperiodic* vibration regime depends on the geometry of the termination. After some time of the *aperiodic* vibration, the string vibration settles in a *periodic* regime, where the string motion is repetitious in time.

The second part of the thesis explores the mechanical and acoustical features of the felt that is used in piano hammer manufacturing. A one-dimensional nonlinear constitutive relation of the wool felt material is derived based on the experimental data of testing the piano hammers. This relation enabled deriving a nonlinear partial differential equation of motion with the third order terms that takes into account the elastic and hereditary properties of the microstructured wool felt. The equation of motion is then used to study the evolution of the initial disturbance in the felt material. The physical dimensionless material parameters are established and their importance in describing the nonlinear effects is discussed. The initial and boundary value problems are considered and the numerical solution describing the nonlinear wave propagation is provided. It is demonstrated that the nonlinearity makes the front slope of a propagating pulse steeper, which causes an eventual breaking of the wave. In addition, the rate of the wave attenuation in the felt material is estimated. Also, a detailed dispersion analysis of the corresponding linear problem is provided. It is shown that both normal and anomalous dispersion types exist in the wool felt material and that for certain values of the physical parameters negative group velocity will appear.

The results presented in the thesis clarify the physics behind the nonlinear sound generation mechanisms of musical instruments such as grand pianos, biwas, shamisens, and veenas.

Resümee

Doktoritöö käsitleb kahte mittelineaarset probleemi, mis on lähedalt seotud selliste muusikaliste instrumentide nagu näiteks tiibklaver, biwa ja sitari helitekke protsessidega.

Doktoritöö esimeses osas vaadeldakse keele võnkumist olukorras, kus keele üks otstest on ühepoolselt piiratud jäiga piirajaga, mille ristlõike kuju võib omada meelevaldset geometriat. Mudelit, mis põhineb lainevõrrandi d'Alembert'i lahendil, kasutatakse keele ja piiraja vahelise mittelineaarsust esile kutsuva interakteerumise simuleerimiseks. Doktoritöös näidatakse, et kadudeta võnkuv ideaalne keel võngub kahes selgelt eristuvast võnkumise režiimis. Võnkumise alguses interakteerub keel piirajaga mittelineaarsel moel, mille tulemuseks on keele *aperioodiline* võnkumine. Siit järeldub, et keele võnkumise spekter sõltub keele võnkeamplituudist ning spektri struktuur *aperioodilises* režiimis on pidevas muutumises. *Aperioodilise* võnkerežiimi ajaline kestus sõltub piiraja ristlõike kujust. Peale selle võnkerežiimi möödumist hakkab keel võnkuma *perioodiliselt*.

Doktoritöö teine osa uurib villast valmistatud vildi, mida kasutatakse tiibklaveri haamrite tootmises, mehaanilisi ja akustilisi omadusi. Kasutades klaveri haamrite uuringutest saadud katseandmeid, koostatakse vildi materjali ühedimensiooniline mittelineaarne olekuvõrrand, mis võtab arvesse nii mikrostruktuurse vildi elastsed kui ka hüstereetilised omadused. Seda olekuvõrrandit omakorda kasutatakse liikumisvõrrandi koostamiseks. Matemaatiliselt on tegu mittelineaarse kolmandat järku osatuletistega diferentsiaalvõrrandiga. Vildi materjali mittelineaarseid omadusi uuritakse materjali dimensioonitute parameetrite abil. Liikumisvõrrandi numbrilise lahendi abil uuritakse deformatsioonilainete levimise evolutsiooni ühedimensioonilises seades. Numbriline lahend näitab, et mittelineaarsus muudab vildis leviva laine frondi järsemaks ning lõpuks on mittelineaarsus vastutav lööklaine tekkimise eest. Lisaks kvantifitseeritakse leviva laine impulsi sumbumise kiirus. Teostatakse üksikasjalik dispersioonianalüüs. Analüüsist selgub, et lainelevil vildis esinevad nii normaalse kui ka anomaalse dispersiooni tüübid ning et teatud materjali parameetrite väärtuste juures eksisteerib negatiivne rühmakiirus.

Doktoritöös esitatud tulemused lisavad selgust selliste muusikariistade nagu biwa, shamiseni ja tiibklaveri helitekke protsesse kirjeldavasse füüsikasse.

Appendix A

PUBLICATIONS

Publication I

A. Stulov and D. Kartofelev,

“Vibration of strings with nonlinear supports,”

Applied Acoustics, vol. 76, pp. 223–229, February 2014.

DOI: 10.1016/j.apacoust.2013.08.010



Vibration of strings with nonlinear supports

Anatoli Stulov*, Dmitri Kartofelev

Centre for Nonlinear Studies, Institute of Cybernetics at Tallinn University of Technology, Akadeemia 21, 12618 Tallinn, Estonia



ARTICLE INFO

Article history:

Received 29 October 2012
Received in revised form 21 May 2013
Accepted 13 August 2013

Keywords:

Grand piano
String vibration
Unilateral constraints
Hammer–string interaction
Numerical simulation

ABSTRACT

The dynamic string motion, which displacement is unilaterally constrained by the rigid termination condition of an arbitrary geometry has been simulated and analyzed. The treble strings of a grand piano usually terminate at a capo bar, which is situated above the strings. The apex of a V-shaped section of the capo bar defines the end of the speaking length of the strings. A numerical calculation based on the traveling wave solution is proposed for modeling the nonlinearity inducing interactions between the vibrating string and the contact condition at the point of string termination. It was shown that the lossless string vibrates in two distinct vibration regimes. In the beginning the string starts to interact in a nonlinear fashion with the rigid terminator, and the resulting string motion is aperiodic. Consequently, the spectrum of the string motion depends on the amplitude of string vibrations, and its spectral structure changes continuously with the passage of time. The duration of that vibration regime depends on the geometry of the terminator. After some time of aperiodic vibration, the string vibrations settle in a periodic regime where the resulting spectrum remains constant.

© 2013 Elsevier Ltd. All rights reserved.

1. Introduction

Investigation of the boundary condition of vibrating string is a very important problem in musical acoustics. It is well known that the fundamental frequency of the string is strictly determined by the type of the string termination. Usually the changing of the tone caused by the curvature of the string support is negligible, but there is a family of Japanese plucked stringed instruments (*biva* and *shamisen*), which sounding is strictly determined by the string termination [1,2]. These lutes are equipped with a mechanism called “*sawari*” (touch). The *sawari* is a contact surface of very limited size, located at the nut-side end of the string, to which the string touches repeatedly, producing a unique timbre of the instrumental tone called the *sawari* tone.

There are other stringed instruments of Indian origin with a similar bridge design, such as sitar, veena and tambura. The interaction of the string with a curved string support creates a peculiar buzzing sound, which is markedly different from that of known European plucked string instruments such as guitar and lute. The geometry of the string terminations for the sitar, veena, and tambura was considered by Raman [3]. Raman concluded that possible explanation of the phenomena of the “missing modes” is the complex interaction of the string with the bridge [4].

Much effort has been devoted to modeling the dynamics of a vibrating string with a distributed unilateral constraint during the past decades. This problem was considered by Schatzman [5],

Burridge et al. [6], and Cabannes [7] who used the method of characteristics, and assumed that the string does not lose energy when it hits the obstacle. Krishnaswamy and Smith [8], Han and Groesenbaugh [9], and Taguti [10] used a finite difference method to study the string interaction with the curved bridge. Vyasrayani et al. [11] described the movement of the sitar string with a set of partial differential equations. Rank and Kubin [12], Evangelista and Eckerholm [13], and Siddiq [14] used a waveguide modeling approach to study the plucked string vibration with nonlinear limitation effects.

The present paper describes a physics-based model for simulation of vibrations of piano string, which at one end has the ideal rigid support, and its other end is terminated at a capo bar. The types of the string support in the piano are different for the bass and treble notes. All the far ends of the piano strings are terminated at the bass and treble bridges, which are rather complicated resonant systems. The nearest ends of the bass and long treble strings begin at the agraffe that can be considered as an absolutely rigid clamp termination. However the treble strings of grand pianos start at the capo bar – the rigid edge of the cast iron frame [15]. These strings are bent around the capo bar, and their vibration tone depends on the curvature of the capo bar V-shaped section. The same type of the string support can be seen also on the guitar and some other musical string instruments.

The aim of this paper is to show the influence of the contact nonlinearity on the spectral structure of the piano string vibration. A part of this analysis was presented in [16]. The study is divided into two stages. Firstly, the mathematical modeling of the hammer–string interaction enables prediction of the piano string

* Corresponding author.

E-mail addresses: stulov@ioc.ee, anstulov@gmail.com (A. Stulov).

motion [17,18]. Secondly, this knowledge is used for appropriate simulation of interaction of the vibrating string with a capo bar.

The numerical simulation of the hammer–string interaction is based on the physical models of a piano hammer described in [19–21]. These models are based on the assumption that the woolen hammer felt is a microstructural material possessing history-dependent properties. The elastic and hereditary parameters of piano hammers were obtained experimentally using a special piano hammer testing device that was developed and built in the Institute of Cybernetics at Tallinn University of Technology [21].

In this paper a number of simplifying assumptions regarding the string and string support are introduced. Thus, the piano string is assumed to be an ideal flexible string, the coupling of strings at the end supports is neglected, and the bridge motion is ignored. We also assume that the right string termination (bridge) is the ideal rigid support. The left string termination (capo bar, *sawari*) is considered here as a rigid but not an ideal support, because we take into account the curvature of its V-shaped section. Nevertheless, we hope that the application of the proposed model will clarify the physics of vibration of the string with nonlinear support.

2. First stage. String with ideal rigid support

2.1. Piano string model

It is assumed that the piano string is an ideal (flexible) string. The transverse displacement $y(x,t)$ of such a string obeys wave equation

$$\frac{\partial^2 y}{\partial t^2} = c^2 \frac{\partial^2 y}{\partial x^2}. \tag{1}$$

Like in [17,18], we have the system of equations describing the hammer–string interaction

$$\frac{dz}{dt} = -\frac{2T}{cm}g(t) + V, \tag{2}$$

$$\frac{dg}{dt} = \frac{c}{2T}F(t), \tag{3}$$

where function $g(t)$ is the form of outgoing wave created by the hammer strike at the contact point $x = l$, c is the speed of a nondispersive wave traveling along the string; $F(t)$ is the acting force, T is the string tension; m , $z(t)$, and V are the hammer mass, the hammer displacement, and the hammer velocity, respectively. The hammer felt compression is defined by $u(t) = z(t) - y(l,t)$. Function $y(l,t)$ describes the string transverse displacement at the contact point $x = l$, and is given by [18]

$$y(l,t) = g(t) + 2 \sum_{i=1}^{\infty} g\left(t - \frac{2iL}{c}\right) - \sum_{i=0}^{\infty} g\left[t - \frac{2(i+a)L}{c}\right] - \sum_{i=0}^{\infty} g\left[t - \frac{2(i+b)L}{c}\right]. \tag{4}$$

Here we suppose that the string of length L extends from $x = 0$ on the left to $x = L$. Parameter $a = l/L$ is the fractional length of the string to the striking point, and $b = 1 - a$. Parameter a determines the actual distance l of the striking point from the nearest string end. The initial conditions at the moment when the hammer first contacts the string, are taken as $g(0) = z(0) = 0$, and $dz(0)/dt = V$.

The physical interpretation of Eq. (4) is simple enough. It describes the deflection of the string at the contact point that is determined by the traveling waves moving in both directions along the string and reflecting back from the string supports. Here the index of summation i simply denotes the number of reflections.

2.2. Piano hammer model

The experimental testing of piano hammers demonstrates that all hammers have a hysteretic type of force-compression characteristics. A main feature of hammers is that the slope of the force-compression characteristics is strongly dependent on the rate of loading. It was shown that nonlinear hysteretic models can describe the dynamic behavior of the hammer felt [19–21]. These models are based on assumption that the hammer felt made of wool is a microstructural material possessing history-dependent properties. Such a physical substance is called either a hereditary material or a material with memory.

According to a three-parameter hereditary model of the hammer presented in [20], the nonlinear force $F(t)$ exerted by the hammer is related to the felt compression $u(t)$ by the following expression

$$F(u(t)) = Q_0 \left[u^p + \alpha \frac{d(u^p)}{dt} \right]. \tag{5}$$

Here the parameter Q_0 is the static hammer stiffness; p is the compliance nonlinearity exponent, and α is the retarded time parameter.

The continuous variations in hammer parameters across the compass of the piano were obtained experimentally by measuring a whole hammer set of recently produced unvoiced *Abel* hammers. The result of those experiments is presented in [20,21]. A best match to the whole set of hammers $1 \leq n \leq 88$ was approximated using

$$Q_0 = 183 \exp(0.045n), \tag{6}$$

$$p = 3.7 + 0.015n, \tag{7}$$

$$\alpha = 259.5 + 0.58n + 6.6 \cdot 10^{-2}n^2 - 1.25 \cdot 10^{-3}n^3 + 1.172 \cdot 10^{-5}n^4. \tag{8}$$

Here the unit for parameter α is ms, and the unit for Q_0 is N/mm^p.

The hammer masses of this set were approximated by

$$m = 11.074 - 0.074n + 10^{-4}n^2, \quad 1 \leq n \leq 88. \tag{9}$$

The mass of hammer 1 (A_0) is 11.0 g, and the mass of hammer 88 (C_8) 5.3 g.

2.3. Numerical simulation for tone A7

The hammer–string interaction is simulated by solving the system of Eqs. (2, 3) for various initial hammer velocities. We chose for calculations the note number $n = 85$ (tone A_7 , frequency $f = 3520$ Hz). The string parameters are the following: the string length $L = 61$ mm; the actual distance of the striking point from nearest string end $l = 2.6$ mm; the linear mass density of the string $\mu = 4.2$ g/m; the string mass $M = 0.26$ g; the string tension $T = 774.6$ N.

For tone A_7 in grand pianos there are three strings per note, the acting mass of a hammer defined by relation (9) for $n = 85$ is chosen equal to 1/3 of the total hammer mass, and thus $m = 1.8$ g. For the hammer 85 we use the following additional parameters: static stiffness $Q_0 = 8387.4$ N/mm^p; nonlinearity exponent $p = 4.975$; hereditary parameter $\alpha = 0.5312$ ms.

As a result of simulation of a hammer–string interaction we can find the history of the acting force $F(t)$ and the time dependence of the outgoing wave $g(t)$ created by the hammer strike, which are shown in Fig. 1.

At the moment $t = t_0$, which is defined as the duration of contact, the hammer has lost the contact with the string. After this moment the acting force $F(t) = 0$ for any time $t > t_0$. Therefore, according to Eq. (3), the outgoing wave $g(t) = const$ for the moments $t > t_0$.

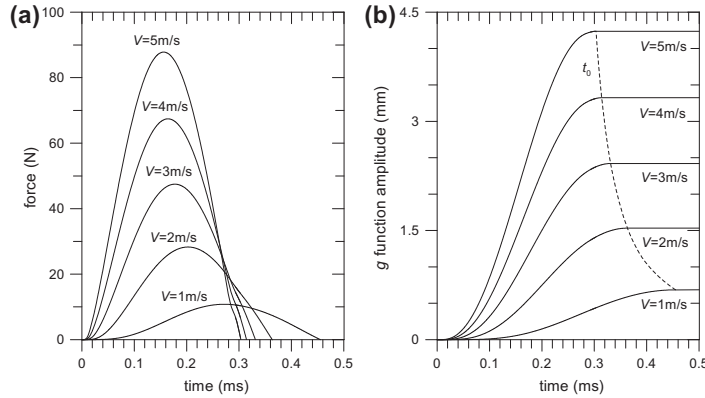


Fig. 1. Force (a) and g function (b) histories computed for tone A_7 ($n = 85, f = 3520$ Hz). The dashed line on (b) defines duration of contact t_0 .

3. Second stage. A string with a nonlinear support

3.1. Capo bar–string interaction

The treble strings of grand pianos usually terminate at a capo bar, and the apex of a V-shaped section of the capo bar defines the end of the speaking length of the strings. The V-shaped section of the capo bar has approximately a parabolic form, and it is described here by the function $W(x) = (2R)^{-1}x^2$, where R is the radius of the capo bar curvature at $x = 0$.

The proposed model of the capo bar–string interaction is based on the knowledge of the outgoing wave function $g(t)$ created by the hammer strike. It is evident that Eq. (1) may be satisfied by combination of simple nondispersive waves $g_1(t - x/c)$ and $g_2(t + x/c)$ moving in either directions along the string from the point $x = l$ where the string makes contact with the hammer. At this point $g_1(t) = g_2(t) = g(t)$. These two waves g_1 and g_2 are simply translation of outgoing wave $g(t)$ from the point $x = l$ to the other segments of the string, and their amplitudes are always positive, because $g(t) > 0$ in our case.

These two waves reflect from each end of the string. The wave $g_1(t - x/c)$ moving to the right creates the wave $g_4(t + x/c)$ moving to the left, and the wave $g_2(t + x/c)$ moving to the left creates the wave $g_3(t - x/c)$ moving to the right. The scheme of waves propagation along the string is shown in Fig. 2. According to our model, the string deflection $y(x, t)$ (shown in Fig. 2 by marked solid line) at any point x and at any time t is simply the resulting sum of waveforms g moving in both directions:

$$y(x, t) = g_1(t - x/c) + g_2(t + x/c) + g_3(t - x/c) + g_4(t + x/c). \quad (10)$$

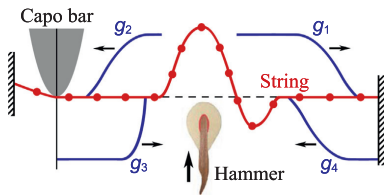


Fig. 2. Scheme of capo bar–string interaction. Functions g are the traveling waves.

At the right end of the string $x = L$ we have an ideal rigid string support. The boundary condition $y(L, t) = 0$ at this end of the string will be satisfied if the reflected wave $g_4(t + L/c) = -g_1(t - L/c)$, therefore this type of string termination is called here the ideal support (IS) of the string.

However, at the left end of the string the reflection of wave $g_2(t)$ is more complicated. Here we suppose that the capo bar is also ideal rigid, and thus its surface restricts the amplitude of the string deflection, when the string moves up. This type of string termination is called here the nonlinear termination (NT) of the string. We assume also that the reflecting wave $g_3(t - x/c)$ moving to the right appears only at the point $x = x_*$, where the amplitude of the string deflection $y(x_*, t) \geq W(x_*)$. The position of this point x_* is determined by the V-shape form $W(x)$ of the capo bar. At this point $x = x_*$ we must have $y(x_*, t) = W(x_*)$, and this condition results in the appearance of reflected wave $g_3(t - x_*/c) = W(x_*) - y(x_*, t)$. Thus the amplitude of the string deflection, which is determined by Eq. (10) in vicinity of the capo bar never exceeds the value $W(x)$.

The process of reflection of newly created traveling waves g_3 and g_4 from the respective ends of the string is described by the same procedure. The physical interpretation of the functions g_3 and g_4 determines what we should use for their values: they exist only because the outgoing wave g at some earlier time has been reflected from the string ends. We must mention also that the amplitudes of reflected waves $g_3(t - x/c)$ and $g_4(t + x/c)$ are always negative.

A computing method that realizes the calculation of the string deflection determined by Eq. (10) is based on a digital delay-line procedure. The numerical application of this method is best explained by Hall [17] in Appendix A.

In illustrative Fig. 3 we demonstrate the form of the string in vicinity of the capo bar during the reflection of the single wave $g_2(t - x/c)$ only. Using the procedure described above, the string deflection as function of the nondimensional distance along the string is computed for three consequent nondimensional ($c = 1$) moments of time. At the moment $t = t_1$ the form of the string is determined by the traveling wave g_2 only. At the next moment $t = t_2$ the segment (1,2) of the string is in contact with the surface of the capo bar, and the reflected wave $g_3(t_2)$ has appeared. This form of the string is shown by solid line marked with crosses. At the moment $t = t_3$ the string is in contact with the surface of the capo bar on the segment (3,4). The form of the string at this moment is shown by solid line marked with solid circles, and the reflected wave $g_3(t_3)$ is also shown by the dashed line. Thus at some

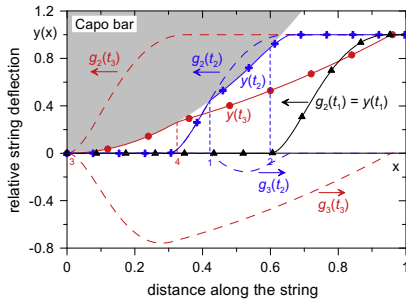


Fig. 3. The traveling waves g_i (dashed lines), and the forms of the string (solid lines marked by signs) shown for consequent nondimensional moments of times $t_1 = 0.4$; $t_2 = 0.7$; $t_3 = 1.0$. The configuration of the capo bar is shaded.

moments the string “clings” to the capo bar, and during that time the form of the string on some segment simply repeats the form of the V-shaped section of the capo bar.

3.2. String motion spectrum

If the string has the ideal rigid support, then the spectrum of the string motion excited by the hammer may be calculated directly from the force history $F(t)$ [17]. The general expression for the string mode energy level is

$$E_i = 10 \log \left[\frac{2M\omega_i^2}{mV^2} (A_i^2 + B_i^2) \right], \tag{11}$$

where

$$A_i = \frac{\sin(i\pi\tau)}{i\pi c\mu} \int_0^{t_0} F(s) \cos(\omega_i s) ds, \tag{12}$$

$$B_i = \frac{\sin(i\pi\tau)}{i\pi c\mu} \int_0^{t_0} F(s) \sin(\omega_i s) ds. \tag{13}$$

Here $\omega_i = \pi i c L^{-1} = i\omega_0$ is the string mode angular frequency; t_0 is the contact time. After the moment $t \geq t_0$, when the hammer has left the string and it vibrates freely, the spectrum of the string vibrations does not change in time.

In our case one end of the string has nonlinear termination. Consequently, the spectrum of the string motion depends on the amplitude of the string vibrations, and its spectral structure changes continuously over time, even after the moment $t = t_0$.

We consider the outgoing wave $g(t)$ generated by the hammer strike as the initial local disturbance of the string motion, which creates a sequence of pulses g_n ($n = 1, 2, 3, 4$). Using the procedure, which describes the capo bar–string interaction, we can determine and assume the string deflection $y(x, t_0)$ as an initial condition of the string vibration. The initial string velocity $v(x, t_0)$ at this moment can be found using the string displacement $y(x, t_0 - \Delta)$ at some earlier time, where $\Delta = t_i - t_{i-1}$ is the discrete time step of numerical simulation. Then, the initial string velocity can be determined as

$$v(x, t_0) = \left. \frac{\partial y}{\partial t} \right|_{t=t_0} = \frac{y(x, t_0) - y(x, t_0 - \Delta)}{\Delta}. \tag{14}$$

Now using Fourier analysis we can find the spectrum of the string vibrations. If

$$y(x, t) = \sum_i (A_i \cos \omega_i t + B_i \sin \omega_i t) \sin \left(\frac{i\pi x}{L} \right), \tag{15}$$

with normal-mode frequencies $\omega_i = i\omega_0$, then

$$A_i = \frac{2}{L} \int_0^L y(x, t_0) \sin \left(\frac{i\pi x}{L} \right) dx, \tag{16}$$

$$B_i = \frac{2}{L\omega_i} \int_0^L v(x, t_0) \sin \left(\frac{i\pi x}{L} \right) dx, \tag{17}$$

and the string mode energy level E_i of the i th mode is also defined by Eq. (11).

4. Results and analysis

4.1. Vibration of the string terminated at the capo bar

In the previous Section, the traveling wave functions g were computed for tone A_7 , and for various initial hammer velocities. Now, using the model of the capo bar–string interaction we can investigate the effect of contact nonlinearity on the string motion, and on the spectral structure of the piano string vibration.

In Fig. 4 we demonstrate the changes of the string deflection over time, computed for initial hammer velocity $V = 5$ m/s, and for the capo bar curvature $R = 15$ mm. Here we can compare the forms of the piano string vibration with and without a capo bar. At the moment t_0 the hammer has just lost the contact with the string, and the left end of the string had contacted with a capo bar surface only once. At this moment there is a small difference between the string forms, shown by solid and dashed lines without marks. The period of the string vibrations for tone A_7 is equal to $T_0 = 0.284$ ms. Therefore, at the moment t_1 the left end of the string had contacted a capo bar surface 13 times, and at the moment t_2 there had been 21 contacts between the string and a capo bar.

The examples of the dynamic string motion are available for viewing at the supplementary web page of this article [22]. This computer animation of the string vibration also shows in details how the string “clings” to the capo bar surface during the first moments ($t < 0.25$ ms).

Visual inspection of the string’s movement shows that the influence of the capo bar is noticeable during approximately first 15–20 interactions between the string and the capo bar. After this moment ($t \approx 6$ ms, in our case), vibration of the string terminated at the capo bar may be considered as periodical, likewise as a vibration of the string with IS.

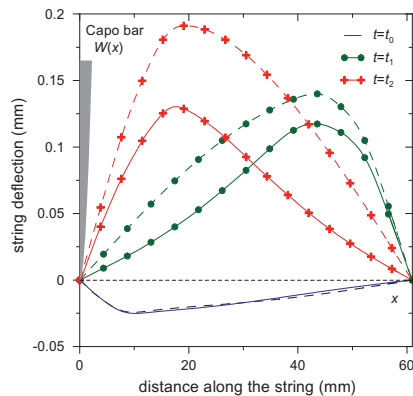


Fig. 4. String forms computed for different time moments $t_0 = 0.3$ ms, $t_1 = 3.86$ ms, $t_2 = 6.21$ ms. The solid lines show the string with NT; the dashed lines show the string with IS. The shaded area is the capo bar.

This phenomenon can be observed also through the string vibration spectra. Fig. 5 shows the spectra corresponding to the same string vibrations, which are shown in Fig. 4.

At the first moment $t = t_0$ there is only a small difference between the spectra of the strings vibrations. After this moment the spectrum of the string with IS, according to expressions (11)–(13), is the stationary, or not a time dependent spectrum. On the contrary, the spectrum of the string with NT changes continuously over time, even when the string vibrates freely. The effect of the capo bar continues for approximately 6 ms, and after this moment the spectrum becomes stationary as well. During this time period the level of first five modes decreases systematically. The difference between the levels of 4th mode for IS and NT cases is equal to 6 dB. Undoubtedly, here one can see the energy transition from low to high modes. The power spectrum of the string vibration is enriched by spectral components up to very large numbers, and the mean level of some high modes gains up to 15 dB. The modes number 22 ($t = t_0$), and number 23 ($t = t_2$) are not shown in Fig. 5 due to their extremely low energy level (less than 90 dB). These modes are the “missing modes” [4], due to the fact that for our string the striking point is located approximately at distance $l = L/N$, where integer $N = 23$.

Fig. 6 demonstrates the changing of the string vibration spectra with variation of the amplitude of the string excitation. The results are presented for the capo bar curvature $R = 15$ mm, and for the time moment $t = 6.21$ ms. It is evident that with increasing of the amplitude of the string vibrations the mean level of high modes grows up, and this phenomenon confirms that the interaction between the capo bar and the string is indeed nonlinear. For the hammer striking velocity $V = 5$ m/s the mode number 23 is also the “missing mode”.

The effect of the capo bar curvature on the spectra of the string vibrations is shown in Fig. 7. The results are presented for the initial hammer velocity $V = 5$ m/s, and for the time moment $t = 6.21$ ms. The mode number 22 ($R = 15$ mm) is also the “missing mode”, and its energy level is less than 85 dB. Analyzing the results presented in Fig. 7 we can state, that the increasing of the capo bar curvature gains the energy of high modes, and thus, with the suggested model it is possible to imitate the energy transfer from the lower to the higher partials.

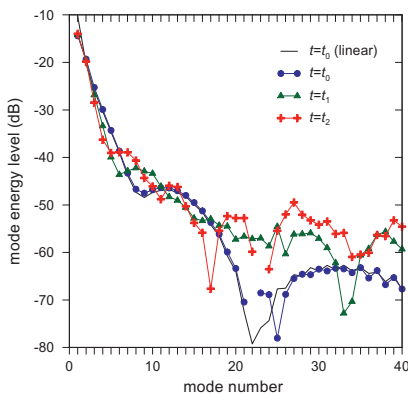


Fig. 5. Comparison of spectra envelopes computed for the same time moments as shown in Fig. 4. The solid line without marks shows the spectrum of the string with IS. The marked solid lines show the spectra of the string with NT.

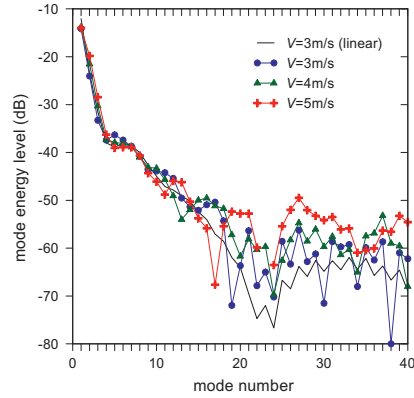


Fig. 6. Comparison of spectra envelopes computed for constant value of the capo bar curvature $R = 15$ mm, and varying the hammer striking velocity V . The solid line without marks shows the spectrum of the string with IS. The marked solid lines show the spectra of the string with NT.

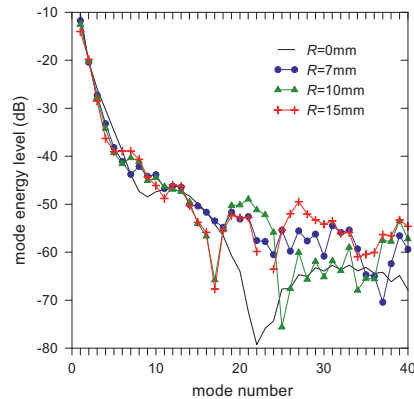


Fig. 7. Comparison of spectra envelopes computed for constant value of hammer striking velocity $V = 5$ m/s, and varying the radius of the capo bar curvature R . The solid line without marks shows the spectrum of the string with IS. The marked solid lines show the spectra of the string with NT.

4.2. Modeling of sawari mechanism in Chikuzen biwa

Presented approach of modeling capo bar–string interaction can be successfully applied to other instruments that also have the strings termination similar to the capo bar in the piano. Taguti in [1,2] has investigated the string vibration in lutes called *biwa* and *shamisen* which are equipped with *sawari*, whose physical structure is a little different but it induces essentially the same nonlinear effect in the string vibrations.

Here we consider the profile of the *sawari* surface approximated by function

$$Z(x) = \begin{cases} -\frac{1}{2R}x^2, & \text{if } x \leq s \\ -\infty, & \text{if } x > s \end{cases} \quad (18)$$

where s is the extent of the *sawari* along the string length (x -axis), R is the radius of a *sawari* curvature at a point $x = 0$. Values of

parameter s and R for *sawari* in *biwa* are taken $s = 1$ cm, $R = 2$ m. Similarly to capo bar the *sawari* surface is also considered to be absolutely rigid.

Biwa string vibration is described also by Eq. (1), i.e. we consider the *biwa* string as an ideal flexible. Parameters for the *biwa* string are taken from [10], and they are as follows: string length $L = 0.8$ m, linear mass density $\mu = 0.375$ g/m, string tension $T = 38.4$ N, and the speed of a wave traveling along the string $c = 320$ m/s. The main tone frequency of such a string $f = 200$ Hz.

The string plucking condition is chosen as follows: at a moment $t = 0$ the force

$$F(t) = F_0 \alpha t \exp(-\alpha t) \tag{19}$$

starts to act on the string at a point $x = 3/4L$ in a perpendicular direction. At a moment $t = t_*$ the force releases the string, i.e. $F(t) = 0$ if $t > t_*$. Here parameter $\alpha = 2 \text{ ms}^{-1}$, duration of the force action $t_* = 2.5$ ms, and $F_0 = 0.96$ N.

According to relation (3), the outgoing wave $g(t)$ created by this force is determined by continuous function

$$g(t) = \begin{cases} A\{1 - [1 + \alpha t] \exp(-\alpha t)\}, & \text{if } t < t_*, \\ \text{const} = g(t_*), & \text{if } t \geq t_*, \end{cases} \tag{20}$$

Here the coefficient $A = 2$ mm, and $g(t_*) = 1.92$ mm.

In Fig. 8 we show the results of simulation of the *biwa* string motion obtained by using the proposed NT string interaction model, and the form of g function, presented above. The solid line marked with circles shows the string form at a moment $t = t_0 = 2.1$ ms. At this moment the force defined by relation (19) is still acting on the string and will do so for the next 0.4 ms. The string has not touch the *sawari* surface yet (the period of strings vibration $T_0 = 5$ ms). The next string form is presented for a moment $t = t_1 = 16.4$ ms. Before that moment the string has interacted with the *sawari* by touching it for 3 times, and the corresponding form of the string is shown by solid line marked with triangles. At the moment $t = t_2 = 201.4$ ms the string has interacted with the *sawari* for 40 times, and the corresponding form of the string is marked by solid line with crosses. The dashed lines marked with

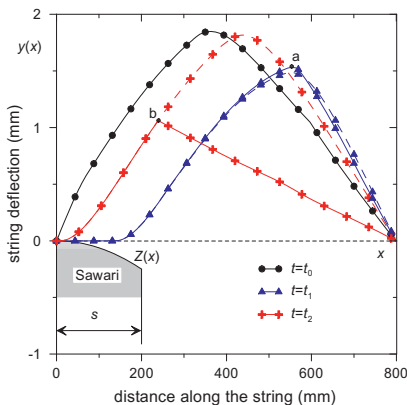


Fig. 8. Forms of *biwa* strings computed for different time moments $t = t_0 = 2.1$ ms (before first interaction), $t = t_1 = 16.4$ ms (after 3 interactions), $t = t_2 = 201.4$ ms (after 40 interactions). The solid lines show the string terminated on the *sawari* surface; the dashed lines show the string vibrating without *sawari*. The illustrative out-off proportion *sawari* configuration is shaded.

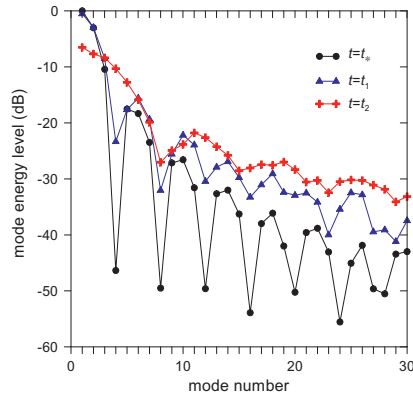


Fig. 9. Evolution of spectra over time ($t_* = 2.5$ ms, $t_1 = 16.4$ ms, $t_2 = 201.4$ ms).

triangles and crosses show the forms of the string vibrations in absence of *sawari* at all.

By studying Fig. 8, one can notice that with the passage of time the distinct sharp edge (discontinuity in slope) is appearing on the curve displaying the string deflection. At the moment $t = t_1 = 16.4$ ms the sharpening is barely visible (point marked by letter a), but with every new interaction of the string with the *sawari* it becomes more distinguishable. After 40 interactions ($t = t_2 = 201.4$ ms) the sharp edge is clearly visible (point marked by letter b), and entirely formed.

The example of the dynamic motion of *biwa* string is available for viewing at the supplementary web page of this article [22]. The computer animation shows in detail the formation, evolution, and sharpening of the *biwa* string form.

Effect of *sawari* on the spectral structure of the *biwa* string vibration is shown in Fig. 9.

The first spectra envelope is shown for the time moment $t = t_* = 2.5$ ms. At this moment the force defined by relation (19) has released the string, which means that the spectrum of the string with IS, according to (11)–(13) is a stationary spectrum. By observing the dynamic motion of the *biwa* string one can see that by the moment $t = t_*$ the string has not yet touched the *sawari* surface, which means that the spectra for the moment $t = t_*$ shown in Fig. 9 corresponds both for the string vibration with *sawari* and without it. Other two spectra are calculated for the time moments t_1, t_2 corresponding to the same string vibrations, which are shown in Fig. 8.

Analysis of spectral structure of *biwa* string vibrations shows that it undergoes a period of rapid change, which lasts approximately for 200 ms. After that time the spectra becomes stable. Fig. 9 shows clearly that during that time mean level of high modes grows up significantly and level of some low frequency modes decreases. This suggests that energy is being transferred from lower to higher partials.

Presented results and conclusions are in good agreement with experimental data obtained by Taguti [2]. Similarly to Taguti's conclusions we also can state that *sawari* effect on the produced tone (string vibration) can be observed in two aspects: the *sawari* intensifies higher partials and prolongs their duration.

5. Conclusions

The computing method presented in this paper was capable of reproducing nonlinear effects of the string vibrations caused by

the complex interaction between the string and the string support. The model is based on the traveling wave solution which makes the method numerically reliable and highly stable. The accuracy of the computing method is only determined by the values of the discrete temporal and spatial steps, which were chosen to obtain the suitable description of the initial local disturbance of the string's motion, and the resolution of the computational grid was selected to be fine enough to account for the relatively small extent of the bridge compared to the string's length. This meant that the model was capable of predicting the string's motion for extensive periods of time without becoming unstable.

The effect of the amplitude of the string vibrations on the mean level of high modes was clearly evident, and this was to confirm that the capo bar and the *sawari* are indeed the nonlinear string terminations. The influence of the curvature of rigid contact surface on the string vibrations and resulting changes in spectral structure over some period of time after string excitation was clearly demonstrated. The theoretical and experimental studies of the *sawari* mechanism's action on the string vibrations discussed by Taguti [1,2,10] has been verified. In addition it was shown that the ideal lossless string terminated at *sawari* or capo bar vibrates in two distinct vibration regimes. In the beginning the string starts to interact in a nonlinear fashion with the bridge, and the resulting string motion is aperiodic. After some time of aperiodic vibration, the string vibration settles in a periodic regime, where the dynamic motion of the string is repetitious in time.

Presently, current model describing the motion of the string with nonlinear support is still idealized and far from complete. Among other things, we use a very simple boundary condition for the string at the bridge. Further, we will attempt to include more realistic loading of the string terminated at the bridge.

Concerning the influence of the capo bar curvature on the piano string vibration one can state that effect appears stronger for hard hammer blows and for the last treble strings where the position of the striking point is close enough to the apex of a V-shaped section of the capo bar. Our theoretical model was confirmed also by exploration of some pianos, which had a harsh voicing in treble. Visual inspection of the capo bar of these instruments revealed that the surface of the edge of the cast iron frame was damaged and had defects. It meant that at such points the curvature of the surface was extremely large, therefore nonlinear effects arose. After the treatment of the damaged surface the sounding of the treble notes was significantly improved. For this reason manufacturers of grand pianos should produce each cast iron frame very accurately, and carefully process the surface of the edge.

Acknowledgment

This research was supported by the EU through the European Regional Development Fund, and by the Estonian Ministry of Education and Research (SF 0140077s08).

References

- [1] Taguti T, Tohnai YK. Acoustical analysis on the sawari tone of chikuzen biwa. *Acoust Sci Technol* 2001;22:199–207.
- [2] Taguti T. Sound production of sawari mechanism in biwa. In: Proc 18th int congr on acoustics, Kyoto, Japan; 2004. p. 2119–22.
- [3] Raman CV. On some Indian stringed instruments. In: Proceedings of the Indian association for the cultivation of science, vol. 7; 1922. p. 29–33.
- [4] Hall DE. Piano string excitation IV: the question of missing modes. *J Acoust Soc Am* 1987;82(6):1913–8.
- [5] Schatzman M. A hyperbolic problem of second order with unilateral constraints: the vibrating string with a concave obstacle. *J Math Anal Appl* 1980;73:138–91.
- [6] Burrige R, Kappraff J, Morshedi C. The sitar string, a vibrating string with a one-sided inelastic constraint. *SIAM J Appl Math* 1982;42:1231–51.
- [7] Cabannes H. Presentation of software for movies of vibrating strings with obstacles. *Appl Math Lett* 1997;10(5):79–84.
- [8] Krishnaswamy A, Smith JO. Methods for simulating string collisions with rigid spatial obstacles. In: IEEE workshop on applications to signal processing to audio and acoustics; 2003. p. 233–6.
- [9] Han SM, Grosenbaugh MA. Non-linear free vibration of a cable against a straight obstacle. *J Sound Vib* 2004;273:337–61. 2004.
- [10] Taguti T. Dynamics of simple string subject to unilateral constraint: a model analysis of sawari mechanism. *Acoust Sci Technol* 2008;29:203–14. 2008.
- [11] Vyasrayani CP, Birkett S, McPhee J. Modeling the dynamics of a vibrating string with a finite distributed unilateral constraint: application to the sitar. *J Acoust Soc Am* 2009;125(6):3673–82.
- [12] Rank E, Kubin G. A waveguide model for slab bass synthesis. In: Proc IEEE int conf on acoustics, speech, and signal processing, vol. 1; 1997. p. 443–6.
- [13] Evangelista G, Eckerholm F. Player-instrument interaction models for digital waveguide synthesis of guitar: touch and collisions. *IEEE Trans Audio Speech Language Process* 2010;18(4):822–32.
- [14] Siddiq S. A physical model of the nonlinear sitar string. *Arch Acoust* 2012;37(1):73–9.
- [15] Conklin Jr HA. Design and tone in the mechanoacoustic piano. Part II. Piano structure. *J Acoust Soc Am* 1996;100(2):695–708. Pt. 1.
- [16] Stulov A, Kartofelev D. Vibration of the string with nonlinear contact condition. In: AIP conf proc 1022: 18th international symposium on nonlinear acoustics ISNA 18, Stockholm, Sweden; 2008. p. 621–4.
- [17] Hall DE. Piano string excitation VI: nonlinear modeling. *J Acoust Soc Am* 1992;92(1):95–105.
- [18] Stulov A. Physical modeling of the piano string scale. *Appl Acoust* 2008;69(11):977–84.
- [19] Stulov A. Hysteretic model of the grand piano hammer felt. *J Acoust Soc Am* 1995;122(3):2577–85.
- [20] Stulov A. Dynamic behavior and mechanical features of wool felt. *ACTA Mech* 2004;169(1–4):13–21.
- [21] Stulov A. Experimental and computational studies of piano hammers. *ACTA Acust United Acust* 2005;91(6):1086–97.
- [22] Supplementary web page of the article <<http://www.cs.ioc.ee/dima/stringmovies.html>>.

Publication II

D. Kartofelev, A. Stulov, H.-M. Lehtonen, and V. Välimäki,
“Modeling a vibrating string terminated against a bridge with arbitrary geometry,” in *Proceedings of SMAC 2013, 4th Stockholm music acoustics conference*, (R. Bresin and A. Askenfelt, eds.), (Stockholm, Sweden), pp. 626–632, KTH Royal Institute of Technology, 2013.

MODELING A VIBRATING STRING TERMINATED AGAINST A BRIDGE WITH ARBITRARY GEOMETRY

Dmitri Kartofelev, Anatoli Stulov

Institute of Cybernetics at
Tallinn University of Technology,
Tallinn, Estonia
dima@cs.ioc.ee

Heidi-Maria Lehtonen, Vesa Välimäki

Department of Signal Processing and
Acoustics, Aalto University,
Espoo, Finland
heidi-maria.lehtonen@aalto.fi

ABSTRACT

This paper considers dynamic string motion in which the displacement is unilaterally constrained by the termination condition with an arbitrarily chosen geometry. A digital waveguide model is proposed for simulating the nonlinearity inducing interactions between the vibrating string and the contact condition at the point of string termination. The current work analyzes the resulting string motion influenced by the contact conditions with mostly flat but slightly curved geometries. The effect of a minute imperfection of the termination condition on the string vibration is investigated. It is shown that the lossless string vibrates in two distinct vibration regimes. In the beginning the string starts to interact in a nonlinear fashion with the bridge, and the resulting string motion is nonperiodic. The duration of that vibration regime depends on the geometry of the bridge. After some time of nonperiodic vibration, the string vibration settles in a periodic regime. Presented results are applicable for example in the physics-based sound synthesis of stringed musical instruments, such as the shamisen, biwa, sitar, tambura, veena or even the bray harp and the grand piano.

1. INTRODUCTION

In numerous musical instruments the collision of a vibrating string with rigid spatial obstacles, such as frets or a curved bridge, are crucial to the tonal quality of the produced sounds. Lutes such as the shamisen, biwa, sitar, tambura or veena have a very distinctive sound which can be described as *buzzing*. The form of the bridge used in these instruments is quite different from that usually found in most stringed instruments, since the profiles of the bridges are slightly curved, almost flat (see Fig. 1). The spatial extent of the bridges along the direction of the string is relatively large compared to the speaking length of the strings themselves [1].

A similar mechanism is also not unknown in Western instruments. The treble strings of a grand piano usually terminate at the capo bar (*capo d'astro*). The V-shaped sec-

tion of the capo bar has a parabolic curvature, and although the area to which the string rapidly touches while vibrating is small compared to the string's speaking length, it was shown by Stulov and Kartofelev [2] that the capo bar has a noticeable effect on the piano tone formation.

Also the Medieval and Renaissance bray harp has small bray-pins which provide a metal surface for the vibrating string to impact, increasing the upper partial content in the tone and providing a means for the harp to be audible in larger spaces and in ensemble with other instruments [3]. It is evident that for realistic physically informed modeling of these instruments such nonlinearity inducing interactions need to be examined and simulated accurately.

Raman was the first to study the effect and identify the bridge as the main reason for distinctive sounding of the tambura and veena [4]. Over the years many authors have solved this problem using different approaches [3], [5] – [15]. An overview and comparison of the existing methods that are proposed for modeling the interaction between the termination and the string are presented by Vyasarayani, *et al.* in [3].

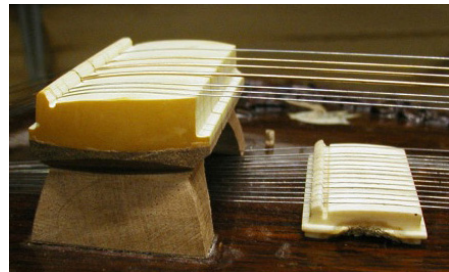


Figure 1. *Jawari*, the main bridge of the sitar and *taraf ka ghoraj*, the sympathetic string bridge.

The aim of the current paper is to model the vibration of the string which is unilaterally constrained at one of the points of string termination. Dynamic motion of the plucked ideal string against the termination condition (TC) with three different profile geometries are simulated and obtained results are examined. In addition, a method for quantifying the effect of minute geometric imperfections of the mostly flat bridge on the string vibration is provided.

Although the cases examined here are for bridges with mostly flat profile geometries, the obtained conclusions hold

to some degree for cases where the bridge profile geometries are more versatile, cf. [2].

Compared to the previously published work, we propose a new and relatively simple approach for modeling the non-linear bridge-string interaction and consequently the dynamic motion of the entire string. In this work the proposed model is demonstrated using physical parameters that are obtained from a Chinese lute biwa, thus presenting an applied approach.

2. IDEAL STRING

For analyzing the phenomenon of interest, it is sufficient to describe the dynamic motion of the string using the *ideal* string. Phenomena such as losses or dispersion are discarded. We consider the wave equation for the linear and lossless flexible string:

$$\frac{\partial^2 u}{\partial t^2} = c^2 \frac{\partial^2 u}{\partial x^2} \quad (1)$$

with $u(0, t) = u(L, t) = 0$, where L and $u(x, t)$ are the speaking length and the displacement of the string, respectively. In (1) the value $c = \sqrt{T/\mu}$ is the speed of the traveling waves on the string, where T is the tension and μ is the linear mass density of the string [16].

String parameters for all the calculations in the current paper are the same as used by Taguti in [8]. Taguti investigated a biwa string with the following parameters: string length $L = 0.8$ m; linear mass density $\mu = 0.375$ g/m; string tension $T = 38.4$ N. From here it follows that the speed of the traveling waves along the string is $c = 320$ m/s and the fundamental frequency of such a string is $f_0 = 200$ Hz.

3. STRING EXCITATION

The string plucking condition can be introduced as follows. We assume that at the point $x = l = 3/4L$ the emerging traveling wave is of the form

$$u(l, t) = \begin{cases} A \left(\frac{t}{t_0}\right)^2 e^{2(1-t/t_0)}, & \text{if } 0 \leq t \leq t_0, \\ A, & \text{if } t > t_0. \end{cases} \quad (2)$$

In (2) $A = 1$ cm is the amplitude of the outgoing traveling wave and the duration of the excitation is $t = t_0 = 4$ ms. Selection of the plucking condition (2) ensures that the plucking force acting on the string point $x = l$ ceases if $t \geq t_0$ (time derivative of (2) is proportional to the plucking force) [2].

It can be shown that (1) may be satisfied by superposition of nondispersive traveling waves $u_r(t - x/c)$ and $u_l(t + x/c)$ moving in either directions along the string emerging from the plucking point $x = l$. At this point $u_r(l, t) = u_l(l, t) = u(l, t)$. These two waves u_r and u_l are simply a translation of the plucking condition (2) from the point $x = l$ to other segments of the string [16].

In the case of ideal rigid string termination where no TC is present, the boundary value $u(0, t) = u(L, t) = 0$ is satisfied if the wave $u_r(t - x/c)$ propagating to the right at the

point $x = L$ creates the wave $u_l(t + x/c) = -u_r(t - x/c)$ moving to the left and the wave $u_l(t + x/c)$ propagating to the left at the point $x = 0$ creates the wave $u_r(t - x/c) = -u_l(t + x/c)$ moving to the right. This procedure can be interpreted as equivalent to the digital waveguide approach [17, 18, 19].

It follows that for the current model the string displacement $u(x, t)$ at any point x of the string and for all time instants t is simply the resulting sum of waveforms u_r and u_l moving in both directions

$$u(x, t) = u_r\left(t - \frac{x}{c}\right) + u_l\left(t + \frac{x}{c}\right). \quad (3)$$

The method for modeling the bridge-string interaction is explained in Sections 5 and 6.

4. BRIDGE GEOMETRY

Slightly curved bridges of the lutes mentioned in Section 1 are usually located at the far end of the neck. Similarly the geometric contact condition (TC) is located at the termination point of the string. Figure 2 shows the traveling waves u_r and u_l , string displacement $u(x, t)$, and the location of the rigid termination (bridge) relative to the string.

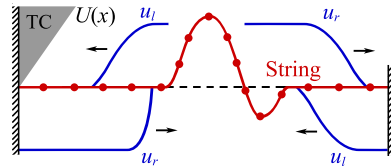


Figure 2. Scheme of the string displacement model. The traveling waves u_r and u_l (solid lines), and the forms of the string (solid lines marked by circles). Position of the TC relative to the string is shown using gray formation.

4.1 Case 1: Linear bridge with a sharp edge

The function $U(x)$ that describes the profile of a flat bridge is calculated as follows

$$U(x) = \begin{cases} kx, & \text{if } x \leq x_c, \\ \infty, & \text{if } x > x_c, \end{cases} \quad (4)$$

where $k = \tan \theta = 0.008$ is the slope of the linear function where $\theta \approx 0.008$ rad $\approx 0.46^\circ$. Value $x_c = 15$ mm marks the coordinate of the truncation of the linear function.

4.2 Case 2: Linear bridge with a curved edge

The profile of a bridge with a curved edge is calculated as follows

$$U(x) = \begin{cases} kx, & \text{if } x \leq x_b, \\ \frac{1}{2R}(x - x_b)^2, & \text{if } x > x_b, \end{cases} \quad (5)$$

where the parameter k has the same value and meaning as in the previous case. Parameter $R = 10$ mm is the curvature radius of the corresponding parabolic function

$f(x) = (2R)^{-1}x^2$ at its minimum. Coordinate $x_b = 10$ mm marks the transition between linear and parabolic parts of the geometry.

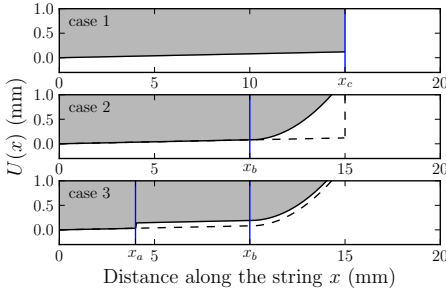


Figure 3. Termination condition geometry for the cases under study. Solid vertical lines mark the positions of the characteristic values x_a , x_b and x_c . Case 1: linear bridge with a sharp edge. Case 2: linear bridge with a curved edge, the dashed line shows the profile of the case 1 for comparison. Case 3: bridge with a small geometric imperfection, the dashed line shows the case 2 for comparison.

4.3 Case 3: Bridge with a geometric imperfection

The bridge in this case is similar to the previous case with the exception of an addition of small imperfection in the form of discontinuity in the linear part of the TC in (5). The bridge profile geometry for this case can be expressed in the following form

$$U(x) = \begin{cases} kx, & \text{if } x \leq x_a, \\ kx + y, & \text{if } x_a < x \leq x_b, \\ \frac{1}{2R}(x - x_b)^2 + K, & \text{if } x > x_b, \end{cases} \quad (6)$$

where the parameters k and R have the same value and meaning as in the previous cases. Parameter $y = 0.11$ mm raises the value of linear function in the interval $x = (x_a, x_b]$ where $x_a = 4$ mm and $x_b = 10$ mm. Constant $K = kx_b + y$ is presented in order to preserve continuity of the form in vicinity of the point $x = x_b$.

The TC geometries presented in (4) - (6) are shown in Fig. 3.

5. BRIDGE-STRING INTERACTION MODEL

In order to model the bridge-string interaction we assume that the reflecting wave $u_r(t - x/c)$ moving to the right appears only at the point $x = x^*$, where the amplitude of the string deflection $u(x^*, t) \geq U(x^*)$. The position of this point x^* is determined by the TC geometry $U(x)$ in the following way. Since the termination is rigid we must have $u(x^*, t) = U(x^*)$, and this condition results in the appearance (addition) of reflected wave

$$u_r\left(t - \frac{x^*}{c}\right) = U(x^*) - u_l\left(t + \frac{x^*}{c}\right), \quad (7)$$

where the waves u_l and u_r correspond to any waves that have reflected on earlier time moments and are currently located at $x = x^*$. The proposed method ensures that the amplitude of the string deflection, which is determined by (3), will never exceed the value $U(x)$.

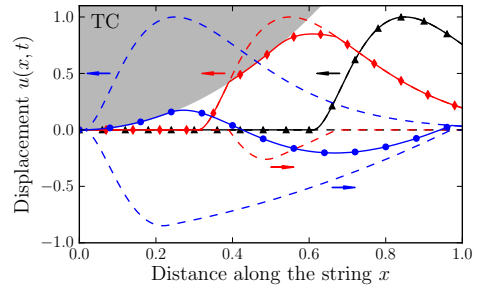


Figure 4. Reflection of the first wave from the termination. The traveling waves u_r and u_l (dashed lines), and the forms of the string (solid lines marked by signs) shown for consequent nondimensional moments of times $t_1 = 0.4$ (triangle); $t_2 = 0.7$ (diamond); $t_3 = 1.0$ (circle).

In Fig. 4 we demonstrate the form of the string in vicinity of the geometric termination during the reflection of the first wave $u_l(t + x/c)$ only. Using the procedure described above, the string deflection as a function of the nondimensional distance along the string is computed for three consequent normalized nondimensional ($c = 1$) moments of time. At the moment $t = t_1$ the form of the string (solid line marked by triangles) is determined only by the traveling wave u_l . At the next moment $t = t_2$ the small segment of the string is in contact with the surface of the termination, and the reflected wave $u_r(x, t_2)$ has appeared (dashed line). The corresponding form of the string deflection is shown by solid line marked with diamonds. At the moment $t = t_3$ the string is in contact with the surface of the termination on the segment closer to the string edge ($x = 0$). The form of the string at this moment is shown by solid line marked with circles, and the reflected wave $u_r(x, t_3)$ is also shown by the dashed line. Thus at some moments the string wraps or clings to the termination, and during that time the form of the string on some segment simply repeats the form of the termination.

6. NUMERICAL IMPLEMENTATION

The bridge-string interaction model and the ideal string vibration are implemented numerically by using discrete t - x space with the time mesh Δt and the space mesh Δx . Values for the Δt and Δx are selected so that

$$c \frac{\Delta t}{\Delta x} = 1, \quad (8)$$

where $c = \sqrt{T/\mu}$. Selection of the step-sizes Δx and Δt according to (8) ensures maximum accuracy of the result for any given resolution of the computational grid. Thus,

the transmission of the traveling waves u_r and u_l with respect to the points of the discrete t - x space are

$$u_r(x_n, t_m) = u_r(x_{n-1}, t_{m-1}), \quad (9)$$

$$u_l(x_n, t_m) = u_l(x_{n+1}, t_{m-1}), \quad (10)$$

where the index $n = 0, \dots, N$ corresponds to the discrete space points and the index $m = 0, \dots, M$ corresponds to the discrete time points. Values of the corresponding coordinates x and t in (9) and (10) can be calculated as $x = x_n = n\Delta x$ and $t = t_m = m\Delta t$, respectively.

In order to satisfy the boundary condition at the right side of the string, namely $u(L, t) = 0$, the mechanism presented in Sec. 3 is used. For every successive time moment t_m

$$u_l(x_N, t_m) = -u_r(x_N, t_{m-1}), \quad (11)$$

where $x_N = N\Delta x = L$.

The effect of the geometric TC on the string vibration can be implemented numerically as follows. According to Sec. 5 the traveling wave u_r only appears in the vicinity of the bridge at the discrete point $x_n = x_n^*$ where the amplitude of the string deflection $u(x_n^*, t) \geq U(x_n^*)$. Thus, for every successive time moment t_m and for all x_n^*

$$u_r(x_n^*, t_m) = u_r(x_n^*, t_{m-1}) - \Delta u, \quad (12)$$

where $\Delta u = u(x_n^*, t_m) - U(x_n^*)$. Expression of the form (12) is more suitable for the iterative numerical scheme used to generate the result compared to the expression (7) shown in Sec. 5. Finally, when the aforementioned operations are conducted the final form of the string's displacement with respect to the discrete computational grid takes the form

$$u(x_n, t_m) = u_r(x_n, t_m) + u_l(x_n, t_m). \quad (13)$$

Numerical parameters selected to calculate the presented results are: $\Delta x = 0.985$ mm, $\Delta t = 3.077$ μ s, number of spatial points $N = 816$, including spatial points dedicated for the bridge $N_{TC} = 25$, number of the time points $M = 130000$, from here it follows that the temporal sampling rate is 325 kHz. The relevant part of the computer code written using the Python programming language is available for examination at the supplementary web page of this article [20].

7. RESULTS AND DISCUSSION

Figure 5 shows the time series of the string deflection $u(l, t)$ computed at the plucking point $x = l$. Visual inspection of the string deflection $u(l, t)$ reveals that for all the presented cases the strings vibrate in two distinct regimes. The strong influence of the bridge on the string's motion is noticeable for a certain period of time, and its duration depends on the bridge geometry. During this time prolonging for $t = t_{np}$ the string vibrates in *nonperiodic regime*. One can clearly see that after the moment $t = t_{np}$ the behavior of the deflection $u(l, t)$ becomes seemingly highly periodic. Closer examination reveals that the string's displacement is actually still slightly changing and therefore is not absolutely

periodic (string continues to interact with the bridge) but the change is small and can be neglected. This regime is called here the *periodic vibration regime*. It must be noted that this almost periodic vibration regime is possible only when the bridge profile is mostly flat and the string is considered ideal and lossless.

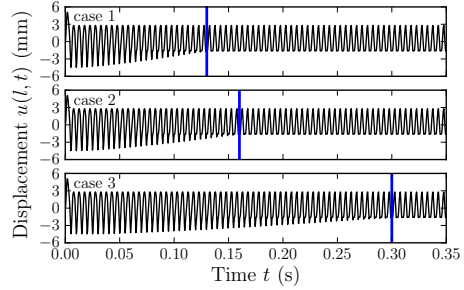


Figure 5. Time series of the string deflection $u(l, t)$ for the cases 1, 2, and 3. Nonperiodic and periodic vibration regimes are separated by vertical lines corresponding to the time moment $t = t_{np}$.

Table 1 shows the corresponding durations of the nonperiodic vibration regimes t_{np} for the cases under study. In addition, the corresponding number of string deflection $u(l, t)$ periods P_{np} are shown.

	t_{np} (s)	P_{np}
Case 1	0.13	26
Case 2	0.16	32
Case 3	0.30	60

Table 1. The duration and the number of the string deflection periods of the nonperiodic vibration regime.

The transitions between the nonperiodic and periodic regimes presented in Fig. 5 are also visible in the spectrograms presented in Fig. 6. All spectrograms are calculated using the Hanning window of the size 45 ms and the overlap value 55% of the window size. The animations of the simulated string vibration terminated against the bridges with profile geometries described in (4) – (6), are available for download on the supplementary web page of the current article [20].

7.1 Case 1: Linear bridge with a sharp edge

Spectrogram of the signal related to the case 1 is shown in Fig. 6 a. Dashed vertical line corresponds to the duration of the nonperiodic vibration regime t_{np} of the string. It can be seen that during the nonperiodic vibration regime the energy of the lower vibration modes is being transferred to the higher modes. This effect of spectral widening can be noticed when comparing Figs. 6 a and 7. Figure 7 shows the spectrogram of the corresponding linear case where no amplitude limiting TC is applied. Transfer of the energy

from lower to higher vibration modes is a sign of nonlinear behavior resulting from the interaction of the vibrating string and the bridge. This phenomenon is similar to the slapped bass effect [6] and the nonlinear limitation of the string amplitude by the damper in the part-pedaling effect in the grand piano [21, 22]. In the periodic vibration regime ($t > t_{np}$) the spectrum remains constant which is an expected result (cf. Fig. 5).

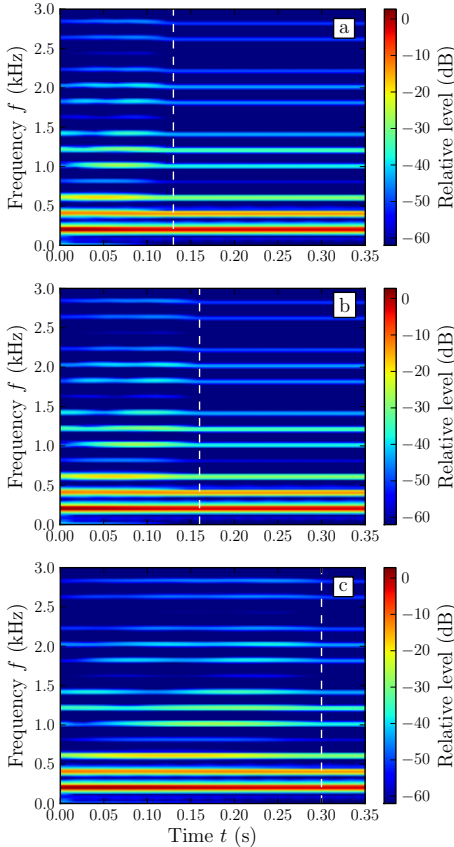


Figure 6. Spectrogram of the signal $u(l, t)$ for the cases: a) case 1, b) case 2 and c) case 3. The transition between nonperiodic and periodic vibration regimes at $t = t_{np}$ is shown using dashed line.

7.2 Case 2: Linear bridge with a curved edge

The spectrogram corresponding to the case 2 is shown in Fig. 6b. As can be seen the result in this case is similar to the case 1 with the exception of the 30 ms longer nonperiodic vibration regime.

7.3 Case 3: Bridge with a geometric imperfection

Figure 6c shows the spectrogram for the case 3. Now the nonperiodic vibration regime is 300 ms long, which is al-

most two times longer compared to the case 2. Again, the energy transfer from lower to higher modes is visible during the nonperiodic vibration regime.

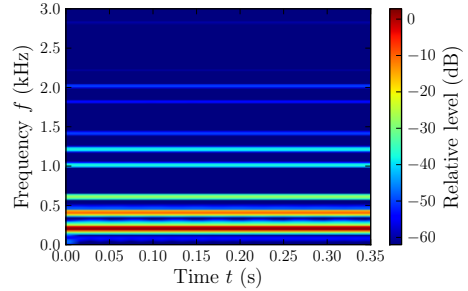


Figure 7. Spectrogram of the signal $u(l, t)$ for the linear case (no TC).

Relatively long nonperiodic vibration regime in connection with the properties of nonlinear dynamic systems can make playing such an instrument challenging. The timbre of the instrument can be very strongly influenced by the selection of the plucking point and the plucking manner, which results in uneven timbre behaviour. This effect is present for example in the sitar, and it makes the learning to play the sitar more complicated compared to the similar Western instruments.

Figure 8 shows four periods of the string deflection $u(l, t)$ during the periodic vibration regime, where the interaction of the string with the bridge is minimal. Figure 8 presents a comparison of all nonlinear cases 1 – 3 to the corresponding linear case. Nonlinear cases are rendered almost identical for $t > t_{np}$. This result is explained by the fact that the selected contact condition profiles defined by (4) - (6) have linear sections near to the string termination point ($x = 0$). With the progression of time this linear section of the bridge *trims* the effects of the other (non-linear) sections of the geometry, thus eventually rendering the periodic string vibrations for all nonlinear cases almost identical.

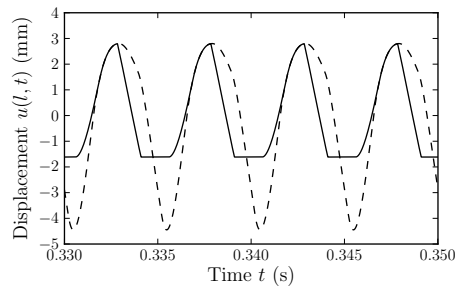


Figure 8. Four periods of the string displacement $u(l, t)$ for the nonlinear cases 1, 2 and 3 are shown using solid line (all identical). Corresponding linear case (no TC) is shown using dashed line.

In addition to the aforementioned results it was noted that a small glide and shift of the fundamental frequency f_0 (and consequently the frequencies of all the other modes, because $f_i = i f_0$ where i is the mode number) of the otherwise harmonic vibration is present. This effect appears for all presented cases and only during the nonperiodic vibration regime after which the frequency slides back to normal (i.e. $f_0 = 200$ Hz). Emergence of this effect is explained by the effective shortening of the speaking length of the string due to the spatial extent of the bridge and the interaction of the string with the bridge.

7.4 String vibration spectrum in the periodic vibration regime

After the period of nonperiodic vibration regime has passed, the string enters the periodic vibration regime. The spectrum of the string vibrations for any time instant of interest is computed using Fourier analysis. If

$$u(x, t) = \sum_i (A_i \cos \omega_i t + B_i \sin \omega_i t) \sin\left(\frac{i\pi x}{L}\right), \quad (14)$$

with normal-mode angular frequencies $\omega_i = i\omega_0$, where $\omega_0 = 2\pi f_0$ and i is the mode number, then

$$A_i = \frac{2}{L} \int_0^L u(x, t) \sin\left(\frac{i\pi x}{L}\right) dx, \quad (15)$$

$$B_i = \frac{2}{L\omega_i} \int_0^L v(x, t) \sin\left(\frac{i\pi x}{L}\right) dx, \quad (16)$$

where $v(x, t)$ is the velocity of the string. It follows that the string mode energy E_i of the i th mode is defined by

$$E_i = \frac{M\omega_i^2}{4} (A_i^2 + B_i^2), \quad (17)$$

where $M = \mu L$ is the total mass of the string. And the mode energy level is defined as

$$EL_i = 10 \log_{10} \left(\frac{E_i}{E_0} \right). \quad (18)$$

Fourier analysis using (18) shows that the spectra of cases 1, 2 and 3 are almost identical for $t > t_{np}$ (cf. Fig. 8). As mentioned earlier this result is explained by the fact that the selected contact condition profiles defined by (4) - (6) have linear sections near to the string termination point ($x = 0$). Figure 9 shows the comparison of the spectrum of the linear case (no TC) with those of the nonlinear cases 1, 2 and 3. The spectrum of the linear case is shown for the time interval $t = (t_0, \infty)$ and the nonlinear cases are shown for the time interval $t = (t_{np}, \infty)$.

Results from spectrogram analysis shown in Fig. 6 are confirmed here by calculations made using (18) and the resulting spectrum is shown in Fig. 9.

Widening of the spectra compared to the linear case and the transfer of energy from lower to higher vibration modes is visible. Relative level of some higher modes grow up to 25 dB. This means that resulting tone of the musical instrument that is equipped with the rigid, slightly curved bridge

which influences the string vibration is completely different from that of an instrument having a regular bridge.

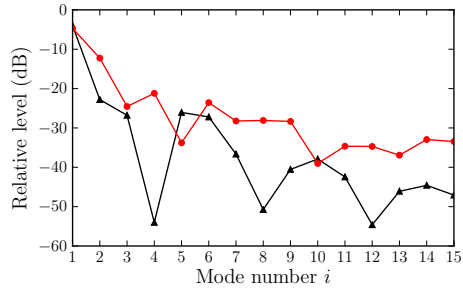


Figure 9. Stationary spectrum of the string vibrations for $t > t_{np}$. Spectra corresponding to the nonlinear cases 1, 2 and 3 are shown using circles (all identical). Linear case (no TC) is shown using triangles.

8. CONCLUSIONS

This article introduced a model that simulates the vibration of an ideal string terminated against a bridge with an arbitrary geometry. Additionally, a method for modeling the effect of minute geometric imperfections of the bridge geometry on the string vibration was presented. It was shown that the lossless string vibrates in two distinct vibration regimes. In the beginning the string starts to interact in a nonlinear fashion with the bridge, and the resulting string motion is nonperiodic. After some time of nonperiodic vibration, the string vibration settles in a *almost* periodic regime, where the dynamic motion of the string is repetitious in time.

The duration of the nonperiodic vibration regime depends on the geometry of the termination. It was concluded that minor imperfection of the bridge profile geometry elongate the duration of the nonperiodic vibration regime and produce noticeable changes in the evolution of the timber in the nonperiodic regime of vibration. The resulting spectrum in the periodic regime is identical for all nonlinear cases studied. Comparison of the resulting spectra in the periodic vibration regime of the linear and nonlinear cases showed that the interaction of the string with the rigid bridge widens the spectrum by transferring energy from lower to higher vibration modes.

Acknowledgments

This work was conducted in February - April 2013, when Dmitri Kartofelev was visiting Aalto University. His visit was supported by the Kristijan Jaak Scholarship program from the Archimedes Foundation, Estonia.

This research was partly supported by the European Union through the European Regional Development Fund and by the Estonian Ministry of Education and Research (SF 0140 077s08).

The work of Heidi-Maria Lehtonen was supported by the Finnish Cultural Foundation.

The authors are grateful for the useful comments and suggestions from Dr. Balázs Bank.

9. REFERENCES

- [1] Wikipedia the free encyclopedia: "Plucked string instrument," http://en.wikipedia.org/wiki/Plucked_string_instrument, 2013
- [2] A. Stulov and D. Kartofelev, "Vibration of strings with nonlinear supports," in press, *Applied Acoustics*, 2013.
- [3] C. P. Vyasarayani, S. Birkett and J. McPhee, "Modeling the dynamics of a vibrating string with a finite distributed unilateral constraint: Application to the sitar," *J. Acoust. Soc. Am.*, vol. 125, no. 6, pp. 3673–3682, 2009.
- [4] C. V. Raman, "On some Indian stringed instruments," in *Proc. Indian Assoc. Cultiv. Sci.* vol. 7, pp. 29–33, 1921.
- [5] A. Krishnaswamy and J. O. Smith, "Methods for simulating string collisions with rigid spatial obstacles," in *Proc. IEEE Workshop on Applications of Signal Processing to Audio and Acoustics*, October 19-22 New Paltz, NY, USA, pp. 233–236, 2003.
- [6] E. Rank and G. Kubin, "A waveguide model for slap-bass synthesis," in *Proc. IEEE International Conference on Acoustics, Speech, and Signal Processing*, April 21-24, Munich, Germany, pp. 443–446, 1997.
- [7] T. Taguti, "Numerical simulation of vibrating string subject to sawari mechanism," in *Proc. 19th Int. Congr. on Acoustics*, September 2-7, Madrid, Spain, pp. 1–6, 2007.
- [8] T. Taguti, "Dynamics of simple string subject to unilateral constraint: A model analysis of sawari mechanism," *Acoustical Science and Technology*, vol. 29, pp. 203–214, 2008.
- [9] R. E. L. Turner and P. Villaggio, "A note on the motion of a string on a unilaterally reacting foundation," *SIAM Journal on Applied Mathematics*, vol. 49, no. 4, pp. 1223–1230, 1989.
- [10] S. Siddiq, "A physical model of the nonlinear sitar string," *Archives of Acoustics*, vol. 37, no. 1, pp. 73–79, 2012.
- [11] R. Burrige, J. Kappraff and C. Morshedi, "The sitar string, a vibrating string with a one-sided inelastic constraint," *SIAM Journal on Applied Mathematics*, vol. 42, no. 6, pp. 1231–1251, 1982.
- [12] S. M. Han and M. A. Grosenbaugh, "Non-linear free vibration of a cable against a straight obstacle," *Journal of Sound and Vibration*, vol. 273, pp. 337–361, 2004.
- [13] H. Cabannes, "Presentation of software for movies of vibrating strings with obstacles," *Appl. Math. Lett.*, vol. 10, no. 5, pp. 79–84, 1997.
- [14] C. Valette, "The mechanics of vibrating strings," in *Mechanics of Musical Instruments*, edited by J. Kergomard and G. Weinreich, Springer-Verlag, Vienna, pp. 115–183, 1995.
- [15] G. Evangelista and F. Eckerholm, "Player–instrument interaction models for digital waveguide synthesis of guitar: touch and collisions," *IEEE Transactions on audio, speech, and language processing*, vol. 18, no. 4, pp. 822–832, 2010.
- [16] N. H. Fletcher and T. D. Rossing, *The physics of musical instruments*, Springer, 1998.
- [17] J. O. Smith, "Physical Modeling using Digital Waveguides," *Computer Music Journal*, vol. 16, no. 4, pp. 74–91, 1992.
- [18] V. Välimäki, J. Pakarinen, C. Erkut, and M. Karjalainen, "Discrete-time modelling of musical instruments," *Reports on Progress in Physics*, vol. 69, no. 1, pp. 1–78, 2006.
- [19] J. O. Smith, *Physical audio signal processing for virtual musical instruments and audio effects*, <https://ccrma.stanford.edu/~jos/pasp/>, W3K Publishing, 2010.
- [20] Supplementary web page of the current article: "Animations of the string vibration terminated against a bridges with arbitrary geometry's: Cases 1 – 3," <http://www.cs.ioc.ee/~dima/stringarbitrary.html>
- [21] H.-M. Lehtonen, A. Askenfelt and V. Välimäki, "Analysis of the part-pedaling effect in the piano," *J. Acoust. Soc. Am.* vol. 126, no. 2, pp. EL49–EL54, 2009.
- [22] A. Stulov, V. Välimäki and H.-M. Lehtonen, "Modeling of the part-pedaling effect in the piano," in: *Acoustics 2012*, April 23-27, Nantes, France, pp. 1223–1228, 2012.

Publication III

D. Kartofelev and A. Stulov,
“Propagation of deformation waves in wool felt,”
Acta Mechanica, Online first, pp. [1–11], 2014.
DOI: 10.1007/s00707-014-1109-1

Dmitri Kartofelev · Anatoli Stulov

Propagation of deformation waves in wool felt

Received: 12 November 2013 / Revised: 3 February 2014
© Springer-Verlag Wien 2014

Abstract The natural wool felt is becoming increasingly popular and important as a resource material in various applications. In this study, a constitutive equation that describes the deformation wave propagation in the felt material is derived using a hysteretic piano hammer model. A nonlinear partial differential equation with third-order terms that takes into account the elastic and hereditary properties of a microstructured felt is used to study a pulse propagation in the one-dimensional case. The boundary value problem is considered, and the numerical solution describing the strain wave propagation is provided. It is shown that the speed of a deformation wave increases with the growth of its amplitude. Also, the nonlinearity makes the front slope of a pulse steeper, which causes the eventual breaking of a pulse. The solution of the linear problem is analyzed, and the rate of the wave attenuation in the felt material is estimated.

1 Introduction

The felt is likely to be the oldest textile fabric known to man. It is made using wool or other animal fibers by tightly matting them together. Nowadays, wool felt with its unique cellular structure is being used for a wide variety of applications: vibration isolation, sound absorption, noise reduction, filtering, etc. For almost two centuries, the felt has been widely used in the piano manufacturing. For instance, felt pads are used for vibration isolation between vibrating strings and the cast iron frame. Piano dampers are made using wool felt, and of course, the piano hammers are coated with two or several layers of felt.

The first constitutive framework proposed as a mathematical model of the hammer felt was worked out by Ghosh [1], who considered the force–compression characteristic of the felt obeying the power law

$$F = Au^{\hat{p}}, \quad A = \text{const}, \quad (1)$$

where F is the acting force, and u is the felt compression. Experimental static testing of different hammers by Hall and Askenfelt [2] demonstrated that for voiced piano hammers, the values of parameter \hat{p} ranging from 2.2 to 3.5 give a good approximation of dependence (1). According to Hertz's law, the force acting on two Hookean bodies gives $\hat{p} = 3/2$. The values of \hat{p} different from $3/2$ indicate the non-Hookean felt properties.

D. Kartofelev (✉) · A. Stulov
Institute of Cybernetics, Tallinn University of Technology, Akadeemia 21, 12618 Tallinn, Estonia
E-mail: dima@cs.ioc.ee
Tel.: +372-55668475
Fax: +372-6204151

A. Stulov
E-mail: stulov@ioc.ee
Tel.: +372-5187079
Fax: +372-6204151

Published online: 21 March 2014

More in-depth information about properties of the hammer felt was presented by Yanagisawa et al. [3] and by Yanagisawa and Nakamura [4,5]. Their dynamic experiments demonstrated very important properties of the felt: The nonlinear force–compression characteristic, strong dependence of the slope of the loading curve on the rate of loading, and the significant influence of hysteresis, i.e., the loading and unloading of the felt, are not alike. The existence of these phenomena requires that the felt is understood as a microstructured material possessing history-dependent properties, or in other words, is a material with memory.

The aim of the current paper was to derive and present a mathematical model that describes the deformation wave propagation in the felt material using the hysteretic piano hammer model. The problem is studied for the one-dimensional case. The presented model takes into account the elastic and hereditary properties of the microstructured wool felt.

2 Compression properties of piano hammer felt

The first dynamical model of the piano hammer felt, which takes into consideration both the hysteresis of the force–compression characteristics and their dependence on the rate of felt loading, was presented in [6]. Following Rabotnov [7], this new nonlinear hysteretic model of the felt was proposed by replacing the parameter \mathcal{A} in expression (1) with a time-dependent operator $F_0[1 - \mathcal{R}(t)*]$, where $*$ denotes the convolution operation, and the relaxation function was given by

$$\mathcal{R}(t) = \frac{\gamma}{\tau_0} e^{-t/\tau_0}. \quad (2)$$

Thus, instead of the simple relation (1), the four-parameter hysteretic model of the felt was derived in [6] in the form

$$F(u(t)) = F_0 \left[u^{\hat{p}}(t) - \frac{\gamma}{\tau_0} \int_0^t u^{\hat{p}}(\xi) e^{(\xi-t)/\tau_0} d\xi \right]. \quad (3)$$

Here, the instantaneous stiffness F_0 and the nonlinearity exponent \hat{p} are the elastic parameters of the material, and hereditary amplitude γ and relaxation time τ_0 are the hereditary parameters. The history of the felt deformation is assumed to start at $t = 0$.

An experimental investigation of the compression characteristics of the piano hammer felt was carried out using a special piano hammer testing device [8,9]. The device was designed for measuring the force and compression histories during a hammer strike against a rigid surface. The aim of these experiments was a verification of the hysteretic model in the form (3), and the determination of the hammer felt parameters.

Figure 1 displays the compression characteristics obtained experimentally. Force–compression curves are presented for three different rates of loading by combining the force and compression histories presented in [9].

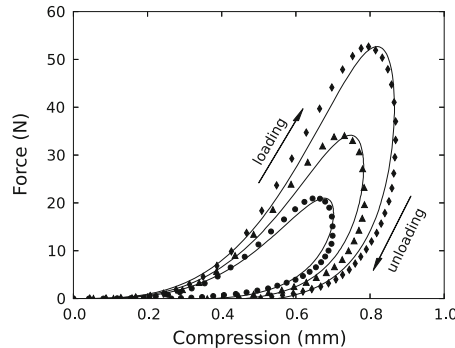


Fig. 1 Comparison of measured data and numerical simulations of force–compression characteristics of the piano hammer. The arrows show the directions of the compression and decompression branches. The symbols denote measured data for hammer striking velocities: 1.31 m/s (diamonds) (contact time $t_c = 1.7$ ms); 1.00 m/s (triangles) ($t_c = 2.0$ ms); 0.74 m/s (bullets) ($t_c = 2.5$ ms). The solid lines are the corresponding curves obtained numerically

The arrows indicate the direction of compression and decompression processes. The solid lines represent the numerical simulation of the experiment, using the four-parameter hysteretic model of the felt in the form (3).

The experimental results presented in Fig. 1 are typical for all measured hammers. A significant influence of hysteresis can be seen clearly in the hammer felt characteristics. The hysteresis leads to the behavior where the loading and unloading of the felt do not follow the same path. This indicates that the energy is dissipating due to viscous damping or frictional losses caused by fiber slippage effects. Moreover, the slope of the force–compression characteristics increases with the growth of the rate of impact, and the contact time is decreased by a stronger strike, exactly like the model of the hysteretic hammer predicts. Thus, we may state that the constitutive four-parameter hysteretic model of the felt describes the dynamic features of piano hammers fairly well and is consistent with the results from experiments presented in [3–5].

The continuous variations in the hammer felt parameters versus key number N were obtained in [9] by numerical simulation of the experimental data for a whole piano hammer set. A best match to the whole set of hammers was approximated using

$$\hat{p} = 3.7 + 0.015 N, \quad 3.72 \leq \hat{p} \leq 4.98, \quad (4)$$

$$\gamma = 0.9894 + 0.000088 N, \quad 0.9895 \leq \gamma \leq 0.9972, \quad (5)$$

$$\tau_0 = 2.72 - 0.02 N + 0.00009 N^2, \quad 1.65 \leq \tau_0 \leq 2.70, \quad (6)$$

$$F_0 = 15,500 e^{0.059 N}, \quad 16,440 \leq F_0 \leq 2,787,300 \quad (7)$$

for hammer number $1 \leq N \leq 88$. Here, the unit for relaxation time τ_0 is μs , and the unit for the instantaneous stiffness F_0 is $\text{N/mm}^{\hat{p}}$.

The presented regular dependencies of the piano hammer parameters on the key number can be used as a tool for systematical exploration of the process of the hammer–string interaction, or they can be useful for the purpose of improvement of the technological process of the piano hammer manufacturing.

In this study, the aforementioned knowledge regarding the hammer felt compression is used to develop the wool felt model.

3 Wool felt model

In order to analyze the influence of hereditary felt features on the behavior and form of the waves traveling through the felt, the propagation of plane one-dimensional longitudinal wave in an unbounded half-space is considered. The classical equation of motion is in the form

$$\rho \frac{\partial^2 u}{\partial t^2} = \frac{\partial \sigma}{\partial x}, \quad (8)$$

where u is the displacement, σ is the stress, and ρ is the density.

The constitutive equation of microstructured wool felt is derived in a similar manner as the hammer felt model was obtained above. Instead of relation (1), we assume and propose

$$\sigma(\epsilon) = E \epsilon^p(t). \quad (9)$$

Here, $\epsilon = \partial u / \partial x$ is the strain, and E is Young's modulus, and p is the nonlinearity parameter. Because this approach is based on the piano hammer model, we are limited to describe only the compression wave propagation ($\epsilon(x, t) \geq 0$).

Following Rabotnov [7] once again, we obtain the constitutive equation of microstructured wool felt by replacing the constant value of Young's modulus E in expression (9) by a time-dependent operator $E_d [1 - \mathcal{R}(t) *]$, with the relaxation function in the form (2). This means that for the case of one-dimensional deformation and for any rate of loading, the hysteretic felt material is defined with the aid of the constitutive equation

$$\sigma(\epsilon) = E_d [\epsilon^p(t) - \mathcal{R}(t) * \epsilon^p(t)], \quad (10)$$

where the constant E_d is the dynamic Young's modulus of the felt. From Eq. (10), it follows that if $t \ll \tau_0$, then we obtain the constitutive equation for the fast felt compression,

$$\sigma(\epsilon) = E_d \epsilon^p(t), \quad (11)$$

and if $t \gg \tau_0$, then we have constitutive equation for the slow compression,

$$\sigma(\epsilon) = E_s \epsilon^p(t). \quad (12)$$

In these two cases, the loading and unloading of the felt occurs in the similar manner. Quantity $E_s = E_d(1 - \gamma)$ is the static Young's modulus of the felt material.

Substituting (10) in Eq. (8) and eliminating the integral term lead to the equation in the following form:

$$\rho \frac{\partial^2 u}{\partial t^2} + \rho \tau_0 \frac{\partial^3 u}{\partial t^3} - E_d \left\{ (1 - \gamma) \frac{\partial}{\partial x} \left[\left(\frac{\partial u}{\partial x} \right)^p \right] + \tau_0 \frac{\partial^2}{\partial x \partial t} \left[\left(\frac{\partial u}{\partial x} \right)^p \right] \right\} = 0. \quad (13)$$

The analysis of Eq. (13) was reported in [10] where it was shown that the second term of Eq. (13) is significantly smaller compared to the other terms for any reasonable rate of the felt loading (up to 10 m/s). This fact corresponds to the inequality $u \gg \tau_0 |u_t|$, and therefore, the three-parameter model of the felt was derived in [10]. Neglecting the second term of (13), and comparing the new form of Eq. (13) with Eq. (8), one can assume another form of constitutive equation of microstructured wool felt,

$$\sigma(\epsilon) = E_s \left[\epsilon^p + \alpha_0 \frac{\partial(\epsilon^p)}{\partial t} \right], \quad (14)$$

where

$$\alpha_0 = \tau_0 / \delta, \quad \delta = 1 - \gamma. \quad (15)$$

Equation (14) is a nonlinear modification of the well-known Kelvin–Voigt model.

Further, this study will consider the equation of motion in its full form (13). The dimensionless form of the equation is obtained by using the nondimensional variables that are introduced by relations

$$u \Rightarrow u/l_0, \quad x \Rightarrow x/l_0, \quad t \Rightarrow t/\alpha_0, \quad (16)$$

where

$$l_0 = c_d \alpha_0 \sqrt{\delta}, \quad c_d = \sqrt{E_d / \rho}, \quad c_s = c_d \sqrt{\delta}. \quad (17)$$

Thus, Eq. (13) in terms of the nondimensional displacement variable $u(x, t)$ takes the following form:

$$\left[(u_x)^p \right]_x - u_{tt} + \left[(u_x)^p \right]_{xt} - \delta u_{ttt} = 0, \quad (18)$$

and for the strain variable $\epsilon(x, t)$

$$(\epsilon^p)_{xx} - \epsilon_{tt} + (\epsilon^p)_{xxt} - \delta \epsilon_{ttt} = 0. \quad (19)$$

Several samples of felt pads made of the same material that is used in piano hammers manufacturing were subjected to the static stress–strain tests. The average value of the static Young's modulus of the pads was estimated to be $E_s = 0.6$ MPa. The average value of the felt density was $\rho = 10^3$ kg/m³. For realistic results, one should select the values of hereditary parameters γ and τ_0 as follows: $\gamma = 0.99$ and $\tau_0 = 20$ μ s. This selection results in the following values of material constants:

$$\delta = 0.01, \quad E_d = 60 \text{ MPa}, \quad c_s = 25 \text{ m/s}, \quad c_d = 250 \text{ m/s}. \quad (20)$$

Using those values of material constants, the space and time scales l_0 and α_0 used in (16) are

$$l_0 = 50 \text{ mm}, \quad \alpha_0 = 2 \text{ ms}. \quad (21)$$

4 Linear case and dispersion relations

Peculiar characteristics of wave propagation in the wool felt are revealed already in the linear case $p = 1$,

$$\epsilon_{xx} - \epsilon_{tt} + \epsilon_{xxt} - \delta\epsilon_{ttt} = 0. \quad (22)$$

The fundamental solution of this equation has the form of traveling waves,

$$\epsilon(x, t) = \hat{\epsilon} e^{i\kappa x - i\omega t}, \quad (23)$$

where i is the imaginary unit, κ is the wavenumber, ω is the angular frequency, and $\hat{\epsilon}$ is an amplitude. The dispersion law $\Phi(\kappa, \omega) = 0$ of Eq. (22) is defined by the relation

$$i\delta\omega^3 - \omega^2 - i\kappa^2\omega + \kappa^2 = 0. \quad (24)$$

In the case of the boundary value problem, the general solution of Eq. (22) has the following form:

$$\epsilon(x, t) = \frac{1}{2\pi} \int_{-\infty}^{\infty} \Theta(\omega) e^{i\kappa(\omega)x - i\omega t} d\omega, \quad (25)$$

where $\Theta(\omega)$ is the Fourier transform of the boundary value of the strain prescribed at $x = 0$,

$$\Theta(\omega) = \int_{-\infty}^{\infty} \epsilon(0, t) e^{i\omega t} dt. \quad (26)$$

In case of the initial value problem, the general solution of Eq. (22) has the following form:

$$\epsilon(x, t) = \frac{1}{2\pi} \int_{-\infty}^{\infty} \chi(\kappa) e^{i\kappa x - i\omega(\kappa)t} d\kappa, \quad (27)$$

where $\chi(\kappa)$ is the Fourier transform of an initial disturbance of the strain prescribed at $t = 0$,

$$\chi(\kappa) = \int_{-\infty}^{\infty} \epsilon(x, 0) e^{i\kappa x} dx. \quad (28)$$

The dependencies $\kappa = \kappa(\omega)$ and $\omega = \omega(\kappa)$ are derived from dispersion relation (24). In general case, κ and ω are complex quantities. In order to provide the dispersion analysis in context with a boundary value problem, we rewrite the wavenumber $\kappa(\omega)$ in the form

$$\kappa(\omega) = k(\omega) + i\lambda(\omega), \quad (29)$$

where $k = \text{Re}(\kappa)$ and $\lambda = \text{Im}(\kappa)$. Using this notation, expression (23) can be rewritten as follows:

$$\epsilon(x, t) = \hat{\epsilon} e^{i(k+i\lambda)x - i\omega t} = e^{-\lambda x} \hat{\epsilon} e^{ikx - i\omega t}. \quad (30)$$

From here, it is clear that for positive values of λ it acts as an exponential decay constant for the spectral components of the wave that is propagating along the positive direction of the space axis. In other words, spectral components decay exponentially as $x, t \rightarrow \infty$ for $\lambda(\omega) > 0$. On the other hand, if $\lambda(\omega) < 0$, then the amplitudes of the spectral components grow exponentially as they propagate further along the positive direction of the x -axis. In the latter case, the solution of linear Eq. (22) becomes highly unstable for $t \gg 0$.

5 Dispersion analysis

As discussed above, in order to study the wave propagation along the x -axis, one needs to solve the dispersion relation (24) against wavenumber κ . The solution is in the form

$$\kappa(\omega) = \frac{\omega\sqrt{1-i\delta\omega}}{\sqrt{1-i\omega}}. \quad (31)$$

For real values of k and λ , the dispersion relation (24) takes the following form:

$$k^2 + 2ik\lambda - \lambda^2 - ik^2\omega + 2k\lambda\omega + i\lambda^2\omega - \omega^2 + i\delta\omega^3 = 0. \quad (32)$$

In order to study real and imaginary parts separately, the system of equations in the form

$$\begin{cases} k^2 - \lambda^2 + 2k\lambda\omega - \omega^2 = 0 \\ 2k\lambda - \omega(k^2 - \lambda^2) + \delta\omega^3 = 0 \end{cases} \quad (33)$$

is solved and analyzed. Solutions with respect to k and λ are

$$k(\omega) = LM \left(\sqrt{1+M^2} - 1 \right)^{-1/2}, \quad (34)$$

$$\lambda(\omega) = L \left(\sqrt{1+M^2} - 1 \right)^{1/2}, \quad (35)$$

where

$$L = \omega \sqrt{\frac{1+\delta\omega^2}{2(1+\omega^2)}}, \quad M = \frac{(1-\delta)\omega}{1+\delta\omega^2}. \quad (36)$$

The frequency dependencies $k(\omega) = \text{Re}(\kappa)$ and $\lambda(\omega) = \text{Im}(\kappa)$ of dispersion relation (24) are displayed in Fig. 2 for the various values of the material parameter δ . Parameter δ can have values on the interval $\delta = [0, 1]$.

If $\delta = 1$, then from (34) and (35) one can find

$$k(\omega) = \omega, \quad \lambda(\omega) = 0. \quad (37)$$

This real valued nondispersive case is evident from the study of expression (10). Because $\gamma = 1 - \delta = 0$, it follows that $\mathcal{R}(t) = 0$, and instead of Eq. (10), we are left with the constitutive equation in the form (11). This form is not dependent on the rate of the felt loading. In fact, Eq. (11) describes a usual elastic material, in which the wave propagates without attenuation.

In case of $\omega \rightarrow \infty$, it is easy to see that $k(\omega) \rightarrow \omega\sqrt{\delta}$ and that

$$\lim_{\omega \rightarrow \infty} \lambda(\omega) = \frac{1-\delta}{2\sqrt{\delta}}. \quad (38)$$

For large frequencies, the exponential decay constant λ depends only on the parameter δ .

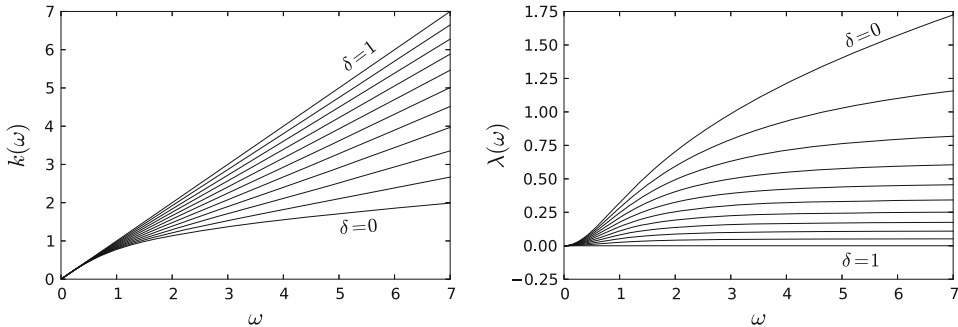


Fig. 2 Dispersion relations $k(\omega)$ and $\lambda(\omega)$ for various values of parameter δ in range $[0.0, 1.0]$ with step 0.1

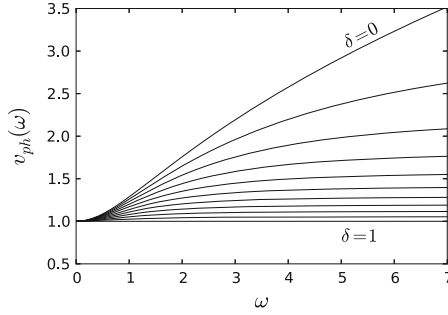


Fig. 3 Phase velocity as a function of frequency for various values of the parameter δ in range $[0.0, 1.0]$ with step 0.1

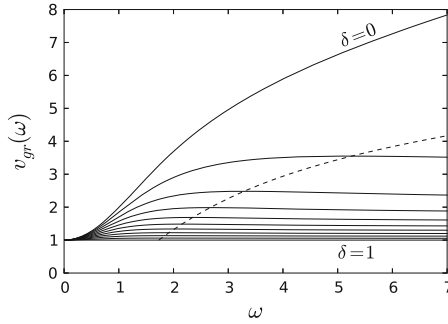


Fig. 4 Group velocity as a function of frequency for various values of the parameter δ in range $[0.0, 1.0]$ with step 0.1. The maximum of v_{gr} for $\delta < 1$ is shown by a *dashed line*

The phase velocity is defined as $v_{ph}(\omega) = \omega/k$, and it takes the following general form:

$$v_{ph} = \frac{\sqrt{2(1 + \omega^2)(N - \delta\omega^2 - 1)}}{(1 - \delta)\omega}, \quad (39)$$

where

$$N = \sqrt{(1 + \omega^2)(1 + \delta^2\omega^2)}. \quad (40)$$

The frequency dependence $v_{ph}(\omega)$ for various values of parameter δ is shown in Fig. 3. In case of $\delta = 1$, the phase velocity becomes $v_{ph}(\omega) = 1$ [cf. relationship (37)]. For large frequencies, the phase velocity has a limit

$$\lim_{\omega \rightarrow \infty} v_{ph}(\omega) = \frac{1}{\sqrt{\delta}}. \quad (41)$$

Taking into account (16) and (17), the range of dimensional values of the phase velocity is $c_s \leq v_{ph} < c_d$.

The group velocity, which is defined as $v_{gr}(\omega) = d\omega/dk = (dk/d\omega)^{-1}$, takes in this case the following general form:

$$v_{gr} = \frac{2(1 + \omega^2)^2 \sqrt{2(1 + \delta^2\omega^2)} (N - \delta\omega^2 - 1)^{3/2}}{\omega(1 - \delta)[(1 + 3\delta^2)\omega^4 - (2N + 2\delta N - 3\delta^2 - 5)\omega^2 - 4(N - 1)]}, \quad (42)$$

where N is defined by relation (40). The frequency dependence $v_{gr}(\omega)$ for various values of the parameter δ is presented in Fig. 4. In case of $\delta = 1$, the group velocity $v_{gr}(\omega) = 1$ [cf. relationship (37)]. For large frequencies, the group velocity has the same limit as the phase velocity has,

$$\lim_{\omega \rightarrow \infty} v_{gr}(\omega) = \frac{1}{\sqrt{\delta}}. \quad (43)$$

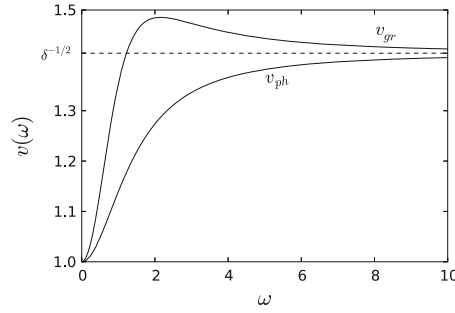


Fig. 5 Comparison of group and phase velocities for a single value of the parameter $\delta = 0.5$. The dashed line shows the limit for the large frequencies

The essential difference between the behavior of phase and group velocities is that the phase velocity is a monotonic function of frequency, while the group velocity has a maximum. The maximum of different values of δ is located on the dashed line shown in Fig. 4. A comparison of the two velocities for a single value of δ is presented in Fig. 5. In the wool felt, the group velocity is larger than the phase velocity for any positive frequency. This means that the felt is a material with anomalous dispersion. This fact is true for $\delta < 1$ because as mentioned above, if $\delta = 1$, then $v_{gr} = v_{ph} = 1$, and we have nondispersive case.

6 Numerical solution of the boundary value problem

The aim of this study was to analyze the one-dimensional deformation (strain) wave propagation inside the felt material along the x axis. This calls for the solution of the boundary value problem of Eq. (19). A boundary value of the strain prescribed at $x = 0$ is selected in the following form:

$$\epsilon(0, t) = A \left(\frac{t}{t_0} \right)^3 e^{3(1-t/t_0)}, \quad (44)$$

where t_0 defines the time coordinate corresponding to the maximum of a pulse amplitude. This form of a pulse is continuous and smooth. The front of a pulse satisfies the necessary conditions $\epsilon(0, 0) = \epsilon_t(0, 0) = \epsilon_{tt}(0, 0) = 0$.

The solution to this problem is obtained numerically by applying the finite difference method. A more suitable form of Eq. (19) for the finite difference approximation can be obtained by integrating Eq. (19) over time. This yields

$$\epsilon_{tt} = (\epsilon^p)_{xx} - \gamma \int_0^t (\epsilon^p)_{xx} e^{\xi-t} d\xi, \quad (45)$$

where $\gamma = 1 - \delta$. Initially ($t \leq 0$), the felt material is assumed to be at rest, thus $\epsilon(x, 0) = \epsilon_t(x, 0) = 0$.

Further, the solution of the boundary value problem (45), (44) is presented and analyzed.

6.1 Linear case

Figure 6 shows the numerical solution of the boundary value problem (45) and (44), with the nonlinearity parameter $p = 1$. A pulse propagates through the felt material in the direction of the x -axis. The form of a pulse determined by the boundary value (44) is presented for three sequential time moments, and for three different values of parameter δ . The dashed lines show corresponding decays of pulse amplitudes. These curves are plotted through the pulses' maxima.

The numerical results presented in Fig. 6 are calculated for a pulse with boundary value where the parameter $t_0 = 1/2$. The additional calculations were also repeated for the boundary values where $t_0 = 1$ and $t_0 = 1/3$.

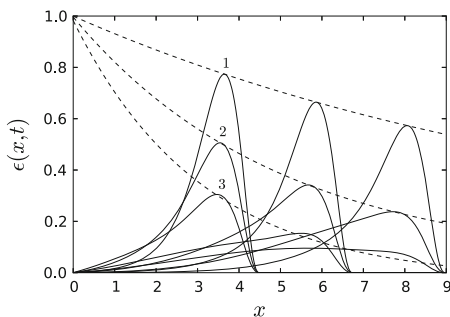


Fig. 6 Snapshots of the pulses' profiles shown for time moments $t = 4.5$, $t = 6.75$, and $t = 9.0$, varying the parameter δ . The boundary value parameter $t_0 = 1/2$. The *dashed lines* show the amplitude decay. For a pulse 1 ($\delta = 0.8$), the corresponding amplitude decay function is $e^{-0.08x}$; for a pulse 2 ($\delta = 0.5$), the amplitude decay function is $e^{-0.20x}$; for a pulse 3 ($\delta = 0.2$), the amplitude decay function is $e^{-0.32x}$

Table 1 Comparison of exponential decay constants λ for different values of parameter δ and frequency ω

δ	t_0	ω	$\lambda(\omega)$	λ_{num}	$ \lambda(\omega) - \lambda_{\text{num}} $
0.2	1	1	0.246	0.304	0.058
	1/2	2	0.493	0.321	0.172
	1/3	3	0.632	0.361	0.271
0.5	1	1	0.142	0.184	0.042
	1/2	2	0.254	0.201	0.053
	1/3	3	0.300	0.214	0.086
0.8	1	1	0.053	0.068	0.015
	1/2	2	0.087	0.077	0.010
	1/3	3	0.099	0.082	0.017

Here, we suppose that the *fundamental* spectral component ω of a pulse (44) is estimated from relationship $\omega t_0 \simeq 1$. This is a rough approximation, but below, it is shown that the resulting numerical calculations are in agreement with the dispersion analysis.

Table 1 displays the parameter δ , the boundary value parameter t_0 , the corresponding value of frequency ω , the value of $\lambda(\omega)$, the value of exponential decay constant λ_{num} , and the absolute value of the difference between λ and λ_{num} . We conclude that the results presented in Table 1 for all values of δ are sufficient enough to confirm that the values of numerically calculated decay constants λ_{num} and the exponential decay constant λ defined by relation (35) are approximately the same. This means that in principle this approach can be used to verify the decay constants for any specific value of t_0 rather accurately.

6.2 Nonlinear case

In this section, the effects of the nonlinearity of the wool felt model on the wave propagation are considered. We examine the influence of the nonlinearity parameter p , and the effect of an initial pulse amplitude A on the evolution of the wave form during its propagation through the felt material.

Figure 7 shows the numerical solution of the boundary value problem (45) and (44). The solution of the problem is presented for three sequential time moments, and for three different values of the nonlinearity parameter p . In this example, the amplitude $A = 0.1$ of the boundary value is a constant for all cases presented.

In Fig. 7, it is possible to see that the front of a pulse becomes steeper as it propagates through the felt material. This pulse steepening increases with the growth of the value of the parameter p . It means that the group velocity is larger than the phase velocity. This phenomenon confirms our conclusion that the felt is a material with anomalous dispersion (*vide* Fig. 5).

The effect of an initial pulse amplitude A on a pulse evolution is presented in Fig. 8. The numerical solution is presented for three sequential time moments, and for three different values of the initial amplitude A of the boundary value (44). It is possible to see that a forward-facing slope of a pulse is strongly dependent on the pulse amplitude A . For larger amplitudes, the maximum point or the crest of a pulse (shown by bullets)

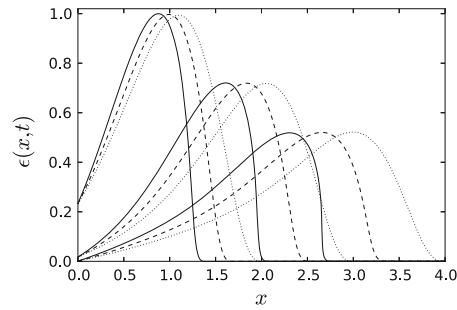


Fig. 7 Evolution of a nonlinear pulse ($t_0 = 1/2$, $A = 0.1$) for three sequential time moments $t = 2$, $t = 3$, and $t = 4$. Material parameters selected $\delta = 0.2$, $p = 1.5$ shown by *solid line*, $p = 1.25$ shown by *dashed line*, $p = 1.0$ (linear case) shown by *dotted line*. Results are normalized

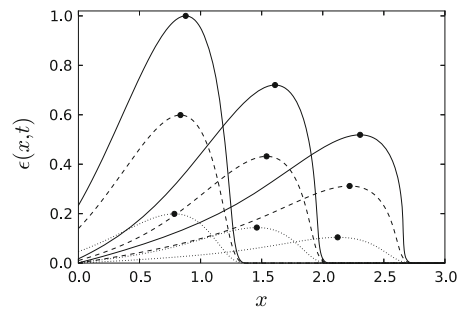


Fig. 8 Evolution of a nonlinear pulse ($t_0 = 1/2$) for three sequential time moments $t = 2$, $t = 3$, and $t = 4$. Material parameters selected $\delta = 0.2$, $p = 1.5$, initial amplitude $A = 0.1$ shown by *solid line*, $A = 0.06$ shown by *dashed line*, $A = 0.02$ shown by *dotted line*. *Bullet* show the position of maximum. Results are normalized

propagates faster than the front of a pulse. Accumulation of this effect results in the eventual pulse breaking. This means that eventually the shock wave will be formed. To simulate this phenomenon, our numerical scheme must be adjusted to the purpose of description of the propagation of discontinuities on the wave front. A detailed analysis of this problem is in progress.

The progressive forward leaning of a propagating pulse can be explained by the fact that the group velocity is larger than the phase velocity. Also, this phenomenon is related to nonlinear features of the felt material and increases with the increase of the amplitude of the initial boundary disturbance.

The animations of the simulated wave pulses propagation through the felt discussed in Sect. 6 are available for viewing at the supplementary Web page of this article.¹

7 Conclusions

We have derived a nonlinear constitutive equation of microstructured wool felt based on the experimental results of piano hammers testing. Using this model, the boundary value problem that describes the propagation of deformation waves in the felt material is considered in the current study. In case of the linear felt-type material, the dispersion analysis of the model is carried out, and the dependencies of the phase and group velocities on the felt parameters are obtained. It is shown that the group velocity is always larger than the phase velocity, and therefore, the wool felt is a medium with anomalous dispersion.

The numerical solution of the linear boundary value problem is used to estimate a strain pulse amplitude decay during its propagation through the felt. It is shown that in the linear case the decay constants may be obtained rather accurately by using dispersion analysis.

¹ Supplementary web page of the article: <http://www.cs.ioc.ee/~dima/feltdeform.html>.

A strain pulse propagation in nonlinear felt is also considered. The general influence of the nonlinear parameter p on a pulse evolution is investigated. It is concluded that the front of a pulse becomes steeper as it propagates through the felt material and that this pulse steepening increases with the growth of the value of the parameter p .

The effect of an initial pulse amplitude A on the nonlinear wave propagation is simulated. It is shown that for larger amplitudes the maximum point or the crest of a pulse propagates faster than the front of a pulse. This is related to the fact that the group velocity is larger than the phase velocity and confirms our assumptions about the felt as a medium with anomalous dispersion.

It is revealed that the front slope of a pulse is strongly determined by a pulse amplitude A . Such a process results in the formation of the shock wave, which is directly caused by the nonlinear features of the microstructured felt material. The originality of the presented model is expressed in the fact that the parameter p that describes the felt nonlinearity may be any real number >1 , including the noninteger values. The solution of the novel wave Eqs. (18) and (19) reflects many physical effects as demonstrated in this paper. In conclusion, we may state that the wool felt is a strongly dissipative and dispersive nonlinear medium, with a strong damping effect.

Acknowledgments This research was supported by the EU through the European Regional Development Fund, and by the Estonian Ministry of Education and Research (SF 0140077s08). The authors would like to thank Prof. Aleksander Klauson from Tallinn University of Technology for his assistance in the stress–strain testing of the felt pads.

References

1. Ghosh, M.: An experimental study of the duration of contact of an elastic hammer striking a damped pianoforte string. *Indian J. Phys.* **7**, 365–382 (1932)
2. Hall, D.E., Askenfelt, A.: Piano string excitation. V. Spectra for real hammers and strings. *J. Acoust. Soc. Am.* **83**, 1627–1638 (1988)
3. Yanagisawa, T., Nakamura, K., Aiko, H.: Experimental study on force–time curve during the contact between hammer and piano string. *J. Acoust. Soc. Jpn.* **37**, 627–633 (1981)
4. Yanagisawa, T., Nakamura, K.: Dynamic compression characteristics of piano hammer. *Trans. Music. Acoust. Tech. Group Meet. Acoust. Soc. Jpn.* **1**, 14–18 (1982)
5. Yanagisawa, T., Nakamura, K.: Dynamic compression characteristics of piano hammer felt. *J. Acoust. Soc. Jpn.* **40**, 725–729 (1984)
6. Stulov, A.: Hysteretic model of the grand piano hammer felt. *J. Acoust. Soc. Am.* **97**, 2577–2585 (1995)
7. Rabotnov, Yu.N.: *Elements of Hereditary Solid Mechanics*, Chap. 17. MIR Publishers, Moscow (1980)
8. Stulov, A., Magi, A.: Piano hammer testing device. *Proc. Estonian Acad. Sci. Eng.* **6**, 259–267 (2000)
9. Stulov, A.: Experimental and computational studies of piano hammers. *Acta Acoust. United Acoust.* **91**, 1086–1097 (2005)
10. Stulov, A.: Dynamic behavior and mechanical features of wool felt. *Acta Mech.* **169**, 13–21 (2004)

Publication IV

T. Peets, D. Kartofelev, K. Tamm, and J. Engelbrecht,
“Waves in microstructured solids and negative group velocity,”
EPL - A Letters Journal Exploring the Frontiers of Physics, vol. 103, no. 1,
pp. 16001-p1–16001-p6, 2013.
DOI: 10.1209/0295-5075/103/16001

Waves in microstructured solids and negative group velocity

T. PEETS^{1(a)}, D. KARTOFEEV², K. TAMM² and J. ENGELBRECHT²

¹ *Department of Mathematics, City University of Hong Kong - 83 Tat Chee Avenue, Kowloon Tong, Kowloon, Hong Kong*

² *Centre for Nonlinear Studies, Institute of Cybernetics at Tallinn University of Technology Akadeemia tee 21, Tallinn 12618, Estonia, EU*

received 29 April 2013; accepted in final form 27 June 2013

published online 23 July 2013

PACS 62.30.+d – Mechanical and elastic waves; vibrations

PACS 46.40.Cd – Mechanical wave propagation (including diffraction, scattering, and dispersion)

PACS 43.20.+g – General linear acoustics

Abstract – Waves with negative group velocity (NGV) were discovered in optics by Sommerfeld and Brillouin, and experimentally verified in many cases, for example in left-handed media. For waves in solids, such an effect is described mostly in layered media. In this paper, it is demonstrated that in microstructured solids, waves with NGV may also exist leading to backwards pulse propagation. Two physical cases are analysed: a Mindlin-type hierarchical (a scale within a scale) material and a felt-type (made of fibres) material. For both cases, the dispersion analysis of one-dimensional waves shows that there exists certain ranges of physical parameters which lead to NGV. The results can be used in dispersion engineering for designing materials with certain properties.

Copyright © EPLA, 2013

Introduction. – In general, wave motion is characterised by the group velocity c_g and the phase velocity c_{ph} which typically have the same direction. However, there are cases for which the phase and group velocities differ by signs (*i.e.*, are in opposite directions) within certain frequency ranges. In general terms, this means a negative group velocity (NGV) which indicates that the peak of the pulse propagates backwards.

Such a phenomenon was first considered by Sommerfeld [1] and Brillouin [2] for waves in a Lorentzian medium as a mathematical possibility in dispersion analysis. Mandel'shtam [3] showed that NGV may appear in crystal lattices. Garrett and McCumber [4] revisited the ideas of Sommerfeld [1] and Brillouin [2] and showed that the phenomenon described by them may be observed and is therefore physical.

In optical materials NGV are a direct consequence of classical interference between different frequency components in a gain-assisted anomalous dispersion region [5]. The gain-assisted anomalous dispersion is due to changes in the refractive index. Such a situation may appear in atomic cesium vapor cells [5] or, in general terms, in left-handed media (LHM) with negative refractive index [6].

LHM is actually a result of the left-handed relationship between the electric field, magnetic field and propagation vector [6]. It has been shown that NGV was observed in a Lorentz dielectric modelled by an oscillator where the oscillator strength was negative [7]. Such a result is directly related to the original studies of Sommerfeld [1] and Brillouin [2]. McDonald [8] showed that a gas with two closely spaced spectral lines of angular frequencies can be modelled like a medium with negative oscillators which give rise to the gain.

In solids, waves with NGV have been studied mostly for layered media. For Lamb waves, which appear in a material composed of solid-liquid-solid layers (for example, glass-water-glass), NGV appears near cut-off frequencies (at which c_{ph} is divergent) of certain propagation modes [9]. The conditions which govern NGV are related to the acoustic impedance ratio. In laminated composite (carbon/epoxy, glass/epoxy, etc.) circular cylindrical shells it is the ratio of radius to thickness of layers which can alter the pattern of the group velocity spectra [10]. Mandel'shtam [3] has attributed NGV in a crystal lattice to periodically varying parameters (density, permittivity). On the other hand, the dispersion relation for longitudinal waves in elastic solid cylinders, known as the Pochhammer equation, displays also NGV depending on the value of the Poisson ratio [11].

^(a) On a leave from Institute of Cybernetics at Tallinn University of Technology - Tallinn, Estonia, EU; E-mail: tanelp@cens.ioc.ee

The attention to waves with NGV has increased in the context of metamaterials which are engineered with a purpose to create effective macroscopic behaviour. The idea is to use small inhomogeneities to control dispersive effects and that is why sometimes the notion of dispersion engineering is used [12]. The first metamaterials were electromagnetic [13] but presently there is a considerable interest in acoustic metamaterials [14–16] which permit sound focusing and confinement.

These studies show that various structural inhomogeneities may lead to NGV. Phononic crystals may be built by placing elastic or fluid inclusions inside a different fluid or elastic matrix which results in a negative refractive index [16]. It is possible to build materials with certain resonators within each unit cell [14,16]. Then it is possible to get a negative refractive index or even a negative mass density [16] or an effective negative dynamic modulus [14]. It is possible to build also periodically loaded transmission lines with a negative refractive index [12].

Finally it must be noted that although NGV leads to backward propagation, the causality principle is not violated. This has been analysed in detail by Toll [17] for general dispersion relations and by Dogariu *et al.* [5] in the context of NGV. It has also been shown experimentally by Gehring *et al.* [18] that although the peak of the pulse propagates backward, the energy flow is always forward.

In this paper we demonstrate that in microstructured solids in which several microstructures exist, cases of NGV can also be observed. The mathematical models of wave propagation studied here are either of a Mindlin-type [19] or felt-type materials [20]. After our straightforward studies reported in [21], we discovered that the detailed dispersion analysis may lead to NGV. The results of this analysis are reported in this paper. It is shown that only in case of special combinations of physical parameters such effects are possible.

Mathematical models. –

Mindlin-type model. We follow the models from Berezovski *et al.* [21] derived for multiple microstructures. Two different models are possible: a hierarchical one (a scale within a scale) and a concurrent one (two coexistent microstructures). In both cases, the influence of microstructures is described by internal variables [22] φ_1 and φ_2 . The free energy functions reflect the differences between these two models. In the case of the hierarchical microstructure, the free energy function is

$$W = \frac{1}{2}\alpha u_x^2 + A_1 u_x \varphi_1 + \frac{1}{2}B_1 \varphi_1^2 + \frac{1}{2}C_1 (\varphi_1)_x^2 + A_{12} (\varphi_1)_x \varphi_2 + \frac{1}{2}B_2 \varphi_2^2 + \frac{1}{2}C_2 (\varphi_2)_x^2 \quad (1)$$

and in the case of the concurrent microstructure it is

$$W = \frac{1}{2}\alpha u_x^2 + A_1 u_x \varphi_1 + \frac{1}{2}B_1 \varphi_1^2 + \frac{1}{2}C_1 (\varphi_1)_x^2 + A_2 u_x \varphi_2 + \frac{1}{2}B_2 \varphi_2^2 + \frac{1}{2}C_2 (\varphi_2)_x^2, \quad (2)$$

where α , A_i , B_i and C_i are material constants. The physical meanings of these parameters are related to bulk (α) and microstress moduli (C_i), coupling effects (A_i) and the interactive force (B_i). The subscripts refer to the microstructure φ_1 or φ_2 , respectively.

The energy functions (1) and (2), where only the quadratic terms are kept, correspond to linear stress-strain relations [23] and they reflect directly the coupling: in (1) the coupling is consecutively between u_x and φ_1 and between φ_1 and φ_2 ; in (2) the coupling is in parallel between u_x and φ_1 and between u_x and φ_2 (and not directly between φ_1 and φ_2). In such a way, both these energy functions can be considered as basic for multiple microstructures with different coupling effects.

The corresponding governing equations derived from the Euler-Lagrange equations are

$$\rho u_{tt} = \alpha u_{xx} + A_1 (\varphi_1)_{tt}, \quad (3a)$$

$$I_1 (\varphi_1)_{tt} = C_1 (\varphi_1)_{xx} - A_1 u_x - B_1 \varphi_1 + A_{12} (\varphi_2)_{tt}, \quad (3b)$$

$$I_2 (\varphi_2)_{tt} = C_2 (\varphi_2)_{xx} - A_{12} (\varphi_1)_{tt} - B_2 \varphi_2, \quad (3c)$$

and

$$\rho u_{tt} = \alpha u_{xx} + A_1 (\varphi_1)_{tt} + A_2 (\varphi_2)_{tt}, \quad (4a)$$

$$I_1 (\varphi_1)_{tt} = C_1 (\varphi_1)_{xx} - A_1 u_x - B_1 \varphi_1, \quad (4b)$$

$$I_2 (\varphi_2)_{tt} = C_2 (\varphi_2)_{xx} - A_2 u_x - B_2 \varphi_2, \quad (4c)$$

respectively.

Felt-type model. The governing equation of motion which describes the propagation of a 1D strain wave (pulse) in a felt-type material is derived from the classical equation of motion

$$\rho u_{tt} = \sigma_x \quad (5)$$

by assuming that the stress σ is governed by a power-law with a time-dependent operator

$$\sigma(v) = E_d \left[v^p(t) - \frac{\varepsilon}{\tau_0} \exp(-t/\tau_0) * v^p(t) \right], \quad (6)$$

where $v = \partial u / \partial x$ is the strain, ε is the hereditary (hysteretic) amplitude, τ_0 is the relaxation time, E_d is the dynamic Young modulus and p is the compliance nonlinearity parameter describing physical properties of the material [20,24]. Here $*$ denotes the convolution integral with the exponential kernel function. Equation (6) is a modification of the well-known Kelvin-Voigt model proposed specifically for a felt-type material [25].

This leads to the nonlinear dimensionless equation in terms of displacement

$$[(U_X)^p]_X - U_{TT} + [(U_X)^p]_{XT} - \delta U_{TTT} = 0, \quad (7)$$

where $\delta = 1 - \varepsilon$ is related to the stress relaxation and $U = u/\tau_0(\rho\delta/E_d)^{1/2}$, $X = x/\tau_0(\rho\delta/E_d)^{1/2}$, $T = t\delta/\tau_0$ are the dimensionless displacement, coordinate and time, respectively. The special case if $\delta = 1$ means that $\varepsilon = 0$ and all hereditary properties cease.

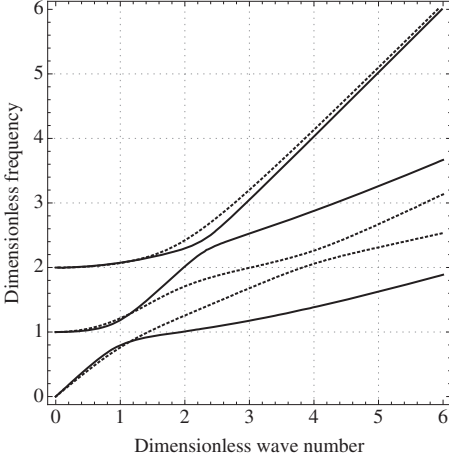


Fig. 1: Dispersion curves of eq. (9) (solid lines) and eq. (10) (dashed lines) for $c_{A1} = c_{A2} = c_{A12} = 0.4c_0$, $c_1 = 0.5c_0$, $c_2 = 0.3c_0$.

The dispersion analysis of harmonic waves is possible for the simplest linearised version of eq. (7). This can be easily achieved for $p = 1$. Then the linear form of eq. (7) is

$$U_{XX} - U_{TT} + U_{XXT} - \delta U_{TTT} = 0. \quad (8)$$

Dispersion analysis. –

Mindlin-type model. The dispersion relations for the hierarchical and concurrent multiscale models [21] are

$$\begin{aligned} & (c_0^2 k^2 - \omega^2)(c_1^2 k^2 - \omega^2 + \omega_1^2)(c_2^2 k^2 - \omega^2 + \omega_2^2) \\ & - c_{A12}^2 \omega^2 k^2 (c_0^2 k^2 - \omega^2) \\ & - c_{A1}^2 \omega_1^2 k^2 (c_2^2 k^2 - \omega^2 + \omega_2^2) = 0 \end{aligned} \quad (9)$$

and

$$\begin{aligned} & (c_0^2 k^2 - \omega^2)(c_1^2 k^2 - \omega^2 + \omega_1^2)(c_2^2 k^2 - \omega^2 + \omega_2^2) \\ & + c_{A2}^2 \omega_2^2 k^2 (c_1^2 k^2 - \omega^2 + \omega_1^2) \\ & - c_{A1}^2 \omega_1^2 k^2 (c_2^2 k^2 - \omega^2 + \omega_2^2) = 0, \end{aligned} \quad (10)$$

respectively. The parameters are defined as

$$\begin{aligned} c_0^2 &= \frac{\alpha}{\rho}, & c_1^2 &= \frac{C_1}{I_1}, & c_2^2 &= \frac{C_2}{I_2}, & c_{A1}^2 &= \frac{A_1^2}{\rho_0 B_1}, \\ c_{A2}^2 &= \frac{A_2^2}{\rho B_2}, & c_{A12}^2 &= \frac{A_{12}^2}{I_1 B_2}, & \omega_1^2 &= \frac{B_1}{I_1}, & \omega_2^2 &= \frac{B_2}{I_2}. \end{aligned} \quad (11)$$

Here c_0 is the velocity in the macrostructure, c_{Ai} reflects the velocity change due to the coupling, c_i are characteristic velocities of the microstructures and ω_i are characteristic frequencies.

The characteristic set of dispersion curves for both cases is shown in fig. 1. In both cases three branches of curves

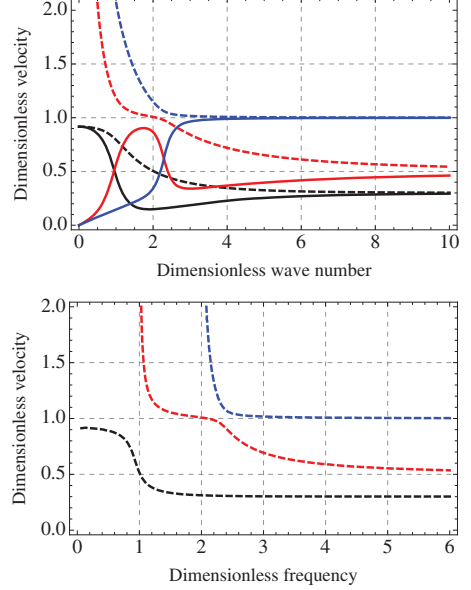


Fig. 2: (Colour on-line) Phase (dashed lines) and group velocity (solid lines) curves against wave number (top plot) and against frequency (bottom plot) of eq. (9) for $c_{A1} = c_{A12} = 0.4c_0$, $c_1 = 0.5c_0$, $c_2 = 0.3c_0$.

appear: one acoustic branch (bottom curves) and two optical branches (upper curves). It is clear that while the asymptotic behaviour of both models is similar there are differences in the region of moderate wavelengths, which is the area where NGV can emerge. Further we focus on wave motion in a solid which possesses the hierarchical microstructure.

The phase ($c_{ph} = \omega/k$) and group velocity ($c_{gr} = \partial\omega/\partial k$) curves for eq. (9) are plotted in fig. 2. The top panel represents the velocity curves against the dimensionless wave number and the bottom panel against the dimensionless frequency.

The upper optical branch (blue lines) first approaches to the velocity c_1/c_0 and then to the c_0 . The lower optical branch (red lines) approaches the same values but in different order —first to the velocity c_0 and then to the velocity c_1/c_0 .

The asymptotic velocities for the acoustic dispersion branch (black lines) are $[(c_0^2 - c_{A1}^2)/c_0^2]^{1/2}$ in the long-wave limit and c_2 in the short-wave limit. In the area of moderate wavelengths (*i.e.*, the dimensionless wave number is in the range $1 \lesssim kc_0/\omega_1 \lesssim 3$) the asymptotic value of the group velocity is $[(c_1^2 - c_{A12}^2)/c_0^2]^{1/2}$.

Phase velocity against the dimensionless frequency curves have also been plotted in the bottom panel of fig. 2 where it can be seen that the transition from long-wave velocity to short-wave velocity is much faster in

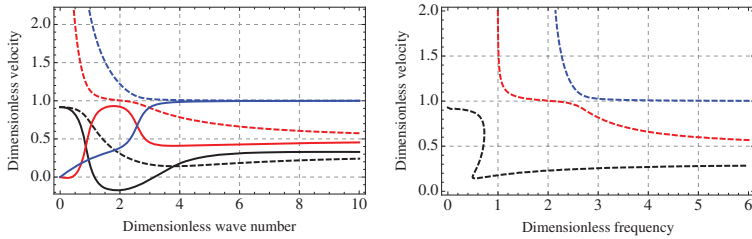


Fig. 3: (Colour on-line) Phase (dashed lines) and group velocity (solid lines) curves against wave number of eq. (9) (left plot) and phase velocity curves against frequency (right plot) for $c_{A1} = 0.4c_0$, $c_{A12} = 0.6c_0$, $c_1 = 0.5c_0$, $c_2 = 0.3c_0$.

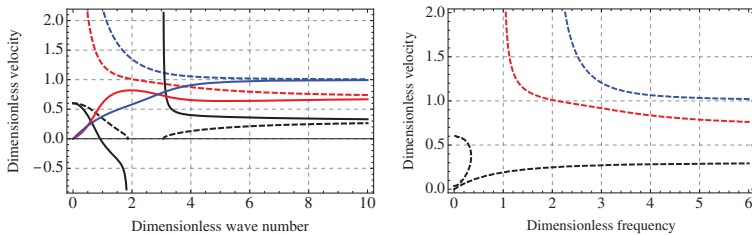


Fig. 4: (Colour on-line) Phase (dashed lines) and group velocity (solid lines) curves against wave number of eq. (9) (left plot) and phase velocity curves against frequency (right plot) for $c_{A1} = c_{A12} = 0.8c_0$, $c_1 = 0.7c_0$, $c_2 = 0.3c_0$.

the frequency domain than in the wave number domain (fig. 2).

NGV will emerge in the case of the hierarchical model (9) when $c_1 < c_{A12}$ as is the case in fig. 3. Mathematically this happens because the asymptotic velocity $[(c_1^2 - c_{A12}^2)/c_0^2]^{1/2}$ becomes imaginary. Making use of the relations (11) we can rewrite this limiting velocity as

$$\frac{1}{I_1} \left(C_1 - \frac{A_{12}^2}{B_2} \right). \quad (12)$$

This allows us to write down the condition for NGV in terms of material parameters as

$$\frac{A_{12}^2}{B_2} > C_1, \quad (13)$$

which means that the emergence of NGV is related to the coupling effects between the two scales (parameters A and B) and the microstrain of the second microstructure (parameter C).

In fig. 3 it is possible to see that the middle optical curve also approaches the value $[(c_1^2 - c_{A12}^2)/c_0^2]^{1/2}$ in the very long-wavelength limit. The behaviour of the phase velocity curves against the dimensionless frequency has been plotted for reference in the right plot of fig. 3 where it can be seen that in the case of NGV there is frequency region where the phase speed is multi-valued. These regions are related to the frequencies where the group velocity changes from positive to negative and vice versa.

It is also known that the optical branches are related to non-propagating oscillations (cf. lattice theory [26]). In the case of the hierarchical microstructure with dispersion relation (9) two optical branches can be very close to each other (cf. fig. 1) at certain frequencies. This can be considered as a pre-resonant situation at which these non-propagating oscillations are coupled resulting in NGV. This is also the reason for the multi-valued nature of the phase velocity.

Another case of NGV is plotted in fig. 4 where a band gap can be seen. This band gap disappears when the velocity c_2 becomes larger. Since $c_2^2 = C_2/I_2$ it may be speculated that the material parameters of the second microstructure are most significant in the emergence of NGV.

Finally, we note that NGV does not emerge in case of the concurrent model (10). It is easy to see in fig. 1 that the limiting velocities for the acoustic dispersion curve is c_1 in the moderate-wavelength region and c_2 in the short-wave limit. The middle optical curve approaches the same lines of asymptotic velocities in different order [21].

Felt-type model. The dispersion relation for the felt-type material is

$$i\delta\omega^3 - \omega^2 - ik^2\omega + k^2 = 0. \quad (14)$$

It is clear that the imaginary part of the complex solution of eq. (14) in the current case corresponds to the exponential decay of amplitudes which are important when wave profiles are analysed. Here the group and phase

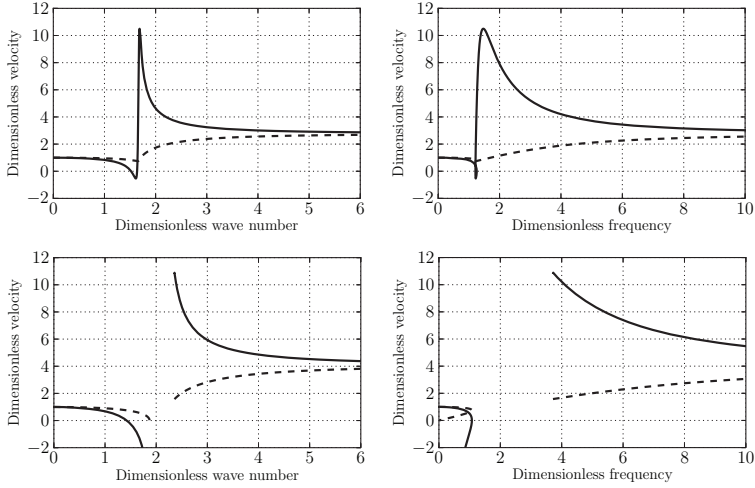


Fig. 5: Group and phase velocities of the felt model for the $\delta = 0.13$ (top row) and $\delta = 0.06$ (bottom row). Group velocities are plotted using solid lines, corresponding phase velocities using dashed lines.

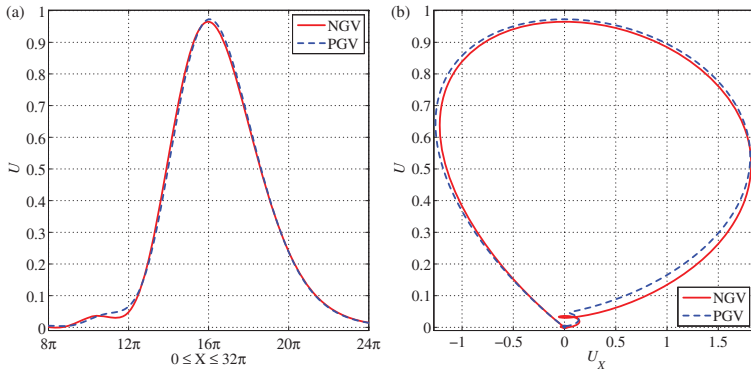


Fig. 6: (Colour on-line) Pulses for the NGV and the positive group velocity (PGV) normalised with respect to velocities to facilitate comparison (a) and the corresponding phase plots (b). Parameters are $c_{A1} = 0.4c_0, c_{A12} = 0.6c_0, c_1 = 0.5c_0, c_2 = 0.3c_0$ for NGV and $c_{A1} = 0.4c_0, c_{A12} = 0.6c_0, c_1 = 0.7c_0, c_2 = 0.3c_0$ for PGV.

velocities are calculated from the real valued solution of ω .

Depending on the value of the parameter δ four distinct cases of dispersion can be identified. NGV will emerge when $0 \leq \delta < 0.135$ [20]. Figure 5 depicts examples of NGV for the two cases of the felt-type model. It is easy to recognise that the behaviour of the felt-type model is similar to the Mindlin-type model; especially to the case depicted in fig. 4. When $\delta > 0.135$ then NGV disappears; when $\delta = 1$ the dispersionless relation between the frequency and wave number follows.

The existence of NGV in case of small values of δ hints that emergence of NGV in the case of felt-type model is

related to the stress-relaxation of the material. Note also the similarity of curves depicted in fig. 5 with those in fig. 3 and fig. 4.

Discussion. – We have demonstrated that in the case of solids, NGV can appear in microstructured materials. Here the cases of the hierarchical Mindlin-type model and the felt-type models are considered. Based on the analysis of phase and group velocities it is shown that NGV exist in a certain range of physical parameters. In the case of a material with two microstructures (a scale within a scale) it is shown that the emergence of NGV is related to the coupling effects between the two scales. In the

case of two concurrent microstructures there will be no such an effect. In the case of a felt-type material, the emergence of NGV depends on the parameter δ which is related to stress relaxation in such a microstructured material.

The general influence of NGV on pulse shapes is not very strong similarly to the behaviour of pulses in optical media [5,18]. It must be noted that in optics NGV is usually space dependent but here NGV is observed at certain wave numbers if the physical conditions are satisfied (see condition (13)). We solved system (3) numerically using the pseudo-spectral method [27] for an input of a pulse-type (sech^2) excitation. Such an excitation has a wide spectrum of frequencies and the excitation is chosen such that the dominant frequencies are in the region of NGV (see fig. 3). The results are shown in fig. 6 for a pulse moving to the right — profiles in fig. 6(a) and the corresponding phase plots in fig. 6(b). The profile corresponding to NGV has shifted some frequencies to the left (slowing down) while in case of the positive group velocity (condition (13) not satisfied) this effect caused by dispersion is much weaker. The expected asymmetry of the pulse which is also demonstrated in [28] for a general case, is well demonstrated in both cases. In general terms, the results are similar to those in optics (see fig. 6 in [5] and fig. 2 in [18]). A detailed analysis of wave profiles including harmonic pulses and wave packets is in progress.

Although both cases analysed above are related to microstructured materials, the physical mechanisms which cause the emergence of NGV, are different. In the case of a Mindlin-type hierarchical microstructure the mechanism is based on coupling effects (parameter A_{12}), in the case of a felt-type material the phenomenological stress-strain relation models the relaxation effect while the scale of the microstructure is not taken into account. However, the stress-strain relation (6) explains the behaviour of the felt-type materials reflecting the influence of fiber-to-fiber forces in the macrolevel. The possibility of the existence of NGV in microstructured materials broadens the ideas of dispersion engineering [12] to be used, for example, in designing negative refractive acoustic media [15].

This research was supported by the European Union through the European Regional Development Fund, by the Estonian Ministry of Education and Research (SF0140077s08) and by the Estonian Science Foundation (Grant No. 8702). Support from the City University of Hong Kong is gratefully acknowledged by one of the authors (TP). Authors thank Prof. JONATHAN WILEY for

carefully reading the manuscript. We are also grateful to the reviewer for his/her comments.

REFERENCES

- [1] SOMMERFELD A., *Ann. Phys. (Leipzig)*, **44** (1914) 177.
- [2] BRILLOUIN L., *Ann. Phys. (Leipzig)*, **44** (1914) 203.
- [3] MANDEL'SHTAM L. I., *Zh. Eksp. Teor. Fiz.*, **15** (1945) 475.
- [4] GARRETT C. and McCUMBER D. E., *Phys. Rev. A*, **1** (1970) 305.
- [5] DOGARIU A., KUZMICH A. and WANG L., *Phys. Rev. A*, **63** (2001) 053806.
- [6] WOODLEY J. and MOJAHEDI M., *Phys. Rev. E*, **70** (2004) 046603.
- [7] BOLDA E. L., GARRISON J. C. and CHIAO R. Y., *Phys. Rev. A*, **49** (1994) 2938.
- [8] McDONALD K. T., *Am. J. Phys.*, **69** (2001) 607.
- [9] NISHIMIYA K., MIZUTANI K., WAKATSUKI N. and YAMAMOTO K., *Proceedings of Acoustics 08, Paris (Société Française d'Acoustique (SFA))* 2008, p. 3613.
- [10] XI Z. C., LIU G. R., LAM K. Y. and SHANG H. M., *J. Acoust. Soc. Am.*, **108** (2000) 2179.
- [11] SMITH S. H., *IEEE Trans. Sonics Ultrason.*, **18** (1971) 123.
- [12] MOJAHEDI M. and ELEFThERIADES G. V., in *Negative Refraction Metamaterials: Fundamental Properties and Applications*, edited by ELEFThERIADES G. V. and BALMAIN K. G. (J. Wiley, Hoboken, NJ) 2005, pp. 367–398.
- [13] SHELBY R. A., *Science*, **292** (2001) 77.
- [14] FANG N., XI D., XU J., AMBATI M., SRITURAVANICH W., SUN C. and ZHANG X., *Nat. Mater.*, **5** (2006) 452.
- [15] GUENNEAU S., MOVCHAN A., PÉTURSSON G. and ANANTHA RAMAKRISHNA S., *New J. Phys.*, **9** (2007) 399.
- [16] FOK L., AMBATI M. and ZHANG X., *MRS Bull.*, **33** (2008) 931.
- [17] TOLL J. S., *Phys. Rev.*, **104** (1956) 1760.
- [18] GEHRING G. M., SCHWEINSBERG A., BARSIC C., KOSTINSKI N. and BOYD R. W., *Science*, **312** (2006) 895.
- [19] ENGELBRECHT J., BEREZOVSKI A., PASTRONE F. and BRAUN M., *Philos. Mag.*, **85** (2005) 4127.
- [20] KARTOFEL'EV D. and STULOV A., *Propagation of deformation waves in wool felt*, submitted to *Acta Mech.*
- [21] BEREZOVSKI A., ENGELBRECHT J. and PEETS T., *Mech. Res. Commun.*, **37** (2010) 531.
- [22] VÁN P., BEREZOVSKI A. and ENGELBRECHT J., *J. Non-Equilib. Thermodyn.*, **33** (2008) 235.
- [23] MINDLIN R. D., *Arch. Ration. Mech. Anal.*, **16** (1964) 51.
- [24] MEYERS M. A. and CHAWLA K. K., *Mechanical Behaviors of Materials* (Cambridge University Press) 2009, Chapt. 13.11.
- [25] STULOV A., *Acta Mech.*, **16** (2004) 13.
- [26] BRILLOUIN L., *Wave Propagation in Periodic Structures* (Dover Publishers Inc., New York) 1953.
- [27] ENGELBRECHT J., SALUPERE A. and TAMM K., *Wave Motion*, **48** (2011) 717.
- [28] ENGELBRECHT J., BEREZOVSKI A. and SALUPERE A., *Wave Motion*, **44** (2007) 493.

Publication V

D. Kartofelev and A. Stulov,

“Wave propagation and dispersion in microstructured wool felt.”

The manuscript has been submitted³ to the journal *Wave Motion*⁴.

³The manuscript was submitted on March 5, 2014. As of July 3, 2014 (printing date of the thesis) the manuscript was undergoing a peer review.

⁴The rules of the publisher prevent publication of the manuscript of Publication V prior to acceptance. Official committee members and opponents will be given a copy of the submitted manuscript to enable them to carry out a judicious review of this thesis.

Appendix B

CURRICULUM VITAE

Curriculum Vitae

1. Personal data

Name Dmitri Kartofelev
Date of birth April 12, 1985
Birthplace Tallinn, Estonia
Nationality Estonian

2. Contact information

Address Institute of Cybernetics at TUT, Akadeemia Rd. 21, 12618
 Tallinn, Estonia
Phone +372 620 4173
Mobile +372 5566 8475
E-mail dima@cs.ioc.ee

3. Education

2009– ... Tallinn University of Technology, Faculty of Science, Institute of Cybernetics, Engineering Physicist, PhD studies.
2007–2009 Tallinn University of Technology, Faculty of Science, Engineering Physicist, MSc.
2004–2007 Tallinn University of Technology, Faculty of Science, Engineering Physicist, BSc.

4. Language competence

Estonian native language
Russian native language
English good
Finnish basic

5. Professional employment

- 2013– ... Institute of Cybernetics, Centre for Nonlinear Studies, Laboratory of Nonlinear Dynamics, Tallinn University of Technology, **Junior Researcher**.
- 2013–2013 Department of Signal Processing and Acoustics, School of Electrical Engineering, Aalto University, **Visiting Researcher**.
- 2012–2012 Nonlinear Dynamics Course (EMR 0060), **Teaching Assistant**, Tallinn University of Technology.
- 2009–2013 Institute of Cybernetics, Department of Mechanics and Applied Mathematics, Centre for Nonlinear Studies, Tallinn University of Technology, **Engineer**.
- 2008–2009 Institute of Cybernetics, Department of Mechanics and Applied Mathematics, Centre for Nonlinear Studies, Tallinn University of Technology, **Technician**.

6. Defended theses

- MSc thesis **“Analysis of vibration spectra of piano string,”** Faculty of Science, Tallinn University of Technology, Supervisor: Senior Researcher Anatoli Stulov, Year of defence 2009.
- BSc thesis **“Action of travelling wave on a piano bridge,”** Faculty of Science, Tallinn University of Technology, Supervisor: Senior Researcher Anatoli Stulov, Year of defence 2007.

7. Field of research

- 2008– ... Musical acoustics of stringed instruments, nonlinear dynamics, deformation waves in microstructured solids.

8. Scientific work

Supervised theses

- 2012–2014 Co-supervisor of the MSc thesis **“Magnetic pickup non-linearity,”** by *M. Mustonen*, Faculty of Science, Tallinn University of Technology.

2011–2012 Co-supervisor of the BSc thesis “**Bass guitar sound modelling based on experimental data,**” by *M. Mustonen*, Faculty of Science, Tallinn University of Technology.

Original research papers

1. D. Kartofelev and A. Stulov, “Wave propagation and dispersion in microstructured wool felt.”
The manuscript has been submitted to the journal *Wave Motion*.
2. D. Kartofelev and A. Stulov, “Propagation of deformation waves in wool felt,” *Acta Mechanica*, Online first, pp. [1–11], 2014.
DOI: 10.1007/s00707-014-1109-1
3. A. Stulov and D. Kartofelev, “Vibration of strings with nonlinear supports,” *Applied Acoustics*, vol. 76, pp. 223–229, February 2014.
4. T. Peets, D. Kartofelev, K. Tamm, and J. Engelbrecht, “Waves in microstructured solids and negative group velocity,” *EPL – A Letters Journal Exploring the Frontiers of Physics*, vol. 103, no. 1, pp. 16001-p1–16001-p6, 2013.

Articles in conference proceedings

1. D. Kartofelev, M. Mustonen, A. Stulov, and V. Välimäki, “Application of high-speed line scan camera for string vibration measurements,” in *Proceedings of International Symposium on Musical Acoustics ISMA 2014*, (Le Mans, France), pp. [1–5], 2014.
2. M. Mustonen, D. Kartofelev, A. Stulov, and V. Välimäki, “Experimental verification of pickup nonlinearity,” in *Proceedings of International Symposium on Musical Acoustics ISMA 2014*, (Le Mans, France), pp. [1–5], 2014.
3. M. Pàmies-Vilà, I. A. Kubilay, D. Kartofelev, M. Mustonen, A. Stulov, and V. Välimäki, “High-speed line-camera measurements of a vibrating string,” in *Proceedings of Baltic-Nordic Acoustic Meeting BNAM 2014*, (Tallinn, Estonia), pp. [1–8], 2014
4. D. Kartofelev, A. Stulov, H.-M. Lehtonen, and V. Välimäki, “Modeling a vibrating string terminated against a bridge with arbitrary geometry,” in *Proceedings of SMAC 2013, 4th Stockholm Music Acoustics Conference*, (R. Bresin and A. Askenfelt, eds.), (Stockholm, Sweden), pp. 626–632, KTH Royal Institute of Technology, 2013.

5. D. Kartofelev and A. Stulov, "Influence of the edge of the cast iron frame curvature on the spectrum of the piano string vibration," in *Proceedings of the Second 2nd Talk on Music Acoustics "Bridging the Gaps"*, (Vienna, Austria), pp. 85–88, 2010.
6. D. Kartofelev and A. Stulov, "Piano hammer–string interaction: the influence of the elastic parameters of bass hammers on the contact time duration," in *Proceedings of ACOUSTICS High Tatras 2009: 34th International Acoustical Conference - EAA Symposium*, (Nový Smokovec, Slovakia), pp. [1–4], 2009.
7. D. Kartofelev and A. Stulov, "Vibration of the string with nonlinear contact condition," in *Nonlinear Acoustics - Fundamentals and Applications: 18th International Symposium on Nonlinear Acoustics (ISNA 18)*, (B. O. Enflo, C. M. Hedberg, and L. Kari, eds.), (Stockholm, Sweden), pp. 621–624, AIP Conference Proceedings; 1022, American Institute of Physics, Melville, NY, 2008.

Abstracts

1. D. Kartofelev and J. Engelbrecht, "Algorithmic melody composition based on fractal geometry of music," in *Book of Abstracts: FUDoM 13 Finno-Ugric International Conference on Mechanics*, (B. Fekete, ed.), (Ráckeve, Hungary), p. 28, 2013.
2. J. Engelbrecht, T. Peets, and D. Kartofelev, "Negative group velocity may appear in microstructured solids," in *Book of Abstracts: FUDoM 13 Finno-Ugric International Conference on Mechanics*, (B. Fekete, ed.), (Ráckeve, Hungary), pp. 46–47, 2013.
3. A. Stulov and D. Kartofelev, "Acoustical properties of the wool felt," in *SAPeM 2011: Symposium on the Acoustics of Poro-Elastic Materials*, (Ferrara, Italy), p. [1], 2011.
4. D. Kartofelev and A. Stulov, "Propagation of deformation waves in the piano hammer felt," in *International Conference on Complexity of Nonlinear Waves: Book of Abstracts*, (A. Berezovski and T. Soomere, eds.), (Tallinn, Estonia), p. 36, Tallinn University of Technology, 2009.

Conference presentations

1. D. Kartofelev, M. Mustonen, A. Stulov, and V. Välimäki, "Application of high-speed line scan camera for string vibration measurements," at *International Symposium on Musical Acoustics ISMA 2014*, Le Mans, France, July 7–12, 2014.

2. D. Kartofelev and J. Engelbrecht,
 “Algorithmic melody composition based on fractal geometry of music,”
 at *FUDoM 13 Finno-Ugric International Conference On Mechanics*,
 Ráckeve, Hungary, August 11–15, 2013.
3. D. Kartofelev, A. Stulov, H.-M. Lehtonen, and V. Välimäki,
 “Modeling a vibrating string terminated against a bridge with ar-
 bitrary geometry,” at *SMAC Stockholm Music Acoustics Conference
 2013/SMC Sound and Music Computing Conference 2013*,
 Stockholm, Sweden, July 30–August 3, 2013.
4. D. Kartofelev and A. Stulov,
 “Acoustical properties of the wool felt,” at *Symposium on the Acoustics
 of Poro-Elastic Materials (SAPEM 2011)*,
 Ferrara, Italy, December 14–16, 2011.
5. D. Kartofelev and A. Stulov,
 “Influence of the edge of the cast iron frame curvature on the spectrum
 of the piano string vibration,” at *2nd Vienna Talk on Music Acoustics*,
 Vienna, Austria, September 19–21, 2010.
6. D. Kartofelev and A. Stulov,
 “Propagation of deformation wave in the piano hammer felt material,”
 at *International Conference on Complexity of Nonlinear Waves*,
 Tallinn, Estonia, October 5–7, 2009.
7. D. Kartofelev and A. Stulov,
 “Piano hammer–string interaction: the influence of the elastic param-
 eters of bass hammer on contact time duration,” at *ACOUSTICS High
 Tatras 2009, 34th International Acoustical Conference - EAA Symposi-
 um*,
 Nový Smokovec, High Tatras, Slovakia, September 28–30, 2009.
8. D. Kartofelev and A. Stulov,
 “Vibration of the string with nonlinear contact condition,” at *18th
 International Symposium on Nonlinear Acoustics*,
 Stockholm, Sweden, July 7–10, 2008.
9. D. Kartofelev and A. Stulov,
 “String vibrations induced by piano hammers,” at *XIII Estonian Days
 of Mechanics*,
 Tallinn, Estonia, September 15–16, 2008.

Elulookirjeldus

1. Isikuandmed

Nimi Dmitri Kartofelev
Sünniaeg 12. aprill 1985
Sünnikoht Tallinn, Eesti
Kodakondsus Eesti

2. Kontaktandmed

Aadress TTÜ Küberneetika Instituut, Akadeemia tee 21, 12618
 Tallinn, Eesti
Telefon +372 620 4173
Mobiil +372 5566 8475
E-post dima@cs.ioc.ee

3. Haridus

2009– ... Tallinna Tehnikaülikool, Matemaatika-loodusteaduskond,
 Küberneetika Instituut, tehniline füüsika, doktoriõpe.
2007–2009 Tallinna Tehnikaülikool, Matemaatika-loodusteaduskond,
 tehniline füüsika, MSc.
2004–2007 Tallinna Tehnikaülikool, Matemaatika-loodusteaduskond,
 tehniline füüsika, BSc.

4. Keelteoskus

eesti keel emakeel
vene keel emakeel
inglise keel hea
soome keel põhiteadmised

5. Teenistuskäik

- 2013– ... Küberneetika Instituut, Mittelineaarsete protsesside analüüsi keskus, Mittelineaarse dünaamika laboratoorium, Tallinna Tehnikaülikool, **nooremteadur**.
- 2013–2013 Signaali töötlemise ja akustika osakond, Elektrotehnika kõrgkool, Aalto Ülikool, **külalisteadur**.
- 2012–2012 Mittelineaarne dünaamika kursus (EMR 0060), **assistent**, Tallinna Tehnikaülikool.
- 2009–2013 Küberneetika Instituut, Mehaanika ja rakendusmatemaatika osakond, Mittelineaarsete protsesside analüüsi keskus, Tallinna Tehnikaülikool, **insener**.
- 2008–2009 Küberneetika Instituut, Mehaanika ja rakendusmatemaatika osakond, Mittelineaarsete protsesside analüüsi keskus, Tallinna Tehnikaülikool, **tehnik**.

6. Kaitstud lõputööd

- Magistritöö **”Klaverikeele võnkumise spektrite analüüs”**, Matemaatika-loodusteaduskond, Tallinna Tehnikaülikool, Juhendaja: vanemteadur Anatoli Stulov, kaitsmise aasta 2009.
- Bakalaureuse-**”Leviva laine mõjust tiibklaveri sillale”**, Matemaatika-
töö loodusteaduskond, Tallinna Tehnikaülikool, Juhendaja: vanemteadur Anatoli Stulov, kaitsmise aasta 2007.

7. Teadustöö põhisuunad

- 2008– ... Keelpillide akustika, mittelineaarne dünaamika, deformatsioonilained mikrostruktuuriga tahkistes.

8. Teadustegevus

Teadusartiklite, konverentsiteaside, konverentsiettekannete ja juhendamiste loetelud on välja toodud ingliskeelse elulookirjelduse juures.

**DISSERTATIONS DEFENDED AT
TALLINN UNIVERSITY OF TECHNOLOGY ON
NATURAL AND EXACT SCIENCES**

1. **Olav Kongas.** Nonlinear Dynamics in Modeling Cardiac Arrhythmias. 1998.
2. **Kalju Vanatalu.** Optimization of Processes of Microbial Biosynthesis of Isotopically Labeled Biomolecules and Their Complexes. 1999.
3. **Ahto Buldas.** An Algebraic Approach to the Structure of Graphs. 1999.
4. **Monika Drews.** A Metabolic Study of Insect Cells in Batch and Continuous Culture: Application of Chemostat and Turbidostat to the Production of Recombinant Proteins. 1999.
5. **Eola Valdre.** Endothelial-Specific Regulation of Vessel Formation: Role of Receptor Tyrosine Kinases. 2000.
6. **Kalju Lott.** Doping and Defect Thermodynamic Equilibrium in ZnS. 2000.
7. **Reet Koljak.** Novel Fatty Acid Dioxygenases from the Corals *Plexaura homomalla* and *Gersemia fruticosa*. 2001.
8. **Anne Paju.** Asymmetric oxidation of Prochiral and Racemic Ketones by Using Sharpless Catalyst. 2001.
9. **Marko Vendelin.** Cardiac Mechanoenergetics *in silico*. 2001.
10. **Pearu Peterson.** Multi-Soliton Interactions and the Inverse Problem of Wave Crest. 2001.
11. **Anne Menert.** Microcalorimetry of Anaerobic Digestion. 2001.
12. **Toomas Tiivel.** The Role of the Mitochondrial Outer Membrane in *in vivo* Regulation of Respiration in Normal Heart and Skeletal Muscle Cell. 2002.
13. **Olle Hints.** Ordovician Scolecodonts of Estonia and Neighbouring Areas: Taxonomy, Distribution, Palaeoecology, and Application. 2002.
14. **Jaak Nõlvak.** Chitinozoan Biostratigraphy in the Ordovician of Baltoscandia. 2002.
15. **Liivi Kluge.** On Algebraic Structure of Pre-Operad. 2002.
16. **Jaanus Lass.** Biosignal Interpretation: Study of Cardiac Arrhythmias and Electromagnetic Field Effects on Human Nervous System. 2002.
17. **Janek Peterson.** Synthesis, Structural Characterization and Modification of PAMAM Dendrimers. 2002.
18. **Merike Vaher.** Room Temperature Ionic Liquids as Background Electrolyte Additives in Capillary Electrophoresis. 2002.
19. **Valdek Mikli.** Electron Microscopy and Image Analysis Study of Powdered Hardmetal Materials and Optoelectronic Thin Films. 2003.
20. **Mart Viljus.** The Microstructure and Properties of Fine-Grained Cermets. 2003.
21. **Signe Kask.** Identification and Characterization of Dairy-Related *Lactobacillus*. 2003.
22. **Tiiu-Mai Laht.** Influence of Microstructure of the Curd on Enzymatic and Microbiological Processes in Swiss-Type Cheese. 2003.

23. **Anne Kuusksalu.** 2–5A Synthetase in the Marine Sponge *Geodia cydonium*. 2003.
24. **Sergei Bereznev.** Solar Cells Based on Polycrystalline Copper–Indium Chalcogenides and Conductive Polymers. 2003.
25. **Kadri Kriis.** Asymmetric Synthesis of C₂-Symmetric Bimorpholines and Their Application as Chiral Ligands in the Transfer Hydrogenation of Aromatic Ketones. 2004.
26. **Jekaterina Reut.** Polypyrrole Coatings on Conducting and Insulating Substrates. 2004.
27. **Sven Nõmm.** Realization and Identification of Discrete-Time Nonlinear Systems. 2004.
28. **Olga Kijatkina.** Deposition of Copper Indium Disulphide Films by Chemical Spray Pyrolysis. 2004.
29. **Gert Tamberg.** On Sampling Operators Defined by Rogosinski, Hann and Blackman Windows. 2004.
30. **Monika Übner.** Interaction of Humic Substances with Metal Cations. 2004.
31. **Kaarel Adamberg.** Growth Characteristics of Non-Starter Lactic Acid Bacteria from Cheese. 2004.
32. **Imre Vallikivi.** Lipase-Catalysed Reactions of Prostaglandins. 2004.
33. **Merike Peld.** Substituted Apatites as Sorbents for Heavy Metals. 2005.
34. **Vitali Syritski.** Study of Synthesis and Redox Switching of Polypyrrole and Poly(3,4-ethylenedioxythiophene) by Using *in-situ* Techniques. 2004.
35. **Lee Põllumaa.** Evaluation of Ecotoxicological Effects Related to Oil Shale Industry. 2004.
36. **Riina Aav.** Synthesis of 9,11-Secosterols Intermediates. 2005.
37. **Andres Braunbrück.** Wave Interaction in Weakly Inhomogeneous Materials. 2005.
38. **Robert Kitt.** Generalised Scale-Invariance in Financial Time Series. 2005.
39. **Juss Pavelson.** Mesoscale Physical Processes and the Related Impact on the Summer Nutrient Fields and Phytoplankton Blooms in the Western Gulf of Finland. 2005.
40. **Olari Ilison.** Solitons and Solitary Waves in Media with Higher Order Dispersive and Nonlinear Effects. 2005.
41. **Maksim Säkki.** Intermittency and Long-Range Structurization of Heart Rate. 2005.
42. **Enli Kiipli.** Modelling Seawater Chemistry of the East Baltic Basin in the Late Ordovician–Early Silurian. 2005.
43. **Igor Golovtsov.** Modification of Conductive Properties and Processability of Polyparaphenylene, Polypyrrole and polyaniline. 2005.
44. **Katrin Laos.** Interaction Between Furcellaran and the Globular Proteins (Bovine Serum Albumin-Lactoglobulin). 2005.
45. **Arvo Mere.** Structural and Electrical Properties of Spray Deposited Copper Indium Disulphide Films for Solar Cells. 2006.

46. **Sille Ehala.** Development and Application of Various On- and Off-Line Analytical Methods for the Analysis of Bioactive Compounds. 2006.
47. **Maria Kulp.** Capillary Electrophoretic Monitoring of Biochemical Reaction Kinetics. 2006.
48. **Anu Aaspõllu.** Proteinases from *Vipera lebetina* Snake Venom Affecting Hemostasis. 2006.
49. **Lyudmila Chekulayeva.** Photosensitized Inactivation of Tumor Cells by Porphyrins and Chlorins. 2006.
50. **Merle Uudsemaa.** Quantum-Chemical Modeling of Solvated First Row Transition Metal Ions. 2006.
51. **Tagli Pitsi.** Nutrition Situation of Pre-School Children in Estonia from 1995 to 2004. 2006.
52. **Angela Ivask.** Luminescent Recombinant Sensor Bacteria for the Analysis of Bioavailable Heavy Metals. 2006.
53. **Tiina Lõugas.** Study on Physico-Chemical Properties and Some Bioactive Compounds of Sea Buckthorn (*Hippophae rhamnoides* L.). 2006.
54. **Kaja Kasemets.** Effect of Changing Environmental Conditions on the Fermentative Growth of *Saccharomyces cerevisiae* S288C: Auxo-accelerostat Study. 2006.
55. **Ildar Nisamedtinov.** Application of ^{13}C and Fluorescence Labeling in Metabolic Studies of *Saccharomyces* spp. 2006.
56. **Alar Leibak.** On Additive Generalisation of Voronoi's Theory of Perfect Forms over Algebraic Number Fields. 2006.
57. **Andri Jagomägi.** Photoluminescence of Chalcopyrite Tellurides. 2006.
58. **Tõnu Martma.** Application of Carbon Isotopes to the Study of the Ordovician and Silurian of the Baltic. 2006.
59. **Marit Kauk.** Chemical Composition of CuInSe_2 Monograin Powders for Solar Cell Application. 2006.
60. **Julia Kois.** Electrochemical Deposition of CuInSe_2 Thin Films for Photovoltaic Applications. 2006.
61. **Iлона Oja Açık.** Sol-Gel Deposition of Titanium Dioxide Films. 2007.
62. **Tiia Anmann.** Integrated and Organized Cellular Bioenergetic Systems in Heart and Brain. 2007.
63. **Katrin Trummal.** Purification, Characterization and Specificity Studies of Metalloproteinases from *Vipera lebetina* Snake Venom. 2007.
64. **Gennadi Lessin.** Biochemical Definition of Coastal Zone Using Numerical Modeling and Measurement Data. 2007.
65. **Enno Pais.** Inverse problems to determine non-homogeneous degenerate memory kernels in heat flow. 2007.
66. **Maria Borissova.** Capillary Electrophoresis on Alkylimidazolium Salts. 2007.
67. **Karin Valmsen.** Prostaglandin Synthesis in the Coral *Plexaura homomalla*: Control of Prostaglandin Stereochemistry at Carbon 15 by Cyclooxygenases. 2007.

68. **Kristjan Piirimäe.** Long-Term Changes of Nutrient Fluxes in the Drainage Basin of the Gulf of Finland – Application of the PolFlow Model. 2007.
69. **Tatjana Dedova.** Chemical Spray Pyrolysis Deposition of Zinc Sulfide Thin Films and Zinc Oxide Nanostructured Layers. 2007.
70. **Katrin Tomson.** Production of Labelled Recombinant Proteins in Fed-Batch Systems in *Escherichia coli*. 2007.
71. **Cecilia Sarmiento.** Suppressors of RNA Silencing in Plants. 2008.
72. **Vilja Mardla.** Inhibition of Platelet Aggregation with Combination of Antiplatelet Agents. 2008.
73. **Maie Bachmann.** Effect of Modulated Microwave Radiation on Human Resting Electroencephalographic Signal. 2008.
74. **Dan Hüvonen.** Terahertz Spectroscopy of Low-Dimensional Spin Systems. 2008.
75. **Ly Villo.** Stereoselective Chemoenzymatic Synthesis of Deoxy Sugar Esters Involving *Candida antarctica* Lipase B. 2008.
76. **Johan Anton.** Technology of Integrated Photoelasticity for Residual Stress Measurement in Glass Articles of Axisymmetric Shape. 2008.
77. **Olga Volobujeva.** SEM Study of Selenization of Different Thin Metallic Films. 2008.
78. **Artur Jõgi.** Synthesis of 4'-Substituted 2,3'-dideoxynucleoside Analogues. 2008.
79. **Mario Kadastik.** Doubly Charged Higgs Boson Decays and Implications on Neutrino Physics. 2008.
80. **Fernando Pérez-Caballero.** Carbon Aerogels from 5-Methylresorcinol-Formaldehyde Gels. 2008.
81. **Sirje Vaask.** The Comparability, Reproducibility and Validity of Estonian Food Consumption Surveys. 2008.
82. **Anna Menaker.** Electrosynthesized Conducting Polymers, Polypyrrole and Poly(3,4-ethylenedioxythiophene), for Molecular Imprinting. 2009.
83. **Lauri Ilison.** Solitons and Solitary Waves in Hierarchical Korteweg-de Vries Type Systems. 2009.
84. **Kaia Ernits.** Study of In₂S₃ and ZnS Thin Films Deposited by Ultrasonic Spray Pyrolysis and Chemical Deposition. 2009.
85. **Veljo Sinivee.** Portable Spectrometer for Ionizing Radiation “Gammamapper”. 2009.
86. **Jüri Virkepu.** On Lagrange Formalism for Lie Theory and Operadic Harmonic Oscillator in Low Dimensions. 2009.
87. **Marko Piirsoo.** Deciphering Molecular Basis of Schwann Cell Development. 2009.
88. **Kati Helmja.** Determination of Phenolic Compounds and Their Antioxidative Capability in Plant Extracts. 2010.
89. **Merike Sõmera.** Sobemoviruses: Genomic Organization, Potential for Recombination and Necessity of P1 in Systemic Infection. 2010.

90. **Kristjan Laes.** Preparation and Impedance Spectroscopy of Hybrid Structures Based on CuIn_3Se_5 Photoabsorber. 2010.
91. **Kristin Lippur.** Asymmetric Synthesis of 2,2'-Bimorpholine and its 5,5'-Substituted Derivatives. 2010.
92. **Merike Luman.** Dialysis Dose and Nutrition Assessment by an Optical Method. 2010.
93. **Mihhail Berezovski.** Numerical Simulation of Wave Propagation in Heterogeneous and Microstructured Materials. 2010.
94. **Tamara Aid-Pavlidis.** Structure and Regulation of BDNF Gene. 2010.
95. **Olga Bragina.** The Role of Sonic Hedgehog Pathway in Neuro- and Tumorigenesis. 2010.
96. **Merle Randrüüt.** Wave Propagation in Microstructured Solids: Solitary and Periodic Waves. 2010.
97. **Marju Laars.** Asymmetric Organocatalytic Michael and Aldol Reactions Mediated by Cyclic Amines. 2010.
98. **Maarja Grossberg.** Optical Properties of Multinary Semiconductor Compounds for Photovoltaic Applications. 2010.
99. **Alla Maloverjan.** Vertebrate Homologues of Drosophila Fused Kinase and Their Role in Sonic Hedgehog Signalling Pathway. 2010.
100. **Priit Pruunsild.** Neuronal Activity-Dependent Transcription Factors and Regulation of Human *BDNF* Gene. 2010.
101. **Tatjana Knjazeva.** New Approaches in Capillary Electrophoresis for Separation and Study of Proteins. 2011.
102. **Atanas Katerski.** Chemical Composition of Sprayed Copper Indium Disulfide Films for Nanostructured Solar Cells. 2011.
103. **Kristi Timmo.** Formation of Properties of CuInSe_2 and $\text{Cu}_2\text{ZnSn}(\text{S},\text{Se})_4$ Monograin Powders Synthesized in Molten KI. 2011.
104. **Kert Tamm.** Wave Propagation and Interaction in Mindlin-Type Microstructured Solids: Numerical Simulation. 2011.
105. **Adrian Popp.** Ordovician Proetid Trilobites in Baltoscandia and Germany. 2011.
106. **Ove Pärn.** Sea Ice Deformation Events in the Gulf of Finland and This Impact on Shipping. 2011.
107. **Germo Väli.** Numerical Experiments on Matter Transport in the Baltic Sea. 2011.
108. **Andrus Seiman.** Point-of-Care Analyser Based on Capillary Electrophoresis. 2011.
109. **Olga Katargina.** Tick-Borne Pathogens Circulating in Estonia (Tick-Borne Encephalitis Virus, *Anaplasma phagocytophilum*, *Babesia* Species): Their Prevalence and Genetic Characterization. 2011.
110. **Ingrid Sumeri.** The Study of Probiotic Bacteria in Human Gastrointestinal Tract Simulator. 2011.
111. **Kairit Zovo.** Functional Characterization of Cellular Copper Proteome. 2011.

112. **Natalja Makarytsheva.** Analysis of Organic Species in Sediments and Soil by High Performance Separation Methods. 2011.
113. **Monika Mortimer.** Evaluation of the Biological Effects of Engineered Nanoparticles on Unicellular Pro- and Eukaryotic Organisms. 2011.
114. **Kersti Tepp.** Molecular System Bioenergetics of Cardiac Cells: Quantitative Analysis of Structure-Function Relationship. 2011.
115. **Anna-Liisa Peikolainen.** Organic Aerogels Based on 5-Methylresorcinol. 2011.
116. **Leeli Amon.** Palaeoecological Reconstruction of Late-Glacial Vegetation Dynamics in Eastern Baltic Area: A View Based on Plant Macrofossil Analysis. 2011.
117. **Tanel Peets.** Dispersion Analysis of Wave Motion in Microstructured Solids. 2011.
118. **Liina Kaupmees.** Selenization of Molybdenum as Contact Material in Solar Cells. 2011.
119. **Allan Olsper.** Properties of VPg and Coat Protein of Sobemoviruses. 2011.
120. **Kadri Koppel.** Food Category Appraisal Using Sensory Methods. 2011.
121. **Jelena Gorbatšova.** Development of Methods for CE Analysis of Plant Phenolics and Vitamins. 2011.
122. **Karin Viipsi.** Impact of EDTA and Humic Substances on the Removal of Cd and Zn from Aqueous Solutions by Apatite. 2012.
123. **David Schryer.** Metabolic Flux Analysis of Compartmentalized Systems Using Dynamic Isotopologue Modeling. 2012.
124. **Ardo Illaste.** Analysis of Molecular Movements in Cardiac Myocytes. 2012.
125. **Indrek Reile.** 3-Alkylcyclopentane-1,2-Diones in Asymmetric Oxidation and Alkylation Reactions. 2012.
126. **Tatjana Tamberg.** Some Classes of Finite 2-Groups and Their Endomorphism Semigroups. 2012.
127. **Taavi Liblik.** Variability of Thermohaline Structure in the Gulf of Finland in Summer. 2012.
128. **Priidik Lagemaa.** Operational Forecasting in Estonian Marine Waters. 2012.
129. **Andrei Errapart.** Photoelastic Tomography in Linear and Non-linear Approximation. 2012.
130. **Külliki Krabbi.** Biochemical Diagnosis of Classical Galactosemia and Mucopolysaccharidoses in Estonia. 2012.
131. **Kristel Kaseleht.** Identification of Aroma Compounds in Food using SPME-GC/MS and GC-Olfactometry. 2012.
132. **Kristel Kodar.** Immunoglobulin G Glycosylation Profiling in Patients with Gastric Cancer. 2012.
133. **Kai Rosin.** Solar Radiation and Wind as Agents of the Formation of the Radiation Regime in Water Bodies. 2012.

134. **Ann Tiiman.** Interactions of Alzheimer's Amyloid-Beta Peptides with Zn(II) and Cu(II) Ions. 2012.
135. **Olga Gavrilova.** Application and Elaboration of Accounting Approaches for Sustainable Development. 2012.
136. **Olesja Bondarenko.** Development of Bacterial Biosensors and Human Stem Cell-Based *In Vitro* Assays for the Toxicological Profiling of Synthetic Nanoparticles. 2012.
137. **Katri Muska.** Study of Composition and Thermal Treatments of Quaternary Compounds for Monograin Layer Solar Cells. 2012.
138. **Ranno Nahku.** Validation of Critical Factors for the Quantitative Characterization of Bacterial Physiology in Accelerostat Cultures. 2012.
139. **Petri-Jaan Lahtvee.** Quantitative Omics-level Analysis of Growth Rate Dependent Energy Metabolism in *Lactococcus lactis*. 2012.
140. **Kerti Orumets.** Molecular Mechanisms Controlling Intracellular Glutathione Levels in Baker's Yeast *Saccharomyces cerevisiae* and its Random Mutagenized Glutathione Over-Accumulating Isolate. 2012.
141. **Loreida Timberg.** Spice-Cured Sprats Ripening, Sensory Parameters Development, and Quality Indicators. 2012.
142. **Anna Mihhalevski.** Rye Sourdough Fermentation and Bread Stability. 2012.
143. **Liisa Arike.** Quantitative Proteomics of *Escherichia coli*: From Relative to Absolute Scale. 2012.
144. **Kairi Otto.** Deposition of In₂S₃ Thin Films by Chemical Spray Pyrolysis. 2012.
145. **Mari Sepp.** Functions of the Basic Helix-Loop-Helix Transcription Factor TCF4 in Health and Disease. 2012.
146. **Anna Suhhova.** Detection of the Effect of Weak Stressors on Human Resting Electroencephalographic Signal. 2012.
147. **Aram Kazarjan.** Development and Production of Extruded Food and Feed Products Containing Probiotic Microorganisms. 2012.
148. **Rivo Uiboupin.** Application of Remote Sensing Methods for the Investigation of Spatio-Temporal Variability of Sea Surface Temperature and Chlorophyll Fields in the Gulf of Finland. 2013.
149. **Tiina Kriščiunaite.** A Study of Milk Coagulability. 2013.
150. **Tuuli Levandi.** Comparative Study of Cereal Varieties by Analytical Separation Methods and Chemometrics. 2013.
151. **Natalja Kabanova.** Development of a Microcalorimetric Method for the Study of Fermentation Processes. 2013.
152. **Himani Khanduri.** Magnetic Properties of Functional Oxides. 2013.
153. **Julia Smirnova.** Investigation of Properties and Reaction Mechanisms of Redox-Active Proteins by ESI MS. 2013.
154. **Mervi Sepp.** Estimation of Diffusion Restrictions in Cardiomyocytes Using Kinetic Measurements. 2013.

155. **Kersti Jääger.** Differentiation and Heterogeneity of Mesenchymal Stem Cells. 2013.
156. **Victor Alari.** Multi-Scale Wind Wave Modeling in the Baltic Sea. 2013.
157. **Taavi Päll.** Studies of CD44 Hyaluronan Binding Domain as Novel Angiogenesis Inhibitor. 2013.
158. **Allan Niidu.** Synthesis of Cyclopentane and Tetrahydrofuran Derivatives. 2013.
159. **Julia Geller.** Detection and Genetic Characterization of *Borrelia* Species Circulating in Tick Population in Estonia. 2013.
160. **Irina Stulova.** The Effects of Milk Composition and Treatment on the Growth of Lactic Acid Bacteria. 2013.
161. **Jana Holmar.** Optical Method for Uric Acid Removal Assessment During Dialysis. 2013.
162. **Kerti Ausmees.** Synthesis of Heterobicyclo[3.2.0]heptane Derivatives via Multicomponent Cascade Reaction. 2013.
163. **Minna Varikmaa.** Structural and Functional Studies of Mitochondrial Respiration Regulation in Muscle Cells. 2013.
164. **Indrek Koppel.** Transcriptional Mechanisms of BDNF Gene Regulation. 2014.
165. **Kristjan Pilt.** Optical Pulse Wave Signal Analysis for Determination of Early Arterial Ageing in Diabetic Patients. 2014.
166. **Andres Anier.** Estimation of the Complexity of the Electroencephalogram for Brain Monitoring in Intensive Care. 2014.
167. **Toivo Kallaste.** Pyroclastic Sanidine in the Lower Palaeozoic Bentonites – A Tool for Regional Geological Correlations. 2014.
168. **Erki Kärber.** Properties of ZnO-nanorod/In₂S₃/CuInS₂ Solar Cell and the Constituent Layers Deposited by Chemical Spray Method. 2014.
169. **Julia Lehner.** Formation of Cu₂ZnSnS₄ and Cu₂ZnSnSe₄ by Chalcogenisation of Electrochemically Deposited Precursor Layers. 2014.
170. **Peep Pitk.** Protein- and Lipid-rich Solid Slaughterhouse Waste Anaerobic Co-digestion: Resource Analysis and Process Optimization. 2014.
171. **Kaspar Valgepea.** Absolute Quantitative Multi-omics Characterization of Specific Growth Rate-dependent Metabolism of *Escherichia coli*. 2014.